# Plasma Physics and Chemistry for Nanomaterial and Device Fabrication

**A THESIS**
**SUBMITTED TO THE FACULTY OF THE GRADUATE SCHOOL**
**OF THE UNIVERSITY OF MINNESOTA**
**BY**

**Yunxiang Qin**

**IN PARTIAL FULFILLMENT OF THE REQUIREMENTS**
**FOR THE DEGREE OF**
**Doctor of Philosophy**

**Prof. Uwe R. Kortshagen, Adviser**

**May, 2018**

# Acknowledgements

I have never really been a very talkative person but I would like to take this opportunity to thank everyone. First and foremost, Prof. Kortshagen, thank you for allowing me the freedom to pursue various projects, for your kind patience when my research was stalled, and for your valuable guidance right when it really counts. I could not have asked for a better advisor.

Thank you to everyone in the Kortshagen group but especially to Toshi, Chad and Ben Pearce whose friendship I greatly enjoyed. Special thanks to Jihua for answering all my questions during the early years of my graduate study. Thank you to all the members of the High Temperature and Plasma Lab.

Thank you to my committee members for your effort and time, Prof. Aydil, Prof. Bruggeman, Prof. Girshick and Prof. Yang. I would also like to thank Prof. Aydil for your huge help on my first paper, Prof. Bruggeman, Prof. Ernie and Prof. Girshick for your plasma classes and molecular gas dynamics class that laid the solid foundation for my understanding of plasma physics.

Thank you to (almost all) the specialists at the characterization facility for your help on my research but especially to Nick (SEM) and Javier (XRD) for the delightful conversations during my routine characterizations. Special thanks to Bing (XPS) for the helpful discussions on XPS data fitting.

Thank you to the CSE machine shop for machining and building countless components for my plasma reactors, especially Mike and Bob.

# Abstract

This dissertation thesis revolves around one specific type of plasma: low pressure glow discharges.

In the first half we will focus on particle dynamics visualized by laser light scattering in a silane-containing dusty plasma. A better understanding of particle dynamics in dusty plasmas can be beneficial to both the intended synthesis of nanoparticles and the mitigation of nanoparticle contamination issues. Three distinct types of spatiotemporal behavior are observed for the dust particles, depending on the specific plasma power and pressure. The changing balance between the ion drag force and the electrostatic forces is hypothesized to be the dominant mechanism that determines particle dynamics in our case. It is also hypothesized that the dependence of particle dynamics on plasma power and pressure might be attributed to the generation and growth rate of dust particles. Based on our experimental results, the combination of laser light scattering and plasma emission proves to be an effective method for observing dust particles between tens of nanometers to a few hundreds of nanometers.

In the second half we will instead focus on the application of a magnetically enhanced glow discharge, namely magnetron sputtering, as a critical deposition technique for the fabrication of anisotropic plasmonic nanostructures. Upon light irradiation at the resonance frequency, plasmonic nanostructures can exhibit interesting near-field enhancement and far-field extinction, arising from the resonant oscillation of conduction electrons in the nanostructures. Specifically, we fabricated plasmonic nanocups and nanorods from alternative low-cost materials such as copper, aluminum and titanium nitride, rather than from expensive noble metals such as gold and silver. The copper and aluminum nanocups exhibit main plasmon resonances in the near-infrared region, potentially suitable for biological and window coating applications. The copper nanorods exhibit two plasmon resonance peaks as expected, corresponding to electron oscillations in the transverse and longitudinal directions, respectively. Two sputtering systems at the University of Minnesota Nano Fabrication Center (NFC) are used in this study. Due to certain limitations of the NFC systems we encountered during preliminary attempts at titanium nitride fabrication, we also constructed a custom-built angle sputtering system with a tiltable heated stage, introduced in detail in the appendix.

# Contents

# List of Tables

# List of Figures

# Chapter 1

# Introduction

## 1.1 Basic Plasma Concepts

Plasma can be defined as a quasi-neutral gas of charged particles that exhibit collective behavior. This means that the total amount of positive charge is equal to that of negative charge, and that every charged particle interacts with many other charged particles simultaneously, rather than in a binary fashion, through long-range Coulomb forces. The dynamics of the plasma particles is then determined by basic energy and momentum conservation laws along with Maxwell's equations, in which the electromagnetic fields both affect and are affected by the charged particles.

In our terrestrial environment, plasma only exists in very limited forms such as lightning and aurora. On a bigger picture, however, 99% of the substances constituting the universe are in the plasma form, some examples of which include the solar wind, planetary rings, nebulae and comets. While all the above plasmas occur naturally either on earth or in space, some plasmas are created by humans. Fluorescent lamps are arguably the most common example. Inside a fluorescent light bulb, ultraviolet photons are generated from electron-ion recombination or de-excitation processes in a mercury vapor plasma sustained with high voltages. These photons possess enough energy to excite the phosphor coating on the inside of the lamp, which in turn emits bright visible light and completes the conversion from electrical power to visible light.

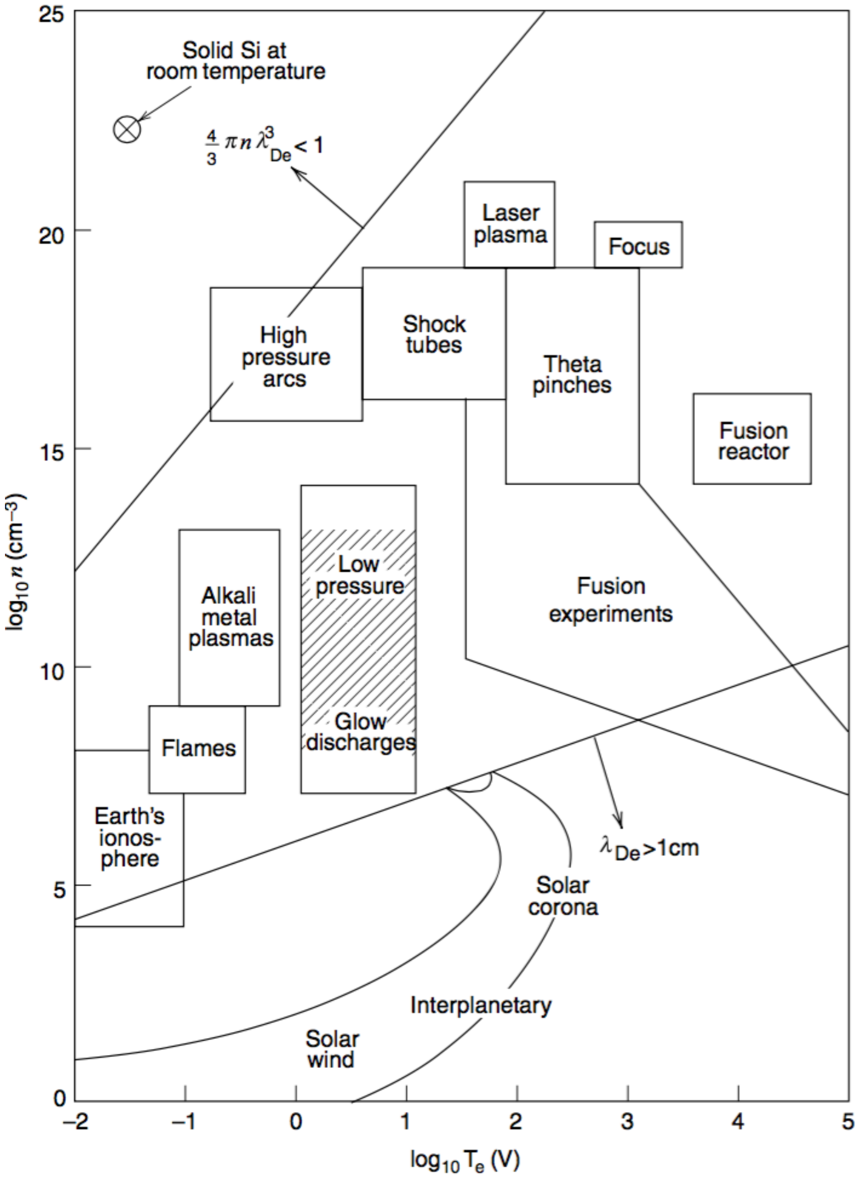

Figure 1.1: Classification of plasmas based on plasma density and electron temperature on a log-log scale [1].

Fig. 1.1 shows the wide ranges of plasma densities and electron temperatures a plasma can be operated at. In this thesis we are concerned with one specific type of plasma: low pressure glow discharges. They are often characterized by moderate plasma densities between $10^8$ to $10^{13}$ $cm^{-3}$ and electron temperatures between 1 and 10 eV. Ionization degrees of low pressure glow discharges are typically very low, on the order of $10^{-6}$ to $10^{-4}$. In other words, only 1 out of $10^4$ to $10^6$ neutral gas atoms or molecules is actually ionized in the plasma. Another important characterization parameter for glow discharges is the Debye length $\lambda_D$, the distance over which charge separation can spontaneously occur. In fact, the aforementioned plasma quasi-neutrality only holds true on a spatial scale larger than the Debye length. It follows that the dimensions of any plasma must be larger than its Debye length so as to remain quasi-neutral.

To determine the Debye length, consider a test particle with charge $q_T < 0$ and infinite mass, immersed in a uniform plasma and located at the origin of our coordinate system. Assuming that the heavy ions are immobile ($n_i(\mathbf{r}) = n_o$, where $n_o$ is the unperturbed plasma density), this test particle will locally perturb the plasma by repelling electrons, forming a positively charged region around it called "sheath", which tends to shield the long-range Coulomb field of the test particle. From Poisson's equation we have

$$\nabla^2\phi(\mathbf{r}) = -\frac{e}{\epsilon}(n_i - n_e) - \frac{q_T}{\epsilon}\delta(\mathbf{r})\,, \tag{1.1}$$

where $e$ is the elementary charge and $\delta(\mathbf{r})$ is the Dirac delta function. Now we further assume that electrons are in thermal equilibrium with themselves at temperature $T_e$ and that the density profile follows equilibrium statistical mechanics, *i.e.* $n_e = n_o \exp\left(e\phi/k_B T_e\right)$, Eqn. 1.1 can be written as

$$\nabla^2\phi(\mathbf{r}) = \frac{en_o}{\epsilon}\left[\exp\left(\frac{e\phi}{k_B T_e}\right) - 1\right] - \frac{q_T}{\epsilon}\delta(\mathbf{r}). \tag{1.2}$$

In the limit of $|e\phi| \ll k_B T_e$, the exponential term can be expressed by a Taylor's series expansion $\exp\left(e\phi/k_B T_e\right) \approx 1 + e\phi/k_B T_e$. Using this approximation, Eqn. 1.2 can then be written at $\mathbf{r} \neq 0$ as

$$\nabla^2 \phi(\mathbf{r}) - \frac{1}{\lambda_D^2} \phi(\mathbf{r}) = 0 \,, \tag{1.3}$$

where the Debye length has the form $\lambda_D = \sqrt{\frac{\epsilon k_B T_e}{n_o e^2}}$. It should be noted that, for the shielding idea to work properly, the number of charges inside the Debye sphere needs to be high enough since it is these charges that shield the test particle. This criterion can be expressed as $n_o \lambda_D^3 \gg 1$.

Now consider a slab of plasma with a thickness L in which the ions are immobile (due to their large masses) and the electrons are manually displaced by a small distance $\delta$ with respect to the ions, shown in Fig. 1.2.

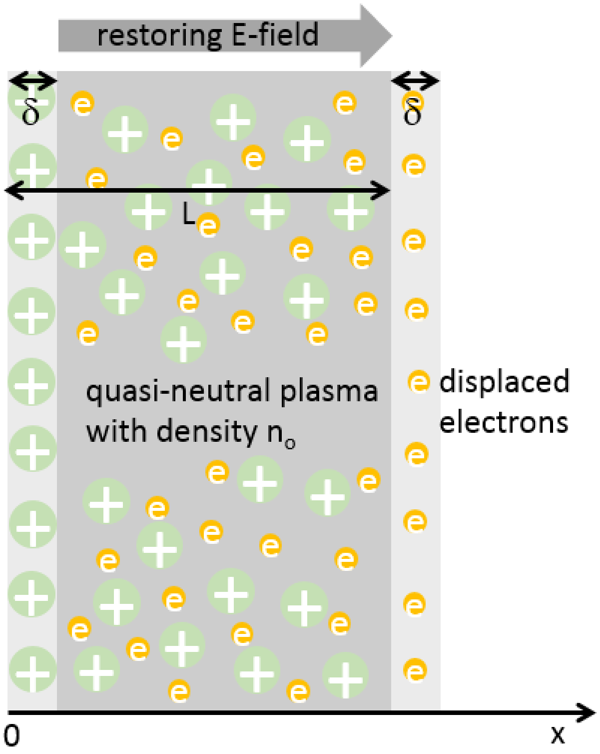

Figure 1.2: Schematic of displaced electrons and ions for the derivation of electron plasma frequency.

The induced electric field **E** between the separated electrons and ions can be described by the Poisson's equation

$$\boldsymbol{\nabla}\cdot\mathbf{E}=\frac{dE}{dx}=\frac{1}{\epsilon}\rho\,, \tag{1.4}$$

which after integration yields $E=\frac{n_o e\delta}{\epsilon}$, resulting in a force on the electron slab per unit volume

$$F=-en_oE=-\frac{n_o^2e^2\delta}{\epsilon}. \tag{1.5}$$

Denoting $\rho_m$ as the electron mass per unit volume (electron mass density) and from Newton's law we know that (for unit volume)

$$F=\rho_m a=\rho_m\frac{d^2\delta}{dt^2}. \tag{1.6}$$

Combining the above two equations and we have

$$\frac{d^2\delta}{dt^2}+\frac{n_oe^2}{\epsilon m_e}\delta=0\,, \tag{1.7}$$

which we recognize as the governing equation for a harmonic oscillator with a natural frequency of $\omega_{pe}=\sqrt{\frac{n_oe^2}{\epsilon m_e}}$, in this case called the electron plasma frequency. Note that we derived the electron plasma frequency under collisionless conditions while in a real plasma electrons collide with other particles, especially neutral gas atoms or molecules. In order for a plasma to exhibit collective behavior, *i.e.* collective electron oscillation near the electron plasma frequency $\omega_{pe}$, the electron-neutral collision frequency $\nu_{en}$ must be smaller than $\omega_{pe}/2\pi$. It also follows that, in addition to the spatial scale $\lambda_D$, plasma quasi-neutrality only holds true on a time scale larger than $1/\omega_{pe}$.

## 1.2 Motivation

This dissertation thesis focuses on the properties and applications of low pressure glow discharges.

We will first focus on particle dynamics of silicon nanoparticles generated inside a silane-containing dusty plasma in the first half of the dissertation thesis. A detailed introduction to dusty plasma is given in Chapter 2, but, for now, suffice it to say that dusty plasmas are simply plasmas containing solid particles (dust particles). While initially the developments in dusty plasma theories are contributed largely by the astrophysics research community, a stronger and renewed interest in dusty plasmas is later stimulated by contamination issues in industrial plasma processing. More recently it was also realized that dusty plasmas can be powerful manufacturing tools for various semiconductor nanocrystals. A detailed understanding of dust behaviors in a plasma is beneficial to both the manufacturing of nanoparticles and the mitigation of contamination issues. Therefore, in this dissertation thesis, we conducted a fundamental study on dusty plasma physics in terms of particle dynamics. Specifically, we resorted to laser light scattering and plasma emission to track the spatiotemporal evolution of particles and study their interaction with the plasma. It was found that particle distributions can be significantly influenced by plasma power and pressure, and that the combination of laser light scattering and plasma emission can be an easy yet effective diagnostic tool for particle distributions.

In the second half we will instead focus on the application of a magnetically enhanced glow discharge, namely magnetron sputtering, as a critical deposition technique for the fabrication of anisotropic plasmonic nanostructures. We will show that, compared to other physical vapor deposition techniques, magnetron sputtering offers unique advantages and is the most suitable technique for our purposes. Anisotropic plasmonic nanostructures, specifically nanocups and nanorods, are successfully fabricated by template-assisted magnetron sputtering. We focus on low-cost alternative materials such as copper, aluminum and titanium nitride, for which solution phase synthesis techniques hardly exist, rather than expensive noble metals such as gold and silver. Two magnetron sputtering systems at the University of Minnesota Nano Fabrication Center (NFC) are used in this study. Limitations of the NFC systems prompted us to construct our own custom-built angle sputtering system, which will be introduced in the appendix at the end.

## 1.3 Structure of the Dissertation Thesis

- Chapter 2 gives a detailed introduction to dusty plasmas that covers particle nucleation and growth, particle charging and particle dynamics, necessary for the understanding of experimental results in the following chapter.
- Chapter 3 describes the experimental setup and discusses the experimental results for the low pressure dusty plasma study.
- Chapter 4 gives a detailed introduction to magnetron sputtering and compares it with other physical vapor deposition techniques, necessary for understanding why magnetron sputtering is the most suitable deposition technique for our purposes, namely the fabrication of anisotropic plasmonic nanostructures from alternative materials including copper, aluminum and titanium nitride. A short introduction to plasmonics is also included, necessary for the understanding of experimental results in the following chapter.
- Chapter 5 describes the fabrication processes and experimental results for copper and aluminum nanocups.

- Chapter 6 describes the fabrication processes and experimental results for copper nanorods.
- Chapter 7 gives a conclusion to the dissertation thesis.
- Appendix A describes the preliminary results for titanium nitride fabrication and gives a detailed introduction to the custom-built angle sputtering system.

# Chapter 2

# Particle Dynamics in Dusty Plasmas: Background

Part of this chapter has been published in *Journal of Physics D: Applied Physics* in Ref. 2. In this chapter, we will present a general introduction to dusty plasmas. Using silane-containing plasmas as an example, we will discuss various basic dusty plasma concepts and theories necessary for the interpretation of experimental results reported in Chapter 3.

## 2.1 General Introduction to Dusty Plasmas

Dusty plasmas are plasmas containing solid particles with sizes ranging from a few nanometers to many microns [3]. These particles may either be produced internally through plasma chemistry or electrode sputtering, or be introduced externally. Most dusty plasmas are extraterrestrial as 99% of our universe is made of plasma, among which a large portion exists in the presence of dust particles or ice crystals [4, 5]. In this thesis, however, we will focus on a technologically important type of laboratory dusty plasma, namely low pressure nonthermal capacitively coupled plasmas (CCPs). Plasma enhanced chemical vapor deposition (PECVD) processes utilizing silane CCP plasmas are widely employed in the semiconductor industry for the fabrication of nanoscale electronic and optoelectronic devices. For these applications the formation of silicon particles (rather than the intended silicon thin films on the wafers) is usually considered as the main source of contamination and can decrease production yields significantly. Another example of *in situ* particle contamination in CCP plasmas can be found in reactive ion etching (RIE) processes, during which photoresists or other sacrificial layers are effectively removed from the underlying films via chemical reactions promoted by ion bombardment. Some of the etching products, however, may form particles, get suspended in the plasma and deposit back onto the wafer after plasma power is turned off.

On the other hand, over the past decade, it was also realized that low pressure nonthermal plasmas have the capability to synthesize nanoparticles with unique size-dependent electronic and optical properties unseen in their bulk counterparts. Indeed, low pressure discharges excited by fields oscillating at radio frequencies (rf) have been used to produce particles and films comprising particles that find applications as biological markers, transparent conductors, light emitting diodes and solar cells [6–11]. For the above reasons, significant efforts have been undertaken to study the formation and spatial distribution of particles generated in dusty plasmas.

In a dusty plasma, particles acquire charge by collecting electrons and ions. In low pressure nonthermal plasmas, dust particles are usually negatively charged because electrons have a much higher temperature than ions and thus move faster; the particles must charge negatively to repel the fast moving electrons so that a time averaged current balance between ions and electrons can be maintained. Charged particles are subject to various forces in the plasma such as the ion drag force and the electrostatic force, the magnitudes of which depend on particle size and particle charge, which depends on particle size itself. Consequently, particles show interesting dynamic behaviors in plasmas. For example, they can behave collectively to form distinct structures such as voids [12, 13], Coulomb crystals [14, 15], spheroids [16, 17] and swirling patterns [18, 19]. Due to their complicated behaviors, a better understanding of particle charging and particle dynamics in nonthermal plasmas is beneficial to both nanoparticle synthesis and the minimization of nanoparticle contamination in device fabrication.

It should be noted that the combination of dust particle and plasma can be described as either "particles in a plasma" or "a dusty plasma" [3], essentially depending on the ordering of the following characteristic length scales: dust particle radius $r_d$, average inter-particle distance $a$ and the plasma Debye length $\lambda_D$. For the case of $r_d \ll \lambda_D < a$, dust particles can be simply considered as a collection of isolated particles and the combination should be described as 'particles in a plasma' while for the case of $r_d \ll a < \lambda_D$ dust particles feel the presence of other particles (within the Debye sphere) and exhibit collective behavior, and the combination should be described as 'a dusty plasma'.

## 2.2 Silane-containing Dusty Plasmas: Particle Nucleation and Growth

Silane-containing plasmas in particular have been widely studied as a prototypical and technologically important example of the cases wherein the particles nucleate and grow *in situ* in the plasma. Watanabe and his coworkers [20–23] proposed that fast reactions between $SiH_2$ and $Si_nH_{2n}$ lead to the nucleation of silicon particles. They conducted laser light scattering (LLS) experiments to visualize the spatiotemporal evolution of silicon nanoparticles. Most silicon nanoparticles were shown by LLS to reside at the plasma/sheath boundary near the powered electrode. Based on the correlation between the spatially resolved LLS intensities and short lifetime neutral radical densities, they concluded that neutral radicals such as $SiH_2$ are the key elements initializing the plasma polymerization processes that eventually result in the nucleation of silicon particles.

On the other hand, Hollenstein, Boufendi, Bouchoule and their coworkers proposed in a series of papers [24–29] that negative ions are instead largely responsible for the nucleation of particles. They observed from mass spectrometry that power modulation at the kHz range allows the negative ions to leave the plasma during the plasma afterglow in the off half-cycle. Negative ions with up to 16 silicon atoms are detected (with 16 silicon atoms being the upper limit of their mass spectrometer) while only very small neutral and positive clusters with a few silicon atoms are detected. When negative ions are de-trapped during the off half-cycle, particle formations are significantly suppressed, indicating the important role negative ions play in particle nucleation. The same authors also proposed a three stage process for the nucleation and growth of silicon particles in a silane plasma, described in detail below.

Within 0.5 ms after the initiation of the plasma, small silicon nanoparticles with diameters of about 2 nm and concentrations exceeding $10^{10}\,cm^{-3}$ are formed by anion-neutral clustering. Starting with $SiH_3^-$, created by electron dissociative attachment onto $SiH_4$ molecules, anion-neutral clustering proceeds through reactions between $Si_nH_{2n+1}^-$ and vibrationally excited $SiH_4$ molecules. These small particles are highly monodisperse as shown in TEM measurements by them and many other authors. To explain this monodispersity, Fridman and his coworkers [30] came up with the concept of selective trapping.

When the average particle size reaches about 2 nm, anion clustering reaction slows down due to, first of all, the relaxation of vibrationally excited silane molecules on the cluster surface [31–33], and, second of all, the thermoneutral or even endothermic nature of some clustering reactions; vibrational energy from the silane molecules can therefore speed up the clustering reactions. Ion-ion recombinations (negative silane cluster and positive inert gas ions) then become more probable for these 2 nm negative clusters. For these neutralized 2 nm clusters, the charging time (non-dissociative electron attachment) is usually smaller than the residence time, indicating that they will be charged negatively at least once before they reach the edge of the plasma. Once these particles are charged, they are brought back into the center region of the plasma by the sheath field and ambipolar diffusion field. On the other hand, for neutral particles smaller than 2 nm, the charging time is significantly larger than the residence time and therefore they have a much lower chance to be charged negatively before they are lost to the wall. In addition, Fridman *et al.* [30] attributed the often observed delay in particle nucleation at high gas temperatures to vibrational-rotranslational relaxations described by a Landau-Teller expression. A later simulation study done by Bhandarkar, Kortshagen and Girshick in 2003 [34], however, found the temperature dependence of the Brownian diffusion coefficient to be the dominant factor in particle nucleation delay at high gas temperatures.

It is worth mentioning at this point that silicon particles synthesized in nonthermal silane plasmas at room temperature are in many cases crystalline. Mangolini *et al.* [6] and later Kramer *et al.* [35] concluded from Monte Carlo simulations that nanoparticles immersed in nonthermal plasmas can be heated up to several hundreds of Kelvin above the gas temperature, exceeding the crystallization temperatures of small nanoparticles, via energetic surfaces reactions such as electron ion recombination and $H_2$ abstraction. Further epitaxial growth on the nanocrystalline core yield larger crystalline particles.

As the 2 nm initial particles are trapped in the plasma by the selective trapping effect, more and more of these initial particles are formed and at a certain point they reach a concentration of $10^{10}$ to $10^{12}\,cm^{-3}$. Electron densities in low pressure CCPs are generally around $10^{9}\,cm^{-3}$ and thus are not able to charge all the initial particles negatively. As a consequence, a non-negligible fraction of the 1 - 2 nm particles are neutral and some even have positive charges [36]. Coagulation between these particles are enhanced by the opposite charges or image charges compared to the neutral coagulation rate, leading to a fast increase in particle size and decrease in particle concentration. During this period, surface deposition of silane radicals also occurs but they contribute very little to the mass of the particles and are generally neglected. However, surface deposition of silane radicals is much more likely to happen at this stage compared to ion clustering reactions from scratch, therefore effectively quenching the formation of new particles. When the average particle diameter reaches 50 or 60 nm, the particles are almost certainly negatively charged. The electrostatic repulsion between these particles then prevents them from further coagulation. Further growth of the particles at about 2 nm/s is attributed to surface deposition of $SiH_x$ radicals.

Similarly, Kortshagen, Girshick and their coworkers [34,37,38] came up with a comprehensive chemical kinetics model that included more than a hundred neutral and charged silicon species, and reached the conclusion that two anion-neutral clustering pathways, starting with $SiH_3^-$ and $SiH_2^-$ respectively, are vital for particle nucleation. Bleecker *et al.* [39] also concluded that negative ion clustering leads to the nucleation and growth of silicon particles. Specifically, the authors concluded that 90% of the particle nucleation starts with $SiH_3^-$ while the other 10% starts with $SiH_2^-$.

Finally we note that the seemingly conflicting nucleation mechanisms from Watanabe *et al.* and Hollenstein *et al.* may be reconciled by considering the potentially different neutral species residence time in their reactors, proposed by Watanabe in a later paper [40]. Clustering of neutral species can play a significant role in particle nucleation provided that their residence time is comparable to the timescale of nucleation. Different reactor geometries, gas flow rates, plasma pressures and vacuum pumping speeds can all affect the residence time of neutral species.

## 2.3 Dust particle-plasma Interaction

Nucleation and growth of dust particles affect the plasma and in some cases have been associated with the appearance of instabilities. For example, Cavarroc *et al.* studied silane-containing plasmas maintained between two parallel electrodes extensively and observed the appearance of a void region in the center of the plasma [41, 42]. This void was associated with a region where the nanoparticles are too small to scatter laser light significantly. They asserted that the nanoparticles nucleate and grow in this region that appears devoid of nanoparticles, and showed data from *in situ* plasma diagnostics and *ex situ* particle characterization that are consistent with the hypothesis that particle nucleation and growth in the silane plasma is cyclic. The production begins with nucleation of nanoparticles in the void and larger particles are pushed out towards the edge as they grow. Cavarroc *et al.* also observed instabilities coinciding with particle aggregation in the gas phase [43, 44]. The void region has also been observed in other dust-containing plasmas and has been associated with appearance of the so called "heartbeat" instability wherein the void expands and contracts periodically [12, 45]. In what follows we will first discuss dust-plasma interaction in terms of dust particle charging, *i.e.* collection of plasma particles (electrons and ions) by dust particles, and then the various forces acted upon the dust particles by the plasma.

### 2.3.1 Dust Particle Charging Theory

As mentioned earlier, dust particles immersed in a nonthermal plasma acquire charges by collecting electrons and ions from the plasma. Electric power deposited into the bulk plasma is coupled very effectively to the electrons while the energy exchange between electrons and heavy species via elastic collisions is extremely low, on the order of $2m_e/M$ [1], where $m_e$ is the electron mass and $M$ is the mass of heavy species. As a result, electrons are at a much higher temperature compared to the rest of the nonthermal plasma. Energetic electrons reach dust particles faster and set up an electric field such that future electron currents and ion currents can be balanced.

The well-known orbital motion limited (OML) theory provides a convenient estimate of current collection on particle surface although in many cases modifications must be made to account for complexities such as ion collisions with gas molecules [46–51], drainage of electrons due to particle charging [52] and ion velocity distributions deviated from a Maxwellian distribution. Nonetheless we will re-derive the OML currents below as the starting point due to its simplicity and fair accuracy when applied to small and sometimes even slightly larger dust particles in the collisionless regime. We will then move on to discuss the major assumptions used in OML and their validity.

The derivation starts with the conservation of momentum and energy which require that

$$m_j v_o b = m_j v_f r_d \, , \tag{2.1}$$

and

$$\frac{1}{2} m_j v_o^2 = \frac{1}{2} m_j v_f^2 + \frac{q_j q_d}{4\pi\epsilon r_d} \, , \tag{2.2}$$

where $m_j$ and $q_j$ are the mass and charge of the incoming plasma particle $j$ (electron or ion), $v_o$ and $v_f$ are the initial and final velocity (assumed grazing) of the plasma particle $j$, $b$ is the impact parameter, and $r_d$ and $q_d$ are the radius and charge of the dust particle, respectively. From these two equations we can write the collision cross section $\sigma_j^d$ as

$$\sigma_j^d = \pi r_d^2 \left(1 - \frac{2q_j q_d}{m_j v_o^2}\right) . \tag{2.3}$$

Denoting the velocity distribution function for the plasma particle $j$ as $f_j(v)$, we have

$$I_j = q_j \int_{V_{min}}^{\infty} v \sigma_j^d f_j(v) dv \, , \tag{2.4}$$

where $I_j$ is the incoming plasma particle current and $V_{min}$ is the integral threshold for the incoming particle velocity. For $q_j q_d < 0$, *i.e.* incoming plasma particle $j$ attracted to the dust particle, $V_{min} = 0$ whereas for $q_j q_d > 0$, *i.e.* incoming plasma particle $j$ repulsed by the dust particle, a minimum velocity is required for the plasma particle to reach the surface of the dust particle. This minimum velocity is determined by the potential energy difference between infinity (potential assumed to be 0) and the dust particle surface (potential denoted as $\phi_d$)

$$V_{min} = \sqrt{\frac{2q_j \phi_d}{m_j}} . \tag{2.5}$$

If we further assume that the plasma particle $j$ is at thermal equilibrium and can be characterized by a temperature $T_j$, then the distribution function can be written as

$$f_j(v_j) = n_j \left(\frac{m_j}{2\pi k_B T_j}\right)^{\frac{3}{2}} \exp\left(-\frac{m_j v_j^2}{2k_B T_j}\right) \, , \tag{2.6}$$

where $n_j$ is the density of the plasma particle $j$ and $k_B$ is the Boltzmann constant. Substituting Eqns. 2.3 and 2.6 into Eqn. 2.4, and writing the integral in spherical coordinates we obtain

$$
\begin{aligned}
I_j &= q_j \iiint v\sigma_j^d f_j(v) v^2 sin\theta dv d\theta d\phi \\
&= q_j \left(\frac{m_j}{2\pi k_B T_j}\right)^{\frac{3}{2}} \pi r_d^2 n_j \iiint \exp\left(-\frac{m_j v^2}{2k_B T_j}\right) v^3 \left[1 - \frac{2q_j\phi_d}{m_j v^2}\right] dv d\theta d\phi \\
&= q_j \left(\frac{m_j}{2\pi k_B T_j}\right)^{\frac{3}{2}} \pi r_d^2 n_j (2\pi)(2) \Bigg[ \int_{V_{min}}^{\infty} \exp\left(-\frac{m_j v^2}{2k_B T_j}\right) v^3 dv \\
&\quad - \int_{V_{min}}^{\infty} \exp\left(-\frac{m_j v^2}{2k_B T_j}\right) \frac{2e\phi_d}{m} v dv \Bigg], \qquad (2.7)
\end{aligned}
$$

where $\theta$ is integrated from 0 to $\pi$ and $\phi$ is integrated from 0 to $2\pi$. The constant before the brackets can be reorganized as

$$
2q_j \pi r_d^2 n_j \left(\frac{m_j}{k_B T_j}\right)^2 \sqrt{\frac{k_B T_j}{2\pi m_j}}.
$$

For $q_j\phi_d < 0$ and $V_{min} = 0$, we use the following integral formula with appropriate $n$, $b$ and $a$

$$
\int_0^{\infty} x^n \exp^{-ax^b} dx = \frac{1}{b} a^{-\frac{n+1}{b}} \Gamma\left(\frac{n+1}{b}\right). \qquad (2.8)
$$

Then current $I_j$ can be written as

$$
\begin{aligned}
I_j &= 2q_j \pi r_d^2 n_j \left(\frac{m_j}{k_B T_j}\right)^2 \sqrt{\frac{k_B T_j}{2\pi m_j}} \left[\frac{1}{2}\left(\frac{m_j}{2k_B T_j}\right)^{-2} - \frac{q_j\phi_d}{m}\left(\frac{m_j}{2k_B T_j}\right)^{-1}\right] \\
&= 4q_j \pi r_d^2 n_j \sqrt{\frac{k_B T_j}{2\pi m_j}} \left[1 - \frac{q_j\phi_d}{k_B T_j}\right]. \qquad (2.9)
\end{aligned}
$$

For $q_j\phi_d > 0$ and $V_{min} = \left(\frac{2q_j\phi_d}{m_j}\right)^{\frac{1}{2}}$, we start with the first integral

$$
\begin{aligned}
\int_{V_{min}}^{\infty} \exp\left(-\frac{m_j v^2}{2k_B T_j}\right) v^3 dv &= \frac{1}{4}\int_{\frac{2q_j\phi_d}{m_j}}^{\infty} \exp\left(-\frac{m_j x}{2k_B T_j}\right) dx^2 \\
&= \frac{1}{2}\int_{\frac{2q_j\phi_d}{m_j}}^{\infty} \exp\left(-\frac{m_j x}{2k_B T_j}\right) x dx \\
&= \frac{1}{2}\left(-\frac{m_j}{2k_B T_j}\right)^{-1}\int_{\frac{2q_j\phi_d}{m_j}}^{\infty} \exp\left(-\frac{m_j x}{2k_B T_j}\right) x d\left(-\frac{m_j x}{2k_B T_j}\right) \\
&= \frac{1}{2}\left(-\frac{m_j}{2k_B T_j}\right)^{-1}\int_{\frac{2q_j\phi_d}{m_j}}^{\infty} x d\exp\left(-\frac{m_j x}{2k_B T_j}\right) \\
&= \frac{1}{2}\left(-\frac{m_j}{2k_B T_j}\right)^{-1}\Bigg[x\exp\left(-\frac{m_j x}{2k_B T_j}\right)\Bigg|_{\frac{2q_j\phi_d}{m_j}}^{\infty} \\
&\quad - \int_{\frac{2q_j\phi_d}{m_j}}^{\infty} \exp\left(-\frac{m_j x}{2k_B T_j}\right) dx \\
&= \frac{1}{2}\left(-\frac{2k_B T_j}{m_j}\right)\exp\left(-\frac{q_j\phi_d}{k_B T_j}\right)\Bigg[-\frac{2q_j\phi_d}{m_j}-\frac{2k_B T_j}{m_j}\Bigg],
\end{aligned}
$$

where $x = v^2$ is a dummy variable. For the second integral, we get

$$
\begin{aligned}
\int_{V_{min}}^{\infty} \exp\left(-\frac{m_j v^2}{2k_B T_j}\right)\frac{2q_j\phi_d}{m_j} v dv &= \frac{q_j\phi_d}{m_j}\int_{\frac{2q_j\phi_d}{m_j}}^{\infty} \exp\left(-\frac{m_j x}{2k_B T_j}\right) dx \\
&= \frac{q_j\phi_d}{m_j}\left(-\frac{m_j}{2k_B T_j}\right)^{-1}\exp\left(-\frac{m_j x}{2k_B T_j}\right)\Bigg|_{\frac{2q_j\phi_d}{m_j}}^{\infty} \\
&= \frac{q_j\phi_d}{m_j}\left(\frac{2k_B T_j}{m_j}\right)\exp\left(-\frac{q_j\phi_d}{k_B T_j}\right).
\end{aligned}
$$

Therefore the current $I_j$ can be writen as

$$
I_j = 4q_j\pi r_d^2 n_j\sqrt{\frac{k_B T_j}{2\pi m_j}}\exp\left(-\frac{q_j\phi_d}{k_B T_j}\right). \tag{2.10}
$$

In summary, the current $I_j$ to the particle is

$$I_j = \begin{cases} 4q_j\pi r_d^2 n_j\sqrt{\dfrac{k_BT_j}{2\pi m_j}}\left(1-\dfrac{q_j\phi_d}{k_BT_j}\right) & \text{if } q_jq_d < 0, \\ 4q_j\pi r_d^2 n_j\sqrt{\dfrac{k_BT_j}{2\pi m_j}}\exp\left(-\dfrac{q_j\phi_d}{k_BT_j}\right) & \text{if } q_jq_d > 0. \end{cases} \tag{2.11}$$

By equating the ion current and the electron current we obtain the average electric potential $\phi_d^f$ that the dust particle oscillates around, also known as the floating potential. It can be shown that, in the case of $r_d \ll \lambda_D$, the capacitance of the dust particle in the plasma is approximated as $C_d = 4\pi\epsilon_d r_d$ [53]. Then the particle charge $q_d$ can be written as $q_d = 4\pi\epsilon_d r_d \phi_d^f$.

Since OML does not solve the Poisson's equation, no potential profiles around the dust particle can be obtained. For $r_d \ll \lambda_D$ the potential profile near the dust particle is usually assumed to have the Debye-Huckel [54] or Yukawa form [55], also known as the screened Coulomb potential

$$\phi = \frac{q_d}{4\pi\epsilon r}\exp\left(-\frac{r-r_d}{\lambda_D}\right). \tag{2.12}$$

Note that the potential profile resembles that of a classical Coulomb potential near the dust particle surface, *i.e.* no shielding near the dust particle surface. Also note that this screened Coulomb potential does not consider the shielding effects of trapped ions, which will be discussed below.

During OML derivation two major assumptions are made, among others, and specifically they are: (1) plasma particles (electrons and ions) have collisionless orbits and (2) no significant potential barriers (due to centrifugal forces) are encountered by the plasma particles when approaching the dust particle in the case of $q_jq_d < 0$. The latter assumption is examined in detail in Ref. 56 where the author concluded that in the limit of small dust particles, *i.e.* $r_d \ll \lambda_D$, the assumption of no significant potential barrier is reasonable. The collisionless assumption, however, has raised many questions and concerns. Initially the collisionless assumption is thought to be justified by the oftentimes large ion mean free path $\lambda_{i,mfp}$ compared to $\lambda_D$ [57]. However, later it was proposed by several researchers that even in the case of $\lambda_{i,mfp} > \lambda_D$ trapped ions due to collisions still cannot be ignored as the density of these ions can be built up indefinitely until some collision processes knock these ions out of their orbits [58–60]. Goree pointed out that the steady state density of trapped ions is actually independent of the ion-neutral collision frequency as both trapping and de-trapping rates are proportional to the collision frequency, and that the total number of trapped ions can be significant based on his Monte Carlo simulation [46]. Later Zobnin *et al.* performed Monte Carlo simulation to obtain the spatial profile of trapped ion density, further proving that trapped ions can make important modifications to the OML theory [47]. Lampe *et al.* then developed an analytical model for the ion density profile that found good agreement with Zobnin's simulation results [48]. Generally speaking, OML can over-predict the dust particle charge by a factor of 2 or 3. In 2005, Khrapak *et al.* came up with the capture radius concept and proposed a much simpler analytical model based on this concept [50]. The authors proposed that there exists a capture radius at which the kinetic energy of the slow ions created by ion-neutral collisions, on the order of $k_B T_g$, is smaller than the magnitude of the screened Coulomb potential energy. These ions are essentially trapped in the potential field of the dust particle as they do not possess enough kinetic energy to overcome the negative potential energy, and will eventually be collected by the particle either directly or after subsequent collisions. Following this capture radius idea, Gatti and Kortshagen later developed another elegant analytical model for ion currents across the entire range from OML to hydrodynamic [51]. In their analytical model the total ion current can be written as a weighted sum of the OML current

$$I_i^{OML} = \pi r_d^2 v_{i,th} n_i \left(1 - \frac{e\phi_d}{k_B T_i}\right) , \tag{2.13}$$

the collision-enhanced current

$$I_i^{CE} = \pi \left(1.22 R_o\right)^2 n_i v_{i,th} , \tag{2.14}$$

and the hydrodynamic current

$$I_i^{HY} = 4\pi r_d n_i \mu_i |\phi_d|. \tag{2.15}$$

Combining all the ion current contributions above we get

$$I_i = P_0 I_i^{OML} + P_1 I_i^{CE} + P_{>1} I_i^{HY} , \tag{2.16}$$

where $P_0$, $P_1$ and $P_{>1}$ are the probabilities of having zero, one and more than one ion-neutral collision within the capture radius $R_o$ [61], $v_{i,th}$ is the ion thermal velocity and $n_i$ is the ion density. $I_i^{OML}$ and $I_i^{HY}$ were originally derived by Khrapak *et al.* in Ref. 50.

OML also neglects sheath effects and considers only the orbiting effects. This can be justified in the limit of very large $\lambda_D$ compared to $r_d$ by looking at the re-scaled Poisson's equation [62]

$$\nabla^2 \left(\frac{e\phi}{k_B T_e}\right) = \frac{1}{\lambda_D^2} \left(\frac{n_e}{n_o} - \frac{n_i}{n_o}\right) , \tag{2.17}$$

where $n_o$ is the undisturbed plasma density. We can see that when $\lambda_D$ approaches $\infty$, the equation can be approximated as

$$\nabla^2 \phi = 0. \tag{2.18}$$

This means that the potential function $\phi$ can be specified without considering the presence of the plasma explicitly. Taking this $\phi$ to have the form of screened Coulomb potential, which is an excellent approximation for small dust particles, we can solve the dynamics of the incoming plasma particles with simple particle mechanics. Note that the screened Coulomb potential approaches the classical Coulomb potential near the particle surface.

At the other end of the spectrum, *i.e.* $\lambda_D$ approaching zero and much smaller than the dust particle, plasma potential varies on a scale larger than $\lambda_D$ and then we have, in one-dimensional form

$$\frac{d^2\phi}{dx^2}\lambda_D^2 = 0 = \frac{n_e - n_i}{n_o}. \tag{2.19}$$

In other words, we have quasi-neutrality right up to the edge of the plasma. On the other hand, the sheath region is not quasi-neutral by definition. It can be shown that the smooth transition between bulk plasma and sheath requires the ions to achieve at least the Bohm velocity at the sheath edge [63]. This means that for large dust particles and thin sheaths a good estimation of ion current can be obtained by Bohm velocity.

In this thesis, we only deal with small silicon particles ($r_d < 100$ nm) generated in relatively low pressure CCP plasmas and the classical OML theory predicts dust particle charge and potential reasonably well in this regime.

### 2.3.2 Forces and Dust Particle Dynamics

Charged dust particles immersed in a nonthermal plasma are subject to various forces. In this section we give a brief review for each of the forces.

#### 2.3.2.1 Electrostatic Force

Daugherty *et al.* [64] showed in their papers that, for a dust particle immersed in a plasma, although the Debye sheath around it can shield the rest of the plasma from the electric field generated by the particle, it cannot shield an externally applied electric field from the dust particle. Hamaguchi *et al.* [65] pointed out that the Debye sheath is not attached to the dust particle in any form but rather is just a local perturbation of the plasma. If the particle moves from spot A to spot B, then the disturbed region around spot A will gradually recover once the particle is gone and a new perturbation will form around spot B. Following Daugherty *et al.* the electrostatic force $\mathbf{F}_e$ exerted on the dust particle by an electric field $\mathbf{E}$ can be written as

$$\mathbf{F}_e = q_d \mathbf{E} \left[ 1 + \frac{(r_d/\lambda_D)^2}{3(1 + r_d/\lambda_D)} \right] , \tag{2.20}$$

where $q_d$ is the charge carried by the dust particle and $r_d$ is the dust particle radius. The derivation of this expression assumed that the potential around the dust particle can be described by the screened Coulomb potential and that there are no trapped ions.

The first term in Eqn. 2.20 is the vacuum electrostatic force while the second term can be interpreted as the dipolar force due to polarization of the Debye sheath. In the limit of $r_d \ll \lambda_D$ the total electrostatic force can be simply approximated by the vacuum electrostatic force.

#### 2.3.2.2 Ion Drag Force

The ion drag force can be defined as the momentum transfer from ions to dust particles per unit time. There are a total of three possible ways for this momentum transfer to happen: (1) direct ion bombardment onto the dust particle, in other words collection of ions by the dust particle, (2) Coulomb collisions between ions and the dust particle, and finally (3) distortion of the Debye sheath by ion fluid flow. The last contribution has been shown to have a minor effect on the overall ion drag force and therefore will be neglected here [66]. Then the total ion drag force $F_{ion}$ can be expressed as

$$\mathbf{F}_{ion} = \mathbf{F}_{Coll} + \mathbf{F}_{Coul}. \tag{2.21}$$

Both ion drag contribution can be expressed in a general form

$$\mathbf{F} = \sigma n_i v_s m_i \mathbf{v_i}\,, \tag{2.22}$$

where $n_i$ and $m_i$ are the ion density and ion mass, $v_s$ is the mean ion speed given by $\sqrt{v_i^2 + v_{i,th}^2}$ with $v_i$ being the ion drift velocity and $v_{i,th}$ being the ion thermal velocity and $\sigma$ is the collision cross section. For $\mathbf{F}_{Coll}$ the cross section $\sigma_{Coll}$ was obtained during OML derivation

$$\sigma_{Coll} = \pi b_c^2 = \pi r_d^2 \left(1 - \frac{2e\phi_d}{m_i v_i^2}\right). \tag{2.23}$$

For $\mathbf{F}_{Coul}$ the cross section $\sigma_{Coul}$ can be obtained from [67]

$$\sigma_{Coul} = 4\pi b_0^2 \int_{b_c}^{\lambda_D} \frac{b db}{b_0^2 + b^2}\,, \tag{2.24}$$

where $b$ is the impact parameter, $b_0$ is the distance of closest approach and also the impact parameter corresponding to a 90 degree Coulomb deflection, given as $b_0 = r_d \frac{e\phi_d}{m_i v_i^2}$. Debye length $\lambda_D$ is chosen as the upper limit of the integral to prevent the integral from diverging. Here the Debye length can be approximated by the electron Debye length in most cases due to the fact that ions streaming at a high velocity $v_i$ cannot form a sheath effectively and will just fly by the dust particle. The upper limit of the collection cross section $b_c$ is used as the lower limit of the Coulomb scattering cross section. The integral of Eqn. 2.24 yields

$$\sigma_{Coul} = 4\pi b_0^2 \frac{1}{2} \ln\left(\frac{b_0^2 + \lambda_D^2}{b_0^2 + b_c^2}\right)\,, \tag{2.25}$$

where $\frac{1}{2}\ln\left(\frac{b_0^2+\lambda_D^2}{b_0^2+b_c^2}\right)$ is known as the Coulomb logarithm and is around 10 to 20 for most laboratory plasmas. Note that both ion drag contribution are proportional to $r_d^2$, embedded in $b_0^2$ or $b_c^2$.

#### 2.3.2.3 Neutral Drag Force

Similar to the ion drag force, neutral drag can be defined as the momentum transfer between neutral gas molecules and dust particles per unit time. A detailed discussion of this force can be found in the work by Graves *et al.* [68] and is given by

$$\mathbf{F}_n = \frac{4}{3}\pi r_d^2 n_n(\mathbf{v}_d - \mathbf{v}_n)v_{n,th}m_n\,, \tag{2.26}$$

where $n_n$, $v_{n,th}$, $m_n$, $\mathbf{v}_n$ are the gas density, thermal velocity, mass and average velocity of the neutral gas molecules and $\mathbf{v}_d$ is the average velocity of the dust particle.

#### 2.3.2.4 Gravitational Force

The gravitational force can be written as

$$\mathbf{F}_g = \frac{4}{3}\pi r_d^3\rho\mathbf{g}\,, \tag{2.27}$$

where $\rho$ is the mass density of the dust particle and $\mathbf{g}$ is the gravitational acceleration.

#### 2.3.2.5 Thermophoretic Force

Dust particles immersed in a neutral gas with a temperature gradient $\nabla T_n$ experience the thermophoretic force. A net momentum transfer from the neutral gas to the dust particle occurs due to the larger momentum transfer from the hot gas side. Talbot *et al.* [69] first derived the following form for the thermophoretic force:

$$\mathbf{F}_T = -\frac{8}{15}\sqrt{2\pi}\frac{r_d^2}{v_{n,th}}\left[1 + \frac{5\pi}{32}(1 - \alpha_{ac})\right] k_n^{cond}\nabla T_n \,, \tag{2.28}$$

where $v_{n,th}$ is the thermal velocity of the neutral gas, $\alpha_{ac}$ is the accommodation coefficient that approaches 1 when temperatures are less than $500K$, and $k_n^{cond}$ is the thermal conductivity of the neutral gas.

Due to the limited amount of gas heating and electrode heating in our dusty plasma, indicated by the merely warm electrodes after maintaining the plasma for a long time, e.g. a few hours, it is safe to assume that the thermophoretic force is negligible in our case.

# Chapter 3

# Particle Dynamics in Dusty Plasmas: Experimental Setup, Results and Discussion

Part of this chapter has been published in *Journal of Physics D: Applied Physics* in Ref. 2. Herein, we report the observation of dust particle dynamics from laser light scattering (LLS) measurements conducted in a 13.56 MHz capacitively coupled dusty plasma maintained in silane and argon. Although LLS intensity is a complex function of particle size, density, shape and refractive index, and its interpretation requires care, one can easily visualize where particles are generated and how they move in the plasma.

Specifically, we focus on the spatiotemporal evolution of dust particles in the plasma as a function of pressure and power. We observed three distinct types of temporal evolution behavior for the nanoparticle dust cloud in the plasma and classified these into three regimes based on pressure and power. Each regime features a distinct pattern in laser light scattering measurements. At low pressures (∼80–100 mTorr) and high powers (∼40–60 W) we observed periodically repeating expansions and contractions of a continuous dust cloud for the first time. Dust voids, which have been reported before, were observed at high pressures (~100–150 mTorr) and low powers (~20–40 W) in the center of the plasma. In the intermediate regime, the two dust cloud structures mentioned above both appear, connected by a transition stage during which the continuous cloud breaks apart and forms a dust void in the plasma center. A mechanism is proposed to explain the observed dynamics of the nanoparticles in all three regimes. The balance between the ion drag force and the electrostatic force and their dependence on particle size are hypothesized to be the dominant factors that determine the nanoparticle cloud dynamics. It is also hypothesized that the difference in the nucleation and growth rate of the particles might have contributed to the different dust cloud structures observed in each regime.

## 3.1 Experimental Setup

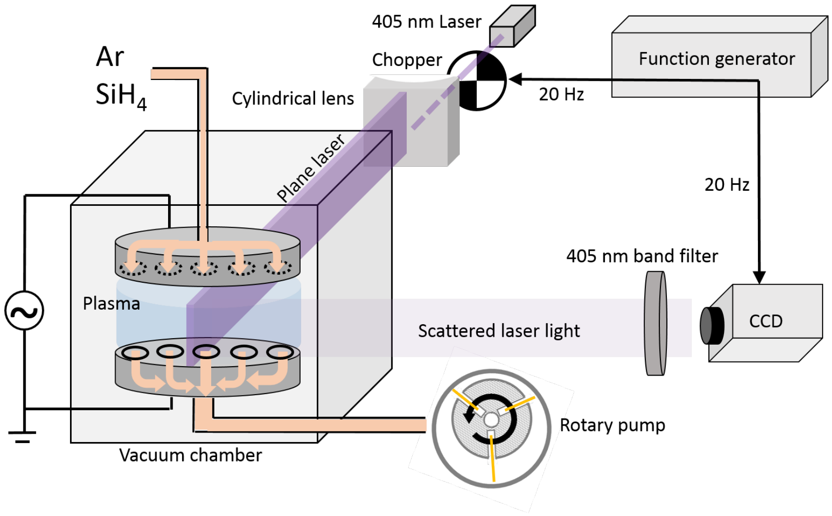

Figure 3.1: Schematic of the CCP plasma reactor and LLS diagnostics.

Experiments were conducted in a parallel plate capacitively coupled plasma reactor described previously in Ref. 70. Fig. 3.1 shows a schematic of the experimental setup. Plasma is maintained between two planar shower-head electrodes each 19.2 cm in diameter and separated by 2.7 cm. The upper electrode is connected to a 13.56 MHz rf power source through a matching network, which enables the reflected power (to the power supply) to be adjusted to 0 W in all experiments. Gases are fed through the two-dimensional array of holes on the powered upper electrode and pumped out of the reactor through the holes on the grounded bottom electrode. A 405 nm laser (model LBX-405-100-CIR-PP) and a cylindrical lens are used to produce a planar sheet of laser light. Scattered laser light is imaged onto a CCD camera perpendicular to the plane of this sheet of laser light. An interference filter with a center wavelength of 405 nm is placed in front of the CCD camera to allow only the scattered laser light through, while filtering all other wavelengths. However, the filter has a bandwidth of 10 nm and plasma emission in this wavelength range also contributes to the light intensity detected by the CCD camera. In fact, plasma emission is quite strong compared to scattered laser light at low particle densities and small particle sizes. To decouple scattered laser light from plasma emission, an optical chopper is synchronized with the camera such that, for every two consecutive frames, one frame is recorded with the laser blocked and only plasma emission is detected, and the other is recorded with the laser sheet illuminating the region between the electrodes such that both plasma emission and scattered laser light are recorded. The difference between the two frames is the scattered laser light intensity.

In the present study, plasma pressure is varied between 80 mTorr and 150 mTorr and power is varied between 20 W and 60 W (nominal power displayed on the power supply unit). The precursor and carrier gases are 5% silane in argon and 99.99% industrial grade argon, respectively. The flow rate ratio of argon to 5% silane diluted in argon is kept constant at 2.69 throughout the study. Plasma pressure is varied by adjusting the total gas flow rates. Specific flow rates for each pressure are summarized in Table 3.1.

Before conducting a laser light scattering experiment, during which nanoparticles generated in the plasma are visualized, electrodes are pre-heated by maintaining a pristine argon plasma for 15 minutes. After this pre-heating step, we

Table 3.1: Flow rates used in the present study.

| Pressure (mTorr) | Argon[a] flow rate (sccm) | 5% silane in argon[b] flow rate (sccm) |
|---|---|---|
| 80 | 10.7 | 4 |
| 90 | 11.9 | 4.4 |
| 100 | 14 | 5.2 |
| 130 | 19 | 7 |
| 150 | 21 | 7.8 |

[a,b] The argon to 5% silane in argon flow rate ratio is kept constant at 2.69.

turn off the argon plasma, adjust the flow rates of silane and argon, wait for the flow rates and gas composition in the vacuum chamber to stabilize (typically 6 minutes), and then strike the plasma and begin the scattering experiments. In a typical experiment, LLS is recorded for approximately 5 or 6 minutes. After each experiment, silane flow is stopped and the vacuum chamber is purged with argon flow for 6 minutes before we start the next experiment. After 2 hours of experiments with dusty plasmas, we clean both electrodes with isopropyl alcohol to minimize the influence of deposited particles from previous experiments.

## 3.2 Sample Frames

Figure 3.2: Sample frames recorded at t = 273 s for a $SiH_4/Ar$ plasma maintained at 100 mTorr and 40 W. Laser scattering dominates although plasma emission can still be extracted. (see Fig. 3.3)

Fig. 3.2 shows two consecutive frames recorded by the CCD camera without and with the chopper blocking the laser sheet in a typical experiment. The second frame is the spatial variation of plasma emission within the 10 nm bandwidth centered at 405 nm. The spatial variation of LLS is obtained by subtracting the second frame from the first frame. Both frames in Fig. 3.2 are grayscale images where 0 represents the weakest intensity (black) and 255 represents the strongest intensity (white). In the first frame a dust cloud can be seen clearly between the two electrodes, with a maximum intensity of 256 (camera is saturated in some areas). The second frame has a maximum intensity of 47 and the spatial variation of plasma emission intensity cannot be appreciated without normalization (see below).

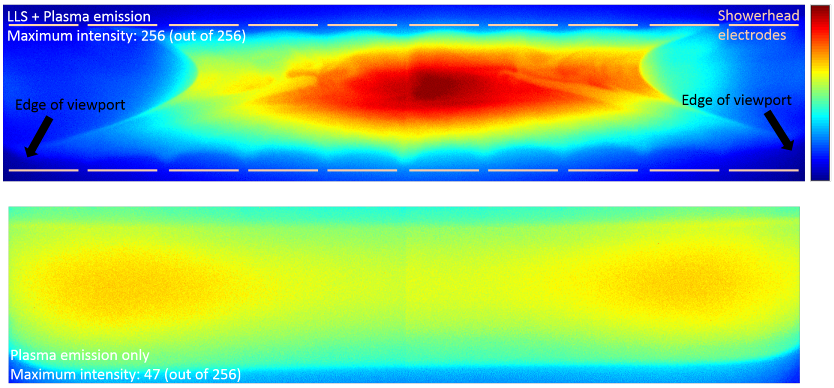

Figure 3.3: The same sample frames as in Fig. 3.2 but intensities are normalized by dividing the value at each pixel by the maximum intensity.

Fig. 3.3 shows the same data as in Fig. 3.2 but uses a normalized color scale where the intensity at each pixel has been divided by the maximum intensity in that frame. Sheaths near both electrodes should appear as dark regions (black or dark blue) in both Figs. 3.2 and 3.3 since negatively charged particles and electrons are expelled from the sheaths, rendering both LLS and plasma emission intensities nearly zero in the sheaths. However, it is not easy and trivial to identify the sheaths in the frames due to the dark environment (solid electrodes) adjacent to them. In addition, the plasma emission frames are not perfect since the entire plasma glows and gets recorded by the CCD camera, but only the plane in which the laser sheet lies is actually in focus.

The dust cloud near the electrodes in this flow configuration exhibits periodic spatial modulation caused by the holes on the shower-head electrodes. The hole positions on the shower-head electrodes are indicated by the dashed lines in Fig. 3.3. Near the upper electrode, the neutral drag force exerted by the gas flow pushes the particle cloud downwards right below the holes. Near the bottom electrode, the dust cloud extends towards the holes as the particles are carried out of the region between the electrodes by the neutral drag force.

Figs. 3.2 and 3.3 show the nanoparticle cloud at a particular point in time where the dust cloud has an hourglass shaped appearance with its waist getting narrower towards the center axis of the electrodes. The radial periphery appears devoid of particles. As will be shown in the following sections, the appearance of the cloud changes with time and its behavior depends on plasma power and pressure.

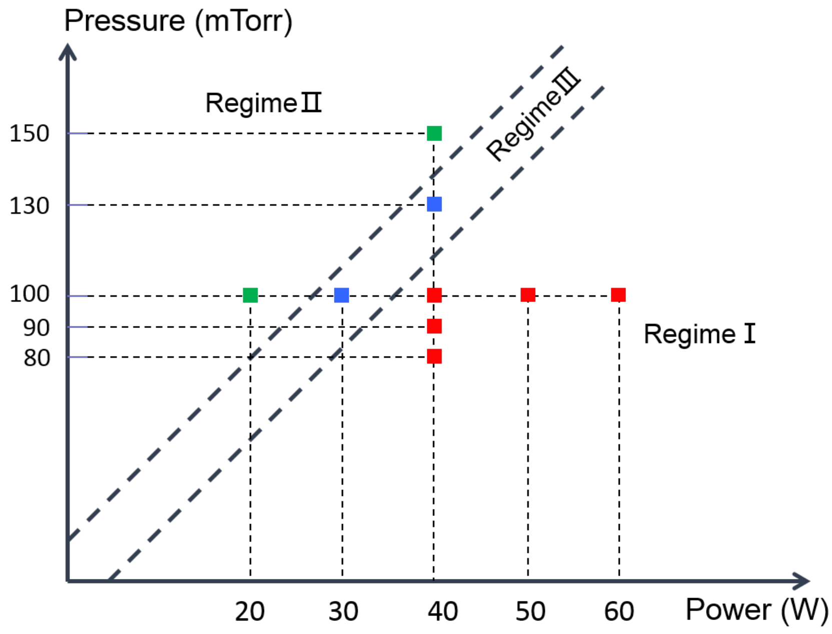

Figure 3.4: Plasma conditions and regimes studied in this work.

## 3.3 Results and Discussion

Three different types of dust cloud behavior, depending on plasma pressure and power, were observed in this study and were correspondingly classified into the three regimes shown in Fig. 3.4. Type 1 behavior is observed at low pressures and high powers while type 2 behavior is observed at high pressures and low powers. Intermediate pressure to power ratios display type 3 behavior. Each regime features a distinct LLS pattern as will be discussed in detail below. TEM images of particles collected at several different times have been reported before for the same reactor [70]. Fig. 3.5(a) and 3.5(b) show another two typical TEM images of particles collected at t = 30 s and t = 300 s for a $SiH_4$/Ar plasma maintained at 80 mTorr and 40 W (Regime 1). As reported in [70], average particle sizes for this plasma at t = 30, 90, 150, 180 and 300 s are about 20, 30, 140, 160 and 110 nm, respectively. The decrease in average particle size at t = 300 s is due to a new generation of small particles.

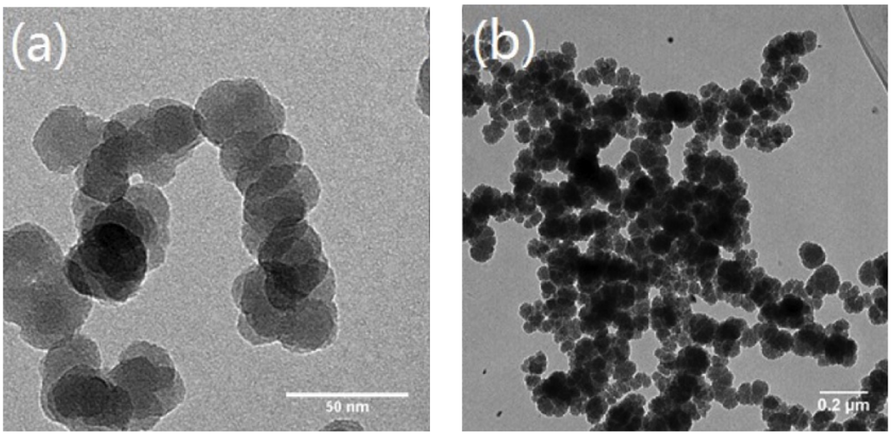

Figure 3.5: TEM images of particles collected at (a) t = 30 s and (b) t = 300 s. The $SiH_4$/Ar plasma was operated at 80 mTorr and 40 W. These particles were collected in the effluent after the plasma was turned off.

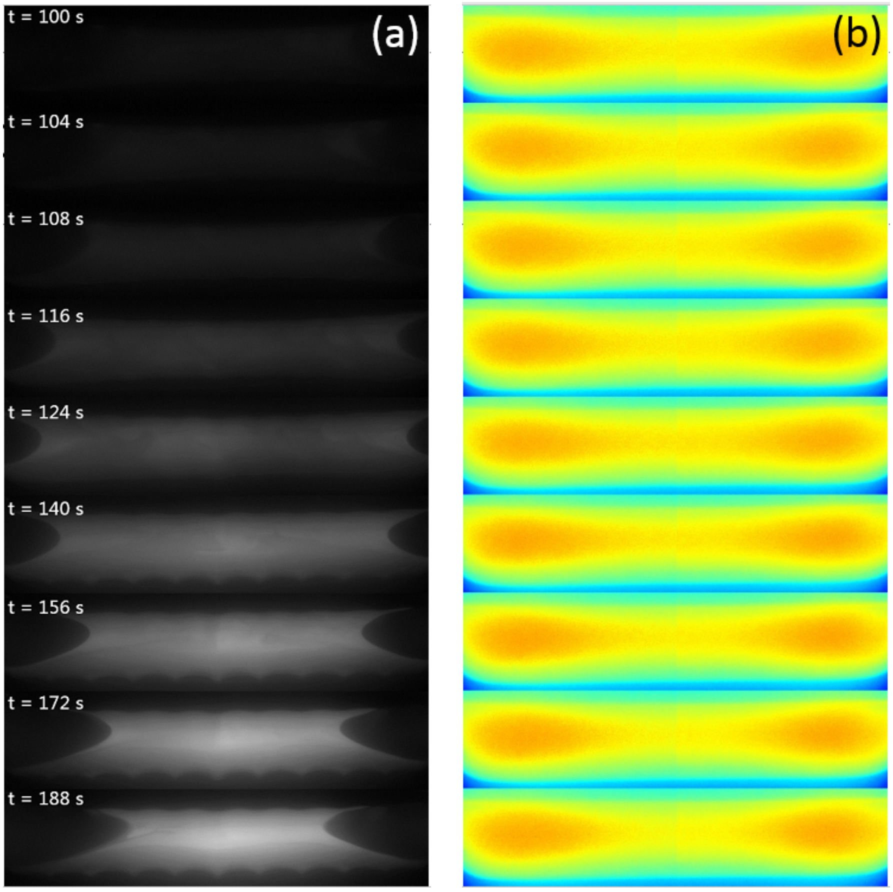

Figure 3.6: (a) LLS from silicon nanoparticles and (b) plasma emission during expansion and contraction of the dust cloud under conditions selected in Regime 1. The $SiH_4$/Ar plasma is maintained at 100 mTorr and 40 W.

### 3.3.1 Type 1 Behavior: Regime 1

At low pressures and high powers we observed periodic expansions and contractions of the dust cloud for the first time. As an example, Figs. 3.6(a) and 3.6(b) show LLS and plasma emission intensities, respectively, from a $SiH_4$/Ar plasma maintained at 100 mTorr and 40 W. Plasma emission intensity peaks off the symmetry axis of the electrodes, shown in Fig. 3.6(b). We infer, from the radial symmetry of our system, that the region where the plasma emission is high has the shape of a doughnut or a ring. We presume that the ionization rate is also high within this annular ring based on the similarities of the cross sections for ionization and excitations. The annular ring develops shortly after the initiation of the plasma and maintains this spatial distribution afterwards. In contrast, LLS intensity displayed in Fig. 3.6(a) shows radial expansion (100 s $<$ t $<$ 124 s) and contraction (124 s $<$ t $<$ 188 s) of the dust cloud.

We believe that the changing balance between the ion drag force and the electrostatic forces is responsible for the expansion and contraction of the particle cloud. The mechanism is similar to that proposed previously to explain the void formation in the center of the plasma and the heartbeat instability [45], in that they both involve the balance between the ion drag and the electrostatic force, but is different in that the shape and position of the void in our case lead to different nanoparticle cloud dynamics.

The ionization hot spot in the shape of a ring will develop a “small” positive space charge density $\rho_+$ , “small” in the sense that quasi-neutrality is still satisfied [13, 71, 72]. In addition, while $\rho_+$ is small over the entire hot spot, it does increase sharply close to the boundary between the dust cloud and the ionization hot spot. This is analogous to the case of a plasma near an absorbing wall: the difference in mobility between electrons and ions sets up an ambipolar field to speed up the ions and retard the electrons, except that the stationary absorbing wall is replaced by the moving dust cloud. Net space charge density profiles across such ionization hot spots and nearby dust clouds have been calculated through simulation [73, 74]. Specifically, Akdim *et al.* concluded that, for an argon dusty plasma maintained at 300 mTorr, the positive charge density $\rho_+$ is around $0.2 \times 10^8\, cm^{-3}$ in the center of the ionization hot spot and rises up to around $0.6 \times 10^8\, cm^{-3}$ near the dust cloud.

As a result of the positive space charge in the annular ionization ring, negatively charged particles in the dust cloud, especially those in the vicinity of the annular ring, are attracted towards it through electrostatic forces. Meanwhile, ions accelerated out of the annulus push the particles away from this region through the ion drag force. The electrostatic force that draws the particles radially outward and away from the center of the plasma scales linearly with particle radius $r_d$ while the ion drag force scales with $r_d^2$ (see derivations above or Refs. 67, 71). Thus, for small particles, electrostatic force pointing towards the annular ring dominates the ion drag force pointing away from the ring while the opposite is true for larger particles. We surmise that this is the reason why particles tend to spread out initially and the dust cloud expands (100 s $<$ t $<$ 124 s). It should be noted that these small particles almost certainly carry negative charges as TEM results indicated that the average particle diameter is about 30 nm. Repulsive Coulomb forces between the particles inside the dust cloud might have also contributed to the expansion of the dust cloud.

At some point later the particle cloud starts to contract because the particles have grown large enough such that the ion drag force pushing them towards the center, away from the annular ring, begins to dominate the electrostatic force. Thus, the annular ionization ring remains mostly devoid of nanoparticles. The time it takes for the dust cloud to expand and contract varies from experiment to experiment (3–5 minutes) even under the same pressure and power, but the expansion-contraction pattern is always observed in the parameter region (low pressure, high power) indicated as Regime 1 in Fig. 3.4.

If the dust cloud expands and contracts fast enough and finishes before approximately 3.5 minutes, we observe a second expansion for a small portion of the dust cloud while the majority of the dust cloud remains contracted in the radial center of the discharge (see Fig. 3.7(a), from t $=$ 213 s to t $=$ 272 s). The portion of the cloud that expands again eventually also contracts towards the center as shown in Fig. 3.7(a) (t $=$ 272 s to t $=$ 302 s). Comparison of plasma emission and LLS shows that the high intensity emission region still coincides nearly with the ionization annulus that is devoid of particles. We infer that these secondary expansions are associated with newly generated small nanoparticles (also observed from TEM results) as they move radially outwards due to the combined effect of electrostatic attraction towards the annular ring and repulsion from the negatively charged large particles in the dust cloud that remains contracted in the center. The electrostatic forces overcome the ion drag force for these newly generated small particles and push them towards the annular ring region. Once the newly generated particles grow large enough, they are also expelled from the annular ring by the ion drag force and another contraction is observed.

We should note that, it has been observed in some cases that these second-generation particles may not mix with the first-generation particles and that there is a boundary separating different generation particles [42,75,76] although no explanations or mechanisms were proposed. The CCD camera used in the present study does not have enough sensitivity and spatial resolution to capture such separatrix, especially when the second-generation particles grow large enough and start to scatter laser light intensively. The coexistence of particles from two different generations has been shown on TEM images before for the same reactor [70]. These particles were collected in the effluent after the plasma was turned off so that the two generations may have mixed as they flowed out of the system. Thus, we can not comment on the existence of a boundary that separates the two generations while the plasma is on.

In comparison, Dorier and his coworkers also alluded to the contraction and expansion of two dust particle layers, one layer near each electrode, in argon diluted silane plasma though only steady state images were reported [77]. The authors also reported that when silane flow was stopped, the dust cloud structure changed from two layers to an annular ring structure. Although at first sight the annular structure might look similar to our dust cloud structure, there are clearly major differences. In their annular structure, there are always particles near the periphery of the electrodes and these particles are connected to the dust cloud in the center via dust layers near the electrodes. The dust void region, if any, is also significantly smaller than ours. Moreover, this annular dust cloud structure disappears within 0.5 s once silane flow is restored.

Finally, we note that, the aforementioned modulation of the dust cloud near both electrodes was observed clearly in Figs. 3.6(a) and 3.7(a). Faster evolution and higher LLS intensities are observed at higher powers and pressures in this regime.

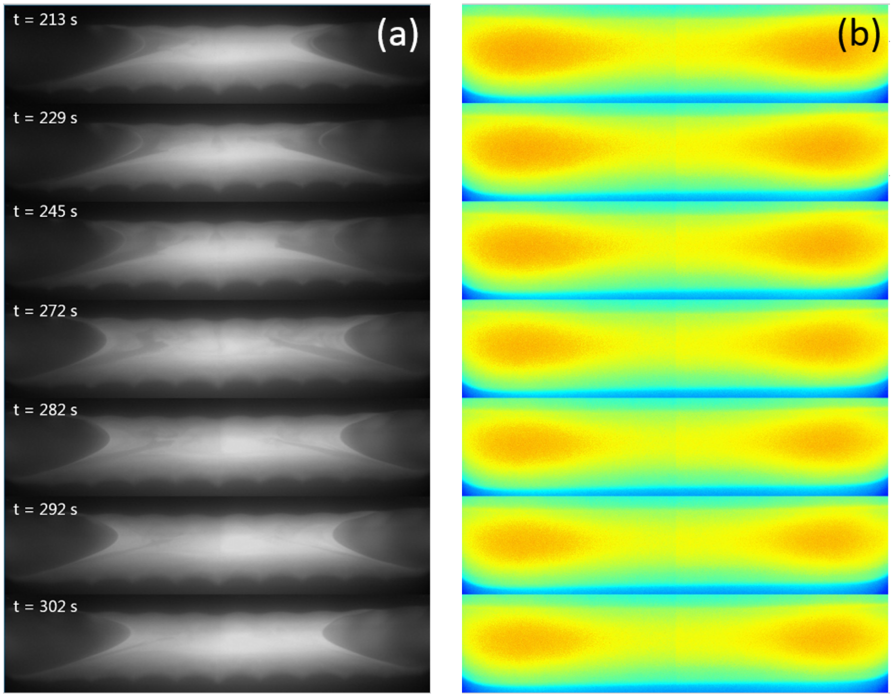

Figure 3.7: (a) LLS from silicon nanoparticles and (b) plasma emission during a second expansion and contraction of a small portion of the dust cloud. The $SiH_4$/Ar plasma is maintained at 100 mTorr and 40 W, *i.e.* under conditions selected from Regime 1.

### 3.3.2 Type 2 Behavior: Regime 2

At high pressures and low powers we observed a large stable region devoid of dust in the center of the plasma. As an example, Figs. 3.8(a) and 3.8(b) show the LLS and plasma emission intensities from a $SiH_4$/Ar plasma maintained at 100 mTorr and 20 W. As shown in Fig. 3.8(a), a dust void comes into shape in the center of the plasma after t = 105 s. After its initial formation, the size of the dust void remains almost constant over time, while the average LLS intensities in both the dust void and the surrounding dust cloud gradually increase. The spatial variation of the plasma emission in Regime 2 is different from that in Regime 1. Instead of peaking off-axis in an annular ring, the emission intensity is found to be highest at the center of the plasma, where the LLS intensity and particle density is low compared to the surrounding dust cloud, as shown in Fig. 3.8(b). Similar to the type 1 behavior at high powers and low pressures, plasma emission does not change significantly over time but the center region where the plasma emission is highest slowly gets smaller as LLS intensity and particle density increases slightly in the dust void (e.g., around t = 220 s). The region where the plasma emission is highest in Fig. 3.8(b) has approximately the same shape and size as the dust void in Fig. 3.8(a).

Similar to the void in the shape of an annular ring observed at low pressures and high powers (Regime 1), the dust void region observed in the center of the plasma at high pressures and low powers has higher emission and higher ionization rate because the electron density in this region is higher since there are few particles in the dust void to deplete electrons. This dust void also develops a small positive space charge compared to other places in the plasma. As a result, negatively charged particles near the dust void are attracted to it through electrostatic forces and at the same time expelled from the dust void through the ion drag force.

Previous experimental [42,78] and theoretical [79] studies have both demonstrated that dust voids act as nanoparticle nurseries: nanoparticles nucleate in these voids and are pushed out by ion drag as they grow larger. Since Rayleigh scattering intensity is proportional to $r_d^6/\lambda^4$ [80], where $r_d$ is the particle radius and $\lambda$ is the wavelength of scattered light, we see much weaker LLS intensities in the dust void where small nanoparticles nucleate. Small nanoparticles stay in the dust void due to the combined effect of electrostatic attraction from the dust void and expulsion from the large negatively charged particles in the surrounding dust cloud. For small particles, the electrostatic forces overcome the opposing ion drag forces pointing away from the dust void. As the nanoparticles grow larger, they are expelled into the surrounding dust cloud and towards the electrodes by the ion drag force and are eventually pumped out of the vacuum chamber.

As shown in Fig. 3.8(a), the structure of the dust cloud is highly symmetrical with respect to the horizontal mid-plane between the two electrodes. For the particles above the mid-plane, they experience ion drag and electrostatic forces in the opposite directions as compared to the particles below the mid-plane. The neutral drag, however, is always in the downward direction for all the particles. The fact that the dust cloud is still highly symmetrical with respect to the horizontal mid-plane indicates that the neutral drag force plays a much weaker role in the dust cloud dynamics compared to the ion drag and electrostatic forces. It should be noted that the center hole on the bottom electrode is about 1.5 mm in diameter while the other holes in the two-dimensional array on the electrode is about 1 mm in diameter. The slightly larger center hole might have contributed to the escape of the dust particles along the center axis, shown in Fig. 3.8(a), through a larger local gas flow rate and therefore neutral drag force. We further note that, modulation of the dust cloud near the bottom electrode, caused by the neutral drag force and holes on the bottom electrode, was much weaker in Regime 2 compared to that in Regime 1. Faster void formation and higher LLS intensities are observed at higher powers and pressures.

### 3.3.3 Type 3 Behavior: Regime 3

In Regime 3 with intermediate powers and pressures, the expansion-contraction pattern observed in Regime 1 and the large dust void pattern observed in Regime 2 both appear. Fig. 3.9 shows the LLS from silicon nanoparticles for a

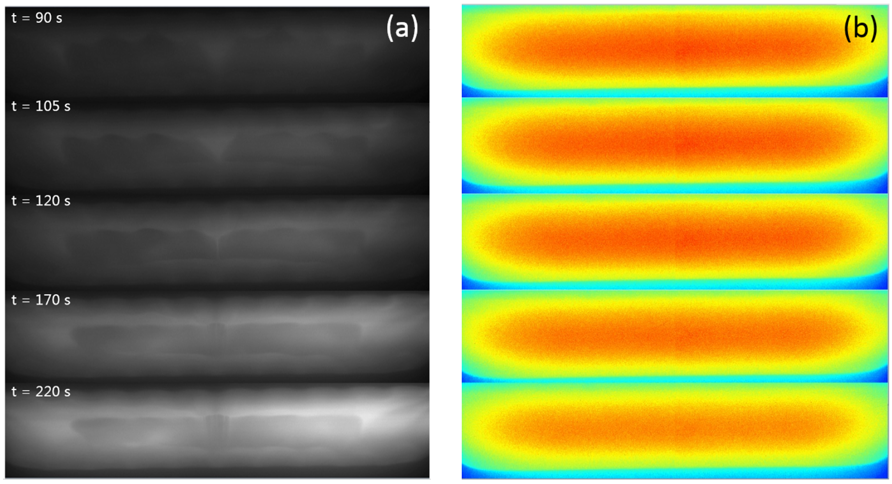

Figure 3.8: (a) LLS from silicon nanoparticles and (b) plasma emission as a function of time under conditions selected from Regime 2. The $SiH_4$/Ar plasma is maintained at 100 mTorr and 20 W.

$SiH_4$/Ar plasma maintained at 100 mTorr and 30 W. The dust cloud first expands radially outwards from t = 130 s to t = 160 s and then begins to contract, following the typical expansion-contraction pattern of Regime 1. However, between t = 280 s and t = 320 s, the dust cloud breaks into two portions, a small portion near the upper electrode and a much larger portion near the bottom electrode. Both portions shrink in size gradually while some particles start to appear near the edges of the electrodes. Later, from t = 370 s to t = 430 s, fewer and fewer particles remain in the center until eventually a dust void develops there, a typical pattern observed under the conditions of Regime 2. Thus, at intermediate powers and pressures between Regime 1 and Regime 2, we observe cloud dynamics resembling patterns observed in both Regime 1 and Regime 2 and the two patterns are connected by a transition stage during which the dust cloud breaks apart and a dust void forms. Faster evolution and higher LLS intensities are observed at higher powers and pressures.

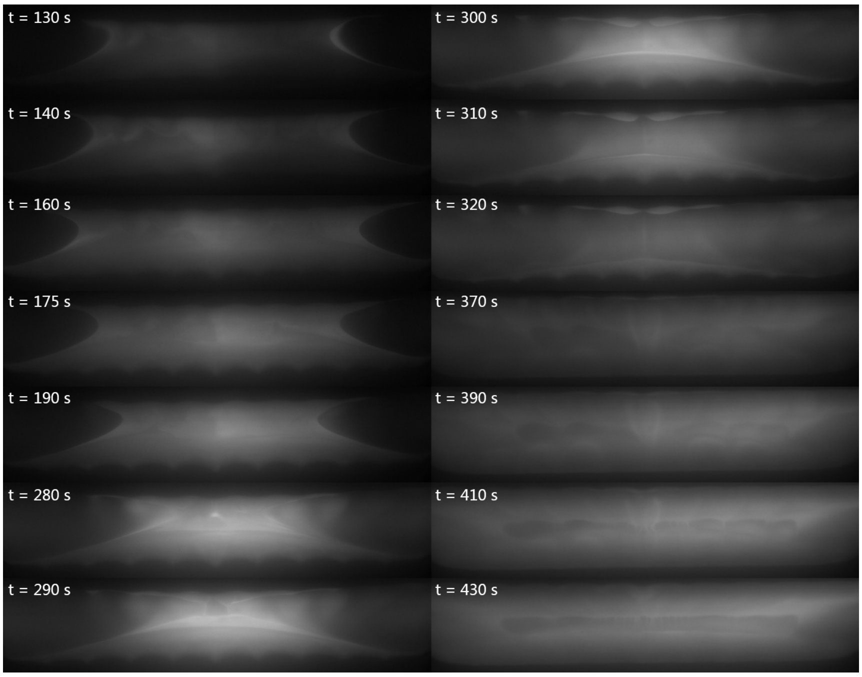

Figure 3.9: LLS from silicon nanoparticles as a function of time under conditions selected from Regime 3. The $SiH_4/Ar$ plasma is maintained at 100 mTorr and 30 W. We observe sequentially formation, expansion and contraction of a dust cloud between t = 130 s and t = 280 s. Following, the cloud transitions to a void by breaking into two dense regions, one near the upper electrode and another near the lower electrode.

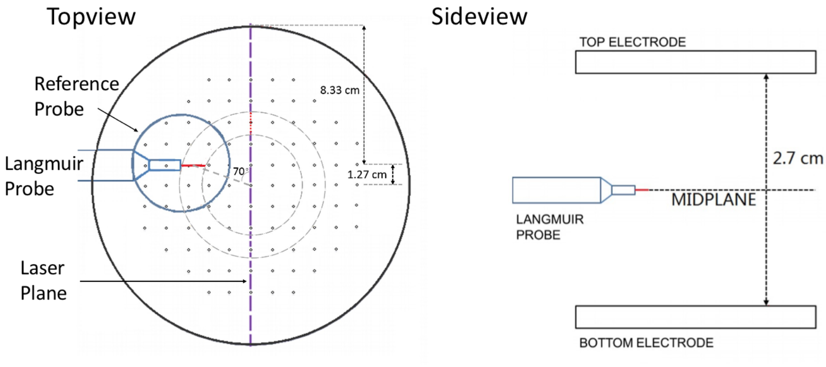

Figure 3.10: Topview (left) and sideview (right) of the Langmuir probe position. The region between the two gray dashed circles in represents the radial location where the probe is inserted. The probe tip (solid red line) is situated at a position rotated about 70° with respect to the plane of laser light scattering.

### 3.3.4 Ion Density Measurements

To complement the LLS experiments, we also conducted Langmuir probe measurements during a typical expansion and contraction cycle of the dust cloud observed in Regime 1. Specifically, we focused on the temporal evolution of ion densities at a specific location in the plasma as the dust cloud expanded and contracted. Ion densities were calculated from the Langmuir probe measurements in the ion saturation region assuming that the electron temperature, $\mathrm{T_e}$, is a very weak function of plasma parameters and remains constant at $3\,eV$, and that ions enter the probe sheath with the Bohm velocity (probe radius is 0.254 mm, on the order of Debye length). Electron temperature measurements conducted with a Langmuir probe have been reported before for the same reactor [70]. The Langmuir probe measurements showed, between t = 0 s and t = 150 s, a monotonic increase in $\mathrm{T_e}$ from $\sim$ 3.3 eV to $\sim$ 4.4 eV after the initiation of the dusty plasma. After t = 150 s, $\mathrm{T_e}$ remains fairly constant at 4.4 eV. We used 3 eV to obtain an order of magnitude estimate of the ion density.

Fig. 3.11 shows the dust cloud during its contraction and expansion in a $\mathrm{SiH_4/Ar}$ plasma maintained at 100 mTorr and 40 W. The red bar represents the radial location where the probe is inserted though the actual probe is situated at a position rotated about 70° with respect to the plane of laser light scattering (see Fig. 3.10). The probe is entirely immersed in the dust cloud between t = 90 s and t = 120 s. As the dust cloud continues to contract between t = 120 s and t = 160 s, the probe gradually emerges out of the dust cloud and is eventually entirely out of the dense part of the dust cloud at t = 160 s. Note, however, a small portion of the dust cloud starts to expand at t = 140 s during the contraction of the dense majority portion. Later the probe becomes entirely immersed in this small expanding portion at around t = 170 s. During its expansion, this small portion gains higher LLS intensity, comparable to that of the majority portion of the dust cloud, at t = 205 s. Following, the dust cloud

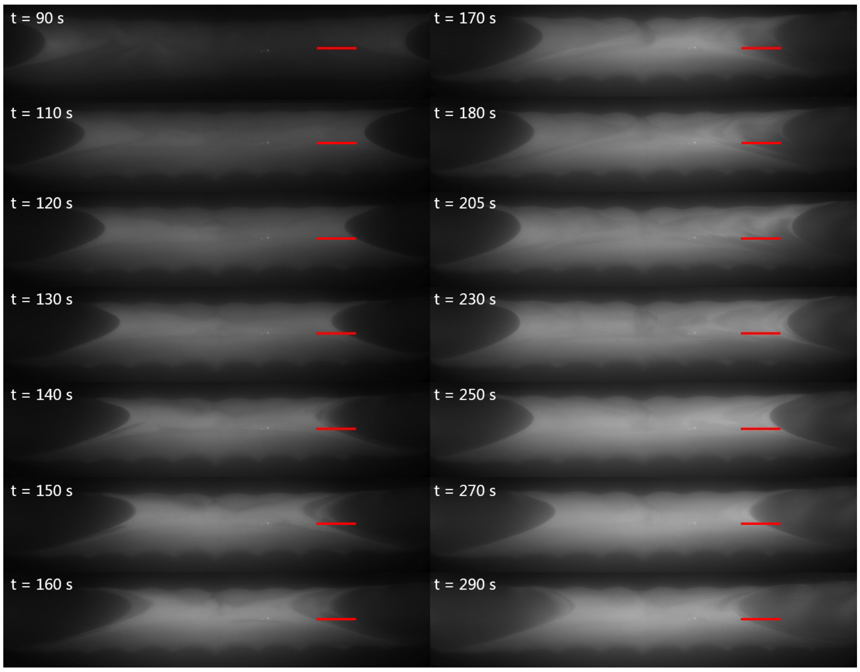

Figure 3.11: LLS from silicon nanoparticles with the Langmuir probe inserted in the plasma. The Langmuir probe's radial position is shown with a red bar. We note that the actual position of the Langmuir probe is rotated about 70° with respect to the laser plane (see Fig. 3.10). The $SiH_4$/Ar plasma is maintained at 100 mTorr and 40 W.

begins to contract again at around t = 230 s. At around t = 250 s, the probe begins to emerge out of the dust cloud again.

The red curve in Fig. 3.12 shows the ion density measurements corresponding to the LLS shown in Fig. 3.11. Ion densities are measured every 10 seconds for 5 minutes. As shown by the red curve, the ion density decreases until it reaches a minimum at around 120 s and then rises until around 170 s, at which point it starts to drop again. Interestingly, t = 120 s corresponds to the moment at which the probe starts to emerge out of the dust cloud and t = 170 s is the moment at which the probe becomes entirely immersed in the dust cloud (more specifically, the small expanding portion of the dust cloud that appears at around t = 140 s) again. Later, the ion density curve rises again at around t = 250 s, at which moment the probe starts to emerge out of the dust cloud again as the dust cloud undergoes a second contraction towards the center of the plasma.

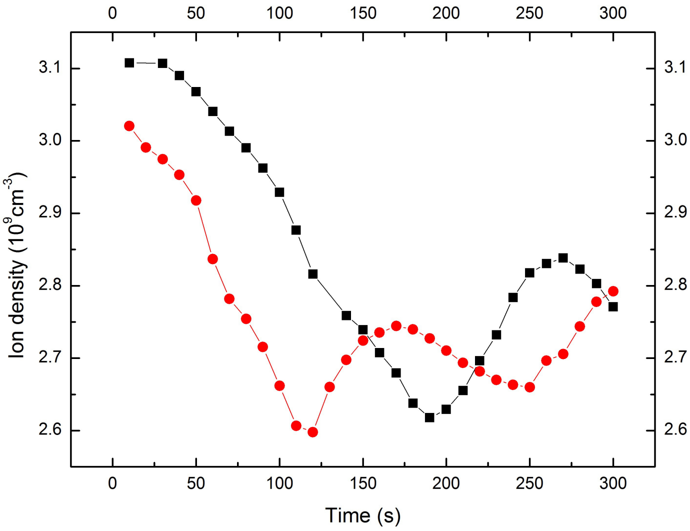

Figure 3.12: Ion density measurements conducted during typical expansions and contractions of the dust cloud in Regime 1. The $SiH_4$/Ar plasma is maintained at 100 mTorr and 40 W. The two sets of data were collected in two different experiments but under the same conditions.

The black curve in Fig. 3.12 is another set of ion density measurements under the same plasma pressure and power. Compared to the red curve, the black curve is shifted rightwards because this time the dust cloud contracts and expands slower. The ion density curve may reach its maxima and minima at different times from experiment to experiment, but it still has the same correlations with the corresponding LLS measurements: that is, ion density is lower when the LLS intensity around the probe is higher and vice versa.

A plausible explanation is that particles deplete electrons and thus lower local ionization rates and ion densities, assuming that the corresponding increase in electron temperature due to electron depletion is not significant enough. This is consistent with our earlier assertion that the annular ring region observed in Regime 1 and the dust void observed in Regime 2 have higher local ionization rates because these regions have much fewer particles compared to other places in the plasma. While the absolute values of the ion density measurements might not be accurate, we believe the consistently observed curve shape and its correlations with LLS measurements are accurate.

We should stress again that the ion densities discussed above are derived from the ion saturation current with the assumption that the electron temperature $T_e$ remains constant during the measurement. However, it is possible that a non-uniform electron temperature distribution exists, *i.e.* a higher electron temperature in or near the dust cloud and a lower electron temperature in the ionization hot spot. As the dust cloud contracts and expands, the electron temperature near the probe might adjust accordingly. Therefore the changes in the ion saturation current drawn by the probe could also be due to a changing electron temperature.

### 3.3.5 A Comparison of Regime 1 and Regime 2

We have shown in previous sections that Regime 1 and Regime 2 exhibit completely different particle dynamics, and in this section we will attempt to gain some insights on the cause(s) of this difference.

We will start by looking at the steady state spatial profiles of plasma emissions of pristine argon plasmas, maintained at the exact same pressures and powers as discussed above for the dusty plasmas. Fig. 3.13 shows the scaled plasma emission profiles at t = 100 sec for pristine argon plasmas maintained at 100 mTorr with powers of 40 W and 20 W. The maximum intensities of the original frames are around 25 for the 40 W argon plasma and 19 for the 20 W argon plasma. Both frames have been scaled (with two different scaling factors) to achieve the same maximum intensity for ease of comparison. The two argon plasma emission profiles at different plasma powers of 20 W and 40 W look very similar to each other and resemble that of the 20 W dusty plasma (Regime 2 with a dust void in the center). In other words, it seems that the particles generated in the 20 W dusty plasma have a relatively small impact on the plasma. On the other hand, for the 40 W dusty plasma case, the generated

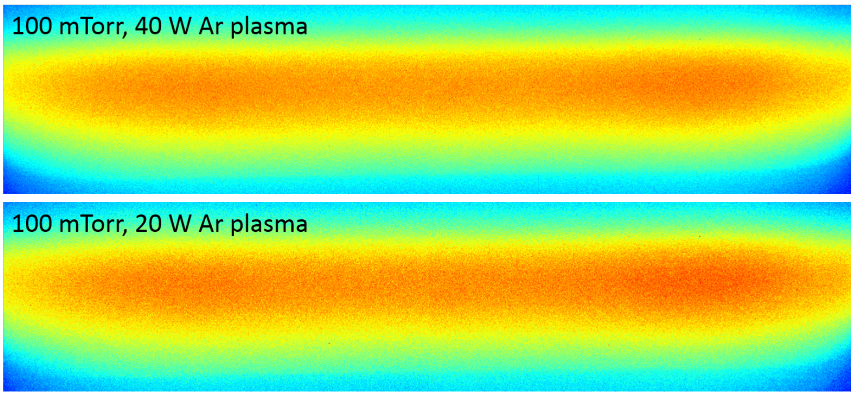

Figure 3.13: Scaled plasma emission profiles at t = 100 sec (steady state) for two pristine Ar plasmas maintained at 100 mTorr with powers of 40 W (top) and 20 W (bottom). The plasma conditions are exactly the same as the ones used for the dusty plasmas discussed above, except that the corresponding $SiH_4$ flow rates are replaced by Ar.

particles strongly modify the plasma and result in a different plasma emission profile. This could be due to a higher particle generation rate or/and particle growth rate at higher input powers.

It is worth noting again at this point that the plasma emission frames should be interpreted with caution. This is due to the fact that the entire plasma glows and therefore gets recorded by the CCD camera, but only one plane, the one in which the laser lies, is actually in focus with respect to the camera. When the overall variation in light intensity coming from that plane in focus is relatively small, which is indeed the case for these argon plasma emission pictures, some small features of the light intensity distribution in that plane can be smeared out by volume light.

In fact, some modeling studies (mostly done by Economou *et al.* [81–83] and Boeuf *et al.* [84, 85]) and probe measurements [86] have found that, for argon plasmas in parallel plate reactors, maxima of plasma density (which affects the emission intensity), at a given axial location, do not occur on the axial symmetry axis (*i.e.* $r = 0$), but rather can occur at some distances away from the symmetry axis. In other words, spatial profiles of plasma density in these reactors tend to have an “M” shape in the radial direction. These off-axis peaks were found to be more significant at higher RF voltages and can be close to non-existent at lower RF voltages. These off-axis peaks were also found to be more significant in parallel plate reactors with small gap distances (for example smaller than 3 cm, which is the case for our reactor). It is possible that we also have these off-axis peaks in our steady state 40 W argon plasma emission profile but we fail to identify them due to smearing issues. This "M" shape in plasma density could also facilitate the formation of an annular ionization hot spot in the 40 W dusty plasma case. The same modeling studies also found that plasma potentials tend to peak near the plasma density peaks. We note, however, this is not necessarily the case when the entire bulk plasma is quasi-neutral (*i.e.*, pristine plasmas without dust voids that can develop positive space charges or double layers). For example, modeling of (electropositive) methane CCP plasma (not a dusty plasma) within a parallel plate reactor has predicted similar off-axis plasma density peaks but the plasma potential peaks occur on the symmetry axis [87]. Similarly, Kushner *et al.* [88] reported from their simulation that, when the wafer (which served as the bottom electrode) diameter is set to 15 cm, ion flux maximum (usually found to coincide with density maximum) occurs off-axis while plasma potential has a primary maximum on the symmetry axis and a secondary local maximum off-axis.

Now we move on to look at the LLS and plasma emission intensities of the dusty plasmas again, only this time we focus on the early stage (*i.e.* $t < 15$ sec) intensity distributions, which have been neglected in previous sections. Fig. 3.14 shows the temporal evolution of scaled plasma emission profiles for dusty plasmas in Regime 1 (100 mTorr 40 W) and Regime 2 (100 mTorr 20 W) between $t = 1$ sec and $t = 15$ sec. For $t = 1$ sec and $t = 4$ sec plasma emissions are fairly uniform at both powers. Then the annular ring structure starts to become more obvious in the 40 W dusty plasma case while plasma emission is still fairly uniform in the center for the 20 W case between $t = 4$ sec and $t =$

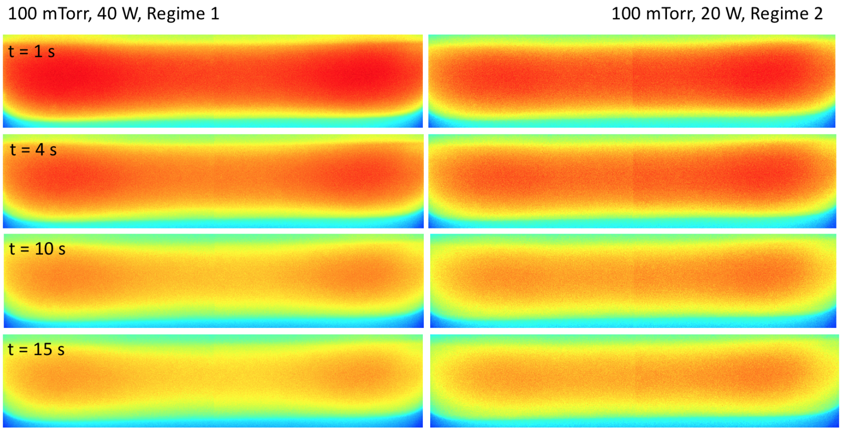

Figure 3.14: Scaled plasma emission profiles for dusty plasmas maintained at 100 mTorr with powers of 40 W (Regime 1) and 20 W (Regime 2). Two different scaling factors are used for the two different powers. Original maximum intensities are 45 for the 40 W plasma and 30 for the 20 W plasma.

15 sec. A possible cause for this difference is the existence of silicon particles discussed below.

Fig. 3.15 shows the scaled LLS intensities for the same dusty plasmas discussed in Fig. 3.14. It can be seen that particle distributions seem to be more uniform for the 20 W case, possibly due to overall smaller electric fields at low RF voltage and therefore less confinement on the negative ions that act as particle precursors [79]. If we assume that the 40 W dusty plasma has a higher particle nucleation rate and growth rate, then it follows that the depletion of electrons by particles is more severe in the 40 W case. Since the particles appear to be residing near the plasma center at these early times for the 40 W case, possibly due to a larger plasma potential in the center at these early times, it is reasonable to argue that these particles deplete electrons in the center region and therefore facilitate the formation of an annular ring with higher ionization and excitation rates observed in Regime 1. Then some small positive space charge starts to develop in the ring and gradually bends the plasma potential profile into an “M” shape. It should be stressed again, however, that the LLS intensities at these early times are extremely low (around 5 - 11 out of 256) and a difference in intensity of even one in the original frames can be exaggerated

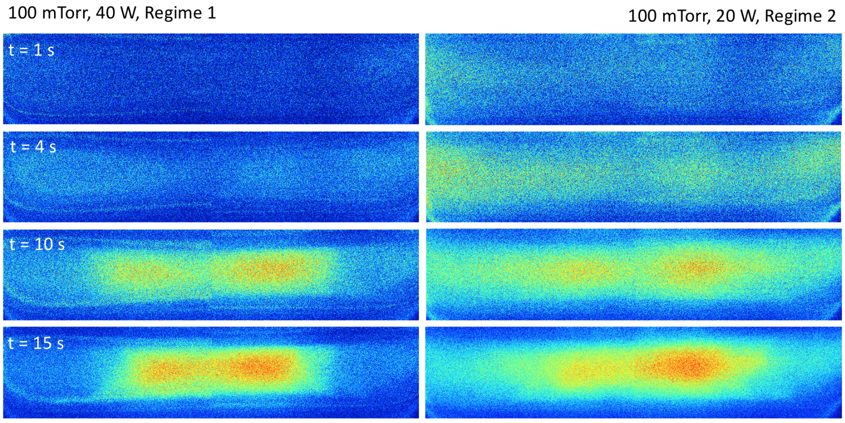

Figure 3.15: Scaled LLS intensity profiles for dusty plasmas maintained at 100 mTorr with powers of 40 W (Regime 1) and 20 W (Regime 2). To better visualize the particles, each frame uses a different scaling factor due to the fast evolving but extremely low scattering intensities at these early times.

many times in the scaled images, and therefore the interpretation of these early stage LLS images should also be viewed with caution.

## 3.4 Conclusion

We conducted LLS measurements in a 13.56 MHz capacitively coupled argon diluted silane plasma and studied the spatial distribution of silicon nanoparticles and nanoparticle agglomerates in the plasma. Specifically, we focused on the temporal evolution of the spatial distribution of nanoparticles. Nanoparticles form dust clouds with interesting spatiotemporal distributions whose dynamics depend on plasma power and pressure. Based on our observations, the spatiotemporal behaviors of the silicon nanoparticles are classified into 3 regimes in the pressure and power parameter space.

In Regime 1 with low pressures ($\sim$ 80–100 mTorr) and high powers ($\sim$ 40–60 W) we have observed periodic radial expansions and contractions of a continuous dust cloud. While appearing similar to the heartbeat instability, to the best of our knowledge the pattern we observed has not been reported before. Most periodic instabilities reported to date exhibit a radially expanding and contracting void that is situated at the center of the plasma. Instead, we observe an annular ring that is devoid of nanoparticles.

In Regime 2 with high pressures ($\sim$ 100–150 mTorr) and low powers ($\sim$ 20–40 W) we have observed a large stable region devoid of dust in the center of the plasma. This is more reminiscent of the nearly spherical voids reported previously but the void we observed is elongated radially and more elliptical than spherical, a difference that may be due to the low aspect ratio of our parallel plate electrode (large electrode diameter-to-gap ratio) as compared to previous experiments.

At intermediate pressures and powers between Regime 1 and Regime 2, assigned to Regime 3, both the radial expansion-contraction pattern and the large dust void pattern are observed. These two patterns are connected by a transition stage during which the dust cloud breaks into two portions vertically and then forms the dust void in the center of the plasma. Ion densities were also measured using a Langmuir probe. Lower ion densities were measured when the Langmuir probe was immersed in the dust cloud, as particles deplete electrons and thus lower local ionization rates. These measurements are consistent with our earlier assertion that regions with enhanced plasma emission (which are also regions devoid of particles) have higher ionization rates.

We hypothesize that the balance between the ion drag force and the electrostatic forces and their dependence on particle size are behind the observed particle dynamics but these forces and their balance change as a function of time and position in the plasma. Detailed description will certainly require two (perhaps three) dimensional modeling that can couple the charged species transport to nanoparticle nucleation, growth and transport.

These observations have demonstrated the diagnostic potential of spatially resolved LLS and plasma emission for dusty plasmas. Especially for the plasma emission profiles, they can be easily measured with the combination of a CCD camera, an optical band filter and a focusing lens, provided that the plasma chamber has a viewport. Observations of ionization hot spots, in the form of excitation hot spots, are often regions devoid of dust particles and are often the origin of various dust particle dynamics, due to the associated ion drag force and electrostatic forces.

# Chapter 4

# Fabrication of Anisotropic Plasmonic Nanostructures: Background

Part of this chapter has been published in *ACS Photonics* in Ref. 89.

While in previous sections our focus is placed on understanding dust particle dynamics in a CCP glow discharge, in the following sections we will focus on the application of a magnetically enhanced glow discharge, namely magnetron sputtering, as a critical deposition technique for the fabrication of anisotropic plasmonic nanostructures.

We will start by explaining why magnetron sputtering is the most suitable physical vapor deposition (PVD) technique for us and then move on to give a brief introduction to plasmonics. Both topics are necessary for the interpretation of the fabrication process and the unique plasmonic properties reported in Chapter 5.

## 4.1 A Comparison among Different PVD Techniques

The two most widely used PVD techniques are evaporation (either thermal or e-beam) and sputtering. One major difference between thermal and e-beam evaporation is that, both the crucible housing the material to be evaporated and the material itself are heated up in the former technique while only the material is sublimated (from its surface) in the latter case. Heating the crucible along with the material can cause impurity diffusion from the crucible to the material and contaminate samples. In addition, e-beam evaporation can deal with high melting point materials while thermal evaporation is limited to metals or low melting point materials.

E-beam evaporation, however, is not suitable for compound materials such as titanium nitride (TiN), which we will cover in the appendix. In addition to the fact that TiN is difficult to evaporate or sublimate, nitrogen also tends to escape during the process, resulting in a pure titanium film or significantly sub-stoichiometric TiN film on the substrate. One remedy for this problem was recently proposed by Ryynanen *et al.* [90] where the authors utilized a nitrogen ion source along with e-beam evaporation of pure titanium pellets. The authors did not specify the type of nitrogen ion source they were using but common ion sources involve the generation of plasmas themselves just like magnetron sputtering [91]. It should also be noted that the authors observed a higher impedance for their TiN film compared to those deposited by commercial magnetron sputtering systems. A higher impedance generally translates to unwanted red-shift and broadening of the plasmon resonance peak due to its negative impact on the coherent oscillation of plasmon electrons. In this regard, magnetron sputtering offers equal or better film quality with an easier setup.

Another advantage of sputtering over evaporation is the high level of energy possessed by the sputtered materials, usually around a few eVs, compared to typical values of 0.1 eV for evaporants. Energetic atoms move around on substrates, filling voids, or hit the underlying film harder and therefore form a higher density film with potentially better electrical and thermal properties. This is especially important when growing thin films. As will be discussed in detail later, the fabrication of plasmonic nanocups on templated wafers is essentially depositing a thin film of plasmonic material on the template.

Finally, due to its large angle distribution, evaporation techniques may require a special mask to ensure uniformity over a large area while at high ion bombardment energies sputtered materials are fairly unidirectional, an ideal feature for the glancing angle deposition (GLAD) technique, which we used for the fabrication of plasmonic nanorods.

Due to the reasons above, magnetron sputtering is chosen as the deposition method for our plasmonic nanostructures. For the fabrication of metal nanostructures such as copper and aluminum, the glow discharge generated by the magnetron sputtering source serves the pure purpose of creating ions for target bombardment while for compound materials such as TiN the glow discharge is also responsible for creating reactive nitrogen species. Due to the relatively inert background ($Ar/N_2$) and low pressure the magnetron sputtering processes are operated at, gas phase particle nucleation is very unlikely and the contamination problem of large particles falling on the deposited film is automatically avoided. We note, however, magnetron sputtering can also be used to synthesize particle clusters from metal, alloy and ceramic targets when operated at pressures higher or around 100 mTorr [92,93].

## 4.2 Diode Sputtering

In the most basic sputtering process, *i.e.* diode sputtering, energetic ions produced in the glow discharge bombard the target, which is also known as the cathode, and cause the removal of individual atoms or clusters of atoms from the target. Two major mechanisms have been proposed for the sputtering process, shown in Fig. 4.1 [94]. When the target surface is bombarded by relatively heavy ions, energy is imparted from heavy ions to the target near its surface and causes a collision cascade, during which some atoms get ejected from the target surface. Lighter ions, however, travel deeper into the target until they get reflected inside the target and hit atoms near the target surface on their way out, causing surface atoms to recoil and get ejected. For ions with intermediate mass, such as Ar ions, both sputtering mechanisms can contribute to the total sputtering yield, defined as the number of sputtered atoms per incident ion. These sputtered atoms can then condense onto substrates or any surfaces in the vacuum system.

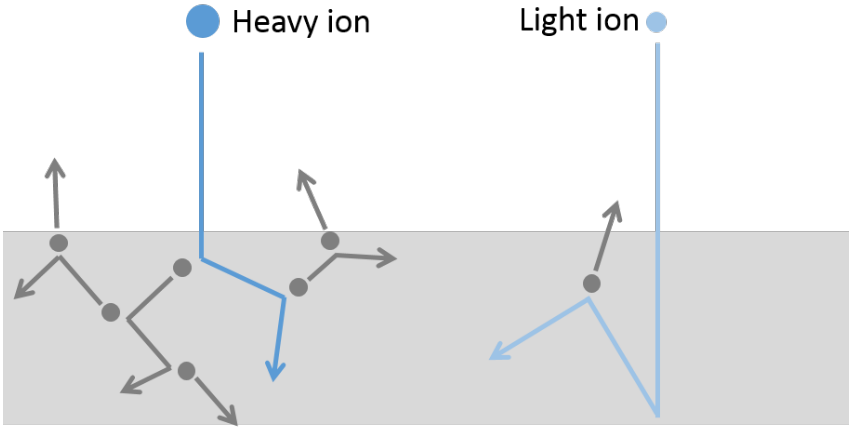

Figure 4.1: Schematic diagram of the two major sputtering mechanisms. The left case is for bombardment of relatively heavy ions while the right case is for relatively light ions. Redrawn from Ref.94.

Both experimental measurements [95–98] and simulation results [94,99] have shown that in most cases sputtering yield initially increases with incident angle, defined as the angle between the incident direction and the target surface normal. This is due to the fact that collision cascades happen closer to the target surface as the incident ions deviate from the surface normal. Once the incident angle passes a certain threshold, the specific value of which is largely dependent on the combination of ion energy, ion type and target material, sputtering yield starts to decrease as incident ions start to get reflected off the surface as groups of adjacent surface atoms start to prevent ions from entering the target.

Like any other glow discharges, secondary electrons are also emitted by the target (cathode) upon positive ion bombardment or neutral atom bombardment, and these electrons play an essential role in the conservation of discharge current and the sustaining of the glow discharge. This basic sputtering process has been known and successfully used since 1852 [100] for the deposition of various materials [101, 102]. However, it suffered severely from low ionization efficiencies and low deposition rates. When operating at low pressures, low ion densities result in low sputtering rates and thus low deposition rates. On the other hand, at high pressures the sputtered materials experience too many collisions with the background gas and may get scattered away from the substrates and again result in low deposition rates. These limitations were largely overcome in the early 1970s by the introduction of magnetrons into the basic sputtering process and a huge improvement was seen in the overall performance [103, 104].

## 4.3 Magnetron Sputtering

As the name suggests, magnetron sputtering utilizes magnets (either electromagnets or permanent magnets) to confine the electrons. In the presence of magnetic fields alone, electrons follow magnetic field lines and are confined in the transverse direction, circling around the magnetic field lines with the radius of gyration. When electric fields are added on top of the magnetic fields, more interesting electron dynamics arise. The part of the electric fields parallel to the magnetic field accelerate the electrons along the magnetic fields while the perpendicular part results in the so-called $\mathbf{E} \times \mathbf{B}$ drift. In magnetron sputtering, the common magnet configuration is placing one pole along the central axis of the target while shaping the other pole as a ring magnet around the outer periphery of the target. The magnetic field and the electric field are carefully designed such that the $\mathbf{E} \times \mathbf{B}$ drift forms an endless, circular racetrack for the electrons. A schematic of the working principle is shown in Fig. 4.2. Without collisions, collective effects or plasma instabilities, the electrons might be trapped in the racetrack indefinitely. It should be noted, however, that the loss of electrons to the anode is essential for completing the electrical circuit (especially in the direct current case) and therefore the magnetron sputtering process cannot be sustained without electron losses [105–107].

Confined electrons cause more ionizations and more ion bombardment of the target, resulting in higher sputtering rates and higher deposition rates. Moreover, an increased ionization rate allows the plasma to be maintained at lower pressures, usually around a few mTorr. As we will discuss later for glancing angle deposition, lower pressures decrease the number of collisions or the possibility of collisions for sputtered atoms and, therefore, lead to columnar microstructures with better qualities.

A molecular dynamics simulation of cluster emission from bombarded metal surfaces by Getz *et al.* found that, under 5 keV Ar ion irradiation, 57.9% of all the sputtered atoms are individual atoms while 32.3% are dimers and the rest are clusters of more than two atoms [108]. The authors also proposed that these cluster emissions are results of neighboring atoms receiving almost parallel momenta simultaneously from a cascade collision. It should be noted that the main emission mechanism of cluster emission discussed in the literature is named double collision mechanism [18,109–112]. This is due to the fact that,

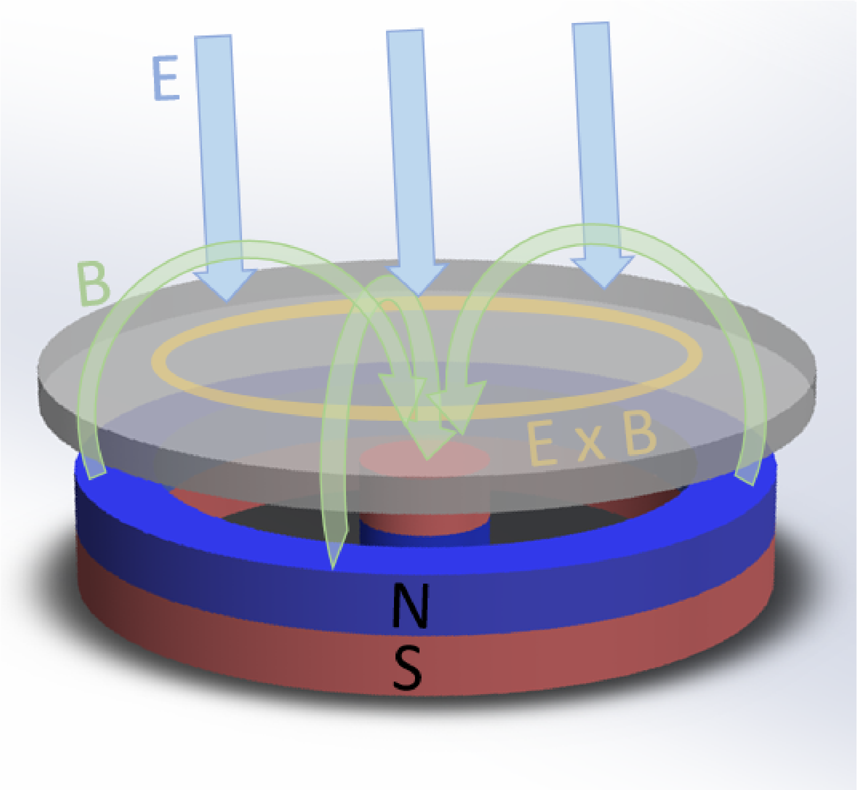

Figure 4.2: A schematic of the working principle of magnetron sputtering. With carefully designed **E** field and **B** field electrons in the glow discharge would travel in endless circles along the racetrack due to **E** × **B** drifts until knocked out by plasma instabilities and collisions.

for metals and semiconductors, the dissociation energy of a dimer is much smaller than the surface binding energy, therefore a dimer can hardly survive the emission process. Immediately after emission, however, the "dimer" atoms collide with each other and form a dimer again, meanwhile transferring the recombination energy back to the surface. Under normal operating voltages of magnetron sputtering, ion energies are only a few hundreds of eV and therefore the vast majority of the sputtered species will be individual atoms. Among those atoms approximately 1 out of 1000 is ionized [93].

### 4.3.1 Structure Zone Models

There are two different types of magnetrons, namely balanced and unbalanced magnetrons. In unbalanced magnetrons, the ring magnet at the target periphery is strengthened compared to the center pole, leaving some magnetic field lines open and directed at the substrate. Electrons can then travel along these open magnetic field lines and extend the plasma towards the substrate. As a result, a higher ion current can be extracted from the plasma to improve film quality on the substrate. To understand how ions contribute to better film quality, the well-known structure zone model(s) should be discussed [113].

Structure zone models for sputtered films [114–117] were developed since the 1970s to correlate process parameters with film properties. One key process parameter used in all structure zone models is the homologous temperature $T_h$, defined as the ratio of the substrate temperature to the melting point of the material being deposited, *i.e.* $T_h = T_s/T_m$. Here the substrate temperature $T_s$ is assumed to be mainly controlled by external heating elements such as cartridge heaters. At low $T_h$ the adatoms have very low mobilities and cannot move around on the substrate freely. Film growth in this condition then depends critically on the availability of the incoming flux. Inter-grain shadowing results in a porous columnar film, commonly known as zone 1. Higher $T_h$ allows surface diffusion of adatoms and results in a dense columnar film where the columnar structure still exists but no voids can be observed between columns, known as zone 2. Finally at still higher $T_h$ a dense film is obtained due to bulk diffusion, known as zone 3. This primitive structure zone model works fairly well for balanced magnetron sputtering deposition although in some cases the limited amount of ion bombardment from balanced magnetrons can still shift the threshold between different zones to lower temperatures. Bombarding ions can heat up the substrate locally, effectively raising substrate temperature $T_s$ at the bombardment site. In fact, P. J. Kelly *et al.* proposed a new structure zone model specifically for closed field unbalanced magnetron sputtering to explicitly include the impact of bombarding ions [113]. It should be noted that closed field in this case refers to the closing of magnetic field lines by mirroring multiple magnetrons, different from the closed field in a single balanced magnetron. In their model the authors chose homologous temperature $T_h$, ion-to-atom ratio and bias voltage as the process parameters. It was found that aluminum coatings deposited by closed field unbalanced magnetrons obtain zone 3 (dense film) structure at much lower $T_h$ than those deposited by conventional balanced magnetron sputtering.

In this study, two balanced magnetron sputtering systems at the University of Minnesota Nano fabrication Center (NFC) were used (AJA1 and AJA2) and, as we will show in the end, a custom-built angle sputtering system (balanced magnetron) is constructed to overcome the shortcomings of the NFC systems.

### 4.3.2 Reactive Magnetron Sputtering

Reactive magnetron sputtering is magnetron sputtering in the presence of chemically reactive gaseous species that react with the sputtering materials. These chemical reactions can occur at both the substrate and the target surface. While chemical reactions at the substrate surface are usually the purpose of reactive magnetron sputtering, the formation of compounds via chemical reactions on the target surface is undesired and known as target poisoning. Target poisoning can proceed through several mechanisms depending on the incoming particle type and energy [106,118–123]. First, low energy neutral species of the reactive gas can be chemisorbed on the target surface and form a thin compound layer. For target materials that have a high chemical affinity to the reactive gas, such as the combination of aluminum target and oxygen, this mechanism can play an important role. High energy inert ions from the glow discharge, such as Ar ions, can also bombard the target surface and cause recoil implantation of the adsorbed reactive atoms, resulting in a thicker compound layer. Similarly, high energy reactive ions, such as N ions, can be directly implanted into the target below the surface. Last but not least, the target surface can be at high temperature due to continuous ion bombardment and enable bulk diffusion of reactive atoms. Since the magnetron sputtering gun is usually water-cooled, this bulk diffusion process mostly happens in areas away from the cooling water. Generally the thickness of the compound layer is more than a few monolayers but the thickness can be significantly reduced near the racetrack region due to the dominant process of sputtering.

The formation of a compound layer on the target surface is often accompanied by a drastic drop in the sputtering rate and deposition rate, a sudden increase in the gas pressure, or more specifically, the reactive gas pressure, and a change in the stoichiometry of the deposited film [118–121, 124]. In addition, for dc magnetron sputtering, the plasma may even be extinguished if the compound layer formed on the target is a poor conductor, because the target serves as the cathode of the dc circuit. Therefore, the reactive gases, or the precursor gases for the reactive species, are usually introduced at certain distances away from the target surface to reduce target poisoning.

Initially when the reactive gas flow rate is relatively low, ion sputtering on the target is able to remove the thin compound layer immediately after its formation and prevent the target from being poisoned. However, at the mean time, due to insufficient reactive species, film deposition on the substrate can be significantly sub-stoichiometric. Increasing the reactive gas flow gradually in this regime can improve the stoichiometry until eventually ion sputtering cannot keep up with the formation rate of the compound layer and the target is poisoned. Therefore, introducing the reactive gas flow at appropriate flow rates and locations are of vital importance for film compositions. The reactive gas needs to be ionized and dissociated by the glow discharge but at the mean time cannot be too concentrated near the target.

In reactive magnetron sputtering, chemical reactions between the sputtering materials and the reactive gases are unlikely to occur in the gas phase as three-body reactions are required for the conservation of energy and momentum, which are highly improbable at the low operating pressures commonly seen in magnetron sputtering (about a few mTorr) [113, 124].

## 4.4 Introduction to Plasmonics

Owing to the tremendous advancement in both theoretical understanding of nanophotonics and fabrication techniques for nanostructures, plasmonic nanomaterials have received great attention in the past decades. When light interacts with a plasmonic nanomaterial, free electrons in the nanomaterial oscillate resonantly in response to the incident light, a phenomenon known as localized surface plasmon resonance (LSPR) in the case of nanoparticles and surface plasmon polariton in the case of metal-dielectric interfaces. Surface plasmons can enhance electromagnetic field intensity by several orders of magnitude, usually near sharp points or edges of the nanostructures or in the narrow space between neighboring nanostructures, and have been utilized in various applications such as surface enhanced Raman spectroscopy, first documented in 1973 [125]. In addition, surface plasmons can also result in far-field extinction (sum of absorption and scattering) near resonant wavelengths, opening opportunities for exciting applications such as photothermal treatment [126], plasmonic photocatalysis [127, 128], and new isotropic optical materials with specially tailored spectra across the whole electromagnetic spectrum from the UV to the infrared [129, 130].

The understanding of particle-light interaction dated back to the 1870s, when Lord Rayleigh first introduced the concept of oscillating electric dipoles to study the scattering phenomenon now known as Rayleigh scattering [131, 132].

When the particle under consideration is so much smaller than the wavelength of the incoming light, e.g. less than 15%, the phase of the electromagnetic irradiation can be assumed to remain constant across the entire particle, *i.e.* uniform electric field across the particle. Under this assumption the response of the particle to the electric field can be obtained by solving the Laplace equation for the scalar electric potential. By comparing the potential solution with that of a dipole, the effective dipole moment can be written as

$$\mathbf{P} = 4\pi\epsilon_m a^3 \frac{\epsilon_p - \epsilon_m}{\epsilon_p + 2\epsilon_m}\mathbf{E}\,, \tag{4.1}$$

where $\epsilon_m$ and $\epsilon_p$ are the dielectric constants of the surrounding medium and the particle itself, $a$ is the particle radius, $\mathbf{E}$ is the uniform electric field. The scattering cross section $C_s$, absorption cross section $C_a$ and total extinction cross section $C_e$ can then be written, respectively, as

$$C_s = \sigma_{geom}\frac{8}{3}(ka)^4\left|\frac{\epsilon_p - \epsilon_m}{\epsilon_p + 2\epsilon_m}\right|^2\,, \tag{4.2}$$

and

$$C_a = \sigma_{geom}4(ka)Im\left[\frac{\epsilon_p - \epsilon_m}{\epsilon_p + 2\epsilon_m}\right]\,, \tag{4.3}$$

and

$$C_e = C_s + C_a\,, \tag{4.4}$$

where $\sigma_{geom}$ is the geometrical cross section and $k$ is the wave vector in the medium. It can be easily observed that $C_e$ approaches infinity when $\epsilon_p = -2\epsilon_m$ and LSPR arises.

The vast majority of the research in plasmonic nanomaterials has been focused on nanostructures made of gold and silver. In addition to its non-toxicity and resistance to oxidation, gold has a strong plasmon resonance in the visible spectrum and can be readily fabricated into different nanostructures via solution phase synthesis [133–142]. Similarly, silver nanostructures [127, 143–147] have strong plasmon resonances near the blue end of the visible spectrum although they are less resistant to oxidation.

More recently, alternative plasmonic materials have seen a strong increase in attention, both to gain access to inexpensive and more abundant materials and also to broaden the spectral range of nanomaterial plasmonics. For example, aluminum offers a higher free carrier density than silver and gold and thus enables plasmonic nanostructures with resonances in the UV range of the spectrum [148, 149]. When in contact with air, however, a self-limiting oxide layer forms on the aluminum surface and results in an attenuation and red-shift of the LSPR. Copper is another potentially interesting plasmonic material though only a few studies have been reported to date. Chan *et al.* fabricated copper nanoparticles on glass and silicon substrates via nanoparticle lithography [150]. The authors showed size tunable LSPRs between $\sim$600 nm – 900 nm. Zong *et al.* studied the optical response of copper nanorods and nanowires embedded in aluminum oxide, prepared by alternating current electrodeposition [151]. This work showed some slightly tunable LSPRs around 550 nm. Chen *et al.* developed a hydrothermal route for nearly spherical and cubic copper nanoparticles and reported plasmon resonance between 600 nm and 800 nm [152]. Wang *et al.* fabricated copper nanoshells via seeded electrodeless plating and observed slightly tunable LSPRs between 600 nm and 850 nm [153].

In addition to the material's carrier density, the LSPR behavior can also be controlled by the shape of the nanomaterial. While spherical nanoparticles exhibit a single dipolar LSPR peak tunable via diameter, anisotropic nanostructures such as nanocups and nanorods offer greater control over LSPR wavelengths as they have more geometry parameters to manipulate. As a result of anisotropy, electron oscillations in different directions give rise to plasmon resonance peaks at different wavelengths. Specifically in the case of nanocups, the main plasmon resonance peaks are significantly red-shifted compared to those of spherical particles and nanoshells [154–156], usually right into the important near-infrared biological transparency window. Moreover, the transverse plasmon mode of nanocups scatters incoming light into the direction normal to the nanocup rim, irrespective of the incident direction over a large solid angle, making them ideal for directional light coupling [155, 156]. Very large near-field enhancements have also been observed near the sharp cup rims [157]. In the case of nanorods, two dipolar LSPR peaks can be observed, corresponding to electron oscillations in the longitudinal and transverse directions, respectively. The transverse LSPR is usually found at similar wavelengths as those for spherical particles with the same width (diameter) while the longitudinal LSPR appears at longer wavelength due to the large length in nanorods.

In the following sections, we will first discuss the plasmonic properties of close-packed yet discrete plasmonic nanocups fabricated by magnetron sputtering on colloidal templates in Chapter 5. Specifically, we fabricated both aluminum and copper nanocups and focused on the latter ones as they demonstrated sharper and stronger plasmon resonances. While nanocups were sometimes used interchangeably with half-shells or nanocaps, we adopt the more rigorous nomenclature [158] where nanocups strictly refer to dielectric cores with a shell coverage of more than 50 percent. We then move on to discuss the plasmonic properties of copper nanorods in Chapter 6, fabricated using essentially the same method as that for nanocups except that the deposition angle is rather small, commonly known as glancing angle deposition (GLAD). Finally in the appendix we will elaborate on our attempts to fabricate plasmonic TiN nanostructures, which led us to build our own angle sputtering system due to limitations of the NFC sputtering systems.

# Chapter 5

# Fabrication of Anisotropic Plasmonic Nanostructures: Copper and Aluminum Nanocups

Part of this chapter has been published in *ACS photonics* in Ref. 89. In this chapter we will focus on the fabrication and characterization of copper and aluminum nanocups. Sharp and tunable LSPRs in the infrared region are obtained from the copper nanocups using the proposed fabrication method. A potential application for these copper nanocups are low emissivity window coatings, which allow the visible light through yet reflect infrared heat.

While there are some wet chemistry synthesis methods for gold nanocups or half-shells [159–162], there is very limited if not none-existent literature regarding wet chemistry synthesis of nanocups from alternative materials such as copper and aluminum. For these alternative materials, Dorpe *et al.* [163] provided a comprehensive summary of the different fabrication methods for nanocups involving the use of dielectric cores. In their paper all the methods were classified into two categories. The first category utilizes chemical plating of dielectric cores to make complete nanoshells, part of which are then removed by anisotropic etching to yield nanocups. The other category starts with immobilization of dielectric cores on substrates, in either a close-packed or an irregular, sparse manner. Then, gas phase deposition such as electron beam evaporation and magnetron sputtering are employed to deposit materials on the dielectric particles. Due to the shadowing effects, the dielectric particles are partially rather than completely covered by the metal, yielding the shapes of nanocaps, half-shells or nanocups depending on the coverage percentage.

It is worth mentioning that, in the case of close-packed dielectric particles, the nanostructures subsequently deposited would link their neighboring nanostructures at equators or above, making them essentially interconnected half-shells or nanocaps, rather than discrete nanocups. The transport of electrons and plasmon coupling among adjacent nanostructures can result in unwanted broadening and shifting of plasmon resonances [164,165]. Interconnected nanostructures are also difficult to disperse in solvents due to their large sizes and masses, rendering them much less useful in solution phase applications or processings [166, 167]. The sparse template approach circumvents the interconnection issue but inevitably reduces the fabrication throughput as a large portion of the substrate is empty and wasted. Moreover, when the nanocups are to be used directly on the substrates, the sparse manner in which the nanocups are arranged results in lower magnitudes for the plasmon resonance peaks.

Here, instead of using a sparse template, we etch an initially close-packed polystyrene latex (PSL) particle template with reactive ion etching (RIE) to avoid nanocups and nanorods fusing at the equators. During RIE, the diameters of the PSL particles are reduced but they remain monodisperse provided that the initial PSL template is hexagonally close-packed. The nanocups are then fabricated by magnetron sputtering of corresponding targets onto RIE etched PSL templates in an argon environment. Tunability of the copper plasmon resonance peaks from 900 nm to 1500 nm, extending the typical tunability reported for other copper nanostructures between 600 nm and 1000 nm [151–153], is demonstrated by varying shell thickness and core PSL particle size. We also demonstrate that a potentially useful optical material that blocks near-infrared but transmits visible light can be constructed by mixing copper nanocups of three different sizes at appropriate ratios.

While the idea of using colloidal templates to assist the fabrication of plasmonic nanostructures has been explored by other researchers before [168–176] and summarized by Dorpe *et al.* [163], the vast majority of those studies focused on noble metals such as gold and silver, and the nanostructures, be them nanocups, nanocaps or half-shells, were often interconnected with neighboring nanostructures. One exception is the paper by Jian *et al.* [177], in which the authors experimentally and theoretically studied copper and aluminum nanocups fabricated on sparse colloidal templates. The authors reported LSPRs between 750 nm and 1000 nm for the copper nanocups and LSPRs at 500 nm for the aluminum nanocups. Despite the fact that the nanocups in their paper are embedded into a polymer film after fabrication and are therefore aligned in the same direction, we observed sharper and more resolved plasmon resonance peaks for our nanocups, measured randomly oriented as dispersed in solution. This suggests that during shell deposition an ordered colloidal template is vital for the formation of uniformly defined nanocups, and the geometrical variations in Jian *et al.*'s nanocups, as observed with atomic force microscopy, due to the use of sparse templates may have contributed to the widening of their LSPRs. As a result, better agreements between experimental and calculated extinction spectra are demonstrated in this study. We also report the absolute intensities of the plasmon resonance peaks, which were not reported in the paper by Jian *et al.*.

## 5.1 Experimental Setup

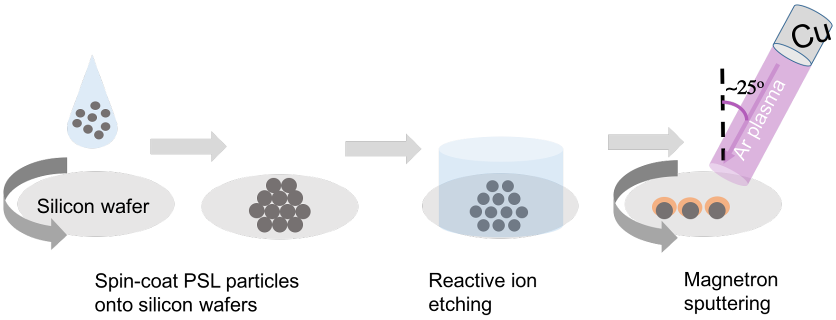

Figure 5.1: Schematic diagram of the fabrication process for the nanocups.

Fig. 5.1 shows the schematic diagram of the fabrication process for the nanocups. Prior to spin-coating PSL particles, silicon wafers are pre-cleaned in piranha solution at 120 $^o$C for 20 minutes, which not only removes organic residuals but also renders the wafer surfaces hydrophilic. A hydrophilic surface ensures a more even spread of the PSL water dispersion and therefore a more uniform coating of PSL particles. PSL particles of 200 nm (2.5 wt%) and 400 nm (10 wt%) dispersed in deionized (DI) water are purchased from Alfa Aesar and Bangs Laboratory, respectively. In preparation for the spin-coating, the 200 nm PSL dispersion is further diluted with DI water to 1.5 wt%. The 400 nm PSL dispersion is diluted with a 1:1 mixture of DI water and Triton X-100 in methanol (1:400) to 3.33 wt%. A monolayer of hexagonally close-packed PSL particles can be obtained with appropriate combinations of dispersion weight concentration, dispersion viscosity, spinning speed and spin-coating time. In our case, we found that when the weight concentration is relatively high (3.3 wt% for the 400 nm PSL and 1.5 wt% for the 200 nm PSL), a medium spinning speed (500 rpm for 200 nm PSL and 900 rpm for 400 nm PSL) generally leads to an ordered, hexagonally close-packed monolayer template.

Following the PSL spin-coating, the close-packed template is placed in a reactive ion etching (RIE) chamber and etched in an $O_2$ (50 sccm)/$CF_4$ (2 sccm) plasma at 100 mTorr and 50 W. Two different reactive ion etchers were used in the present study (STS 320 PC and AV Etcher Vision 300) and similar templates can be achieved given the right amount of etching time despite the different etching rates between them. The lower limit of the PSL particle size after RIE is mostly restricted by uniformity and repeatability of the dry etch process. For the two RIE etchers used in this study, the lower limit is around 135 nm, below which PSL size uniformity starts to deteriorate drastically. Average particle size also becomes increasingly sensitive to etching time (controlled manually in this study) as the particles get smaller. For best uniformity and repeatability, target PSL particle size is set above 135 nm in all templates. After RIE, the non-close-packed template is placed on a rotating stage and a thin metal film is deposited onto the template by magnetron sputtering, which creates well-separated and well-defined nanocups. The sputtering gun is tilted at $25^o$ off the substrate normal. The base pressure of the deposition chamber is lower than $10^{-6}$ Torr and the deposition pressure is $5 \times 10^{-3}$ Torr. An entire $4''$ wafer templated with etched PSL particles can be used for deposition and no noticeable difference is observed for nanocups from different parts of the wafer. We note that, to ensure monodisperse PSL particles after RIE, a hexagonally close-packed template is required to begin with. The hexagonally close-packed structure guarantees that every PSL particle has approximately the same surroundings. During RIE, any differences in surroundings can be magnified and result in PSL particles of irregular shapes and polydisperse sizes. A comparison between initially hexagonally close-packed and randomly arranged PSL particles after RIE is shown in Fig. 5.2.

After deposition, the samples are cleaved into small pieces and sonicated in toluene (for aluminum nanocups or copper nanocups) or a 1:1 mixture of toluene and acetic acid (for copper nanocups) for about 20 seconds. Toluene dissolves the PSL particles and releases the nanocups from the substrates into

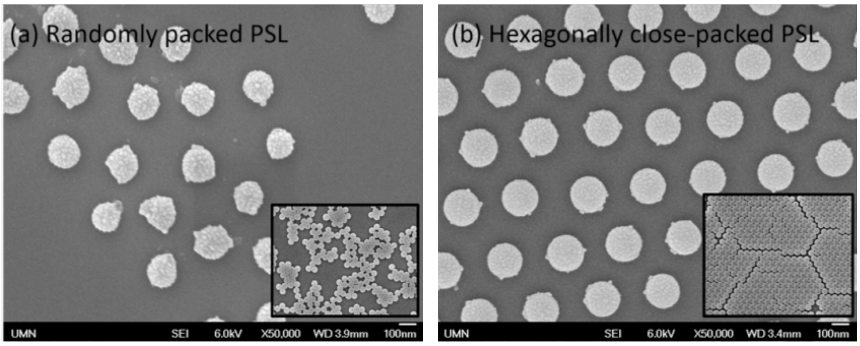

Figure 5.2: Topview scanning electron microscopy (SEM) images of (a) randomly packed and (b) hexagonally close-packed PSL particles after RIE. Insets are topview SEM images before RIE.

the dispersion. Acetic acid removes the surface oxides of the copper nanocups. Extinction spectra are then measured for the nanocup dispersion using Cary 5000 UV-VIS-NIR spectrometer. Nanocups on an area of about 3.7 cm by 3.7 cm are used to prepare the dispersion for each extinction spectrum measurement. Oxidation studies for the copper nanocups are conducted by measuring the extinction spectra immediately, 3 days, 7 days and 13 days after fabrication, respectively, in pure toluene. Unless otherwise specified, the extinction spectra reported are the absolute values (not scaled).

To reveal the nature of the LSPR peaks, the optical properties of the nanocups are numerically investigated by our collaborators using COMSOL®. Initial geometrical parameters of the nanocups in the calculations are estimated from scanning electron microscopy (SEM) images and metal deposition rates on a bare wafer. Then they are further adjusted by comparing the calculated extinction peaks with the measurements. We specifically focused on the main plasmonic extinction peak, which turned out to be sensitive to both the metal film thickness and the size of the smallest features (*i.e.*, edge of the nanocup). In general, the main plasmonic extinction peak red-shifts with reducing thickness of the metal film or rounding radius of the edge. A 3 nm $Al_2O_3$ layer around the aluminum nanocups is included in the model to account for the unavoidable oxidation of aluminum [178]. The dielectric constants of copper and aluminum are taken from Refs.179 and 180. The refractive indices of the matrices are given by $n_{\text{matrix}} = 1.44$ (1:1 volume ratio of toluene to acetic acid) and $n_{\text{matrix}} = 1.50$ (toluene) for the copper nanocups and the aluminum nanocups, respectively. The refractive index of the $Al_2O_3$ oxide layer is given by $n_{\text{oxide}} = 1.76$. We calculated the optical responses of the nanocups for different polarizations and wavevectors: $\{\mathbf{E} \parallel z, \mathbf{k} \parallel x\}$, $\{\mathbf{E} \parallel z, \mathbf{k} \parallel y\}$, $\{\mathbf{E} \parallel x, \mathbf{k} \parallel z\}$, $\{\mathbf{E} \parallel y, \mathbf{k} \parallel z\}$, $\{\mathbf{E} \parallel y, \mathbf{k} \parallel x\}$, $\{\mathbf{E} \parallel x, \mathbf{k} \parallel y\}$, where $x$, $y$ are perpendicular to the nanocups axis and $z$ is parallel to the nanocup axis. The final extinction spectra of the nanocups presented in this thesis were averaged over the orientations.

## 5.2 Results and Discussion

### 5.2.1 Copper Nanocups

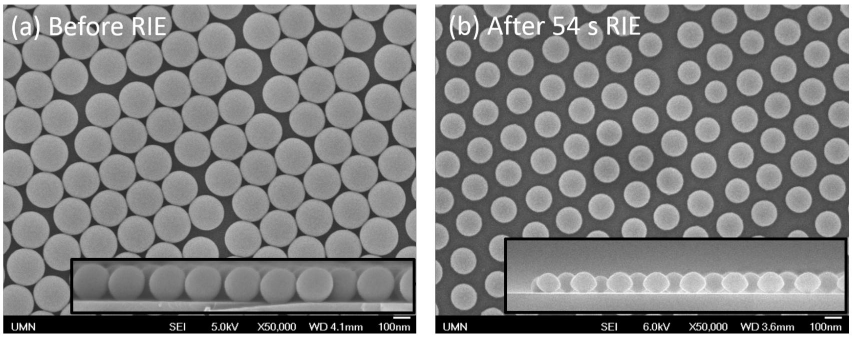

Figure 5.3: Topview and sideview (insets) SEM images of 200 nm PSL particles (a) before and (b) after 54 sec of RIE at 100 mTorr and 50 W.

Copper nanocups are deposited on etched PSL templates using the described method. Topview and sideview (insets) scanning electron microscopy (SEM) images of PSL particles before and after 54 sec of RIE at 100 mTorr and 50 W are shown in Fig. 5.3. The hexagonally close-packed structure of the PSL particles before RIE is clearly displayed in Fig. 5.3 (a). Due to anisotropic etching, the initially spherical PSL particles obtain an oval shape after RIE, shown in inset of Fig. 5.3 (b). The PSL particles remain monodisperse while their horizontal diameters are reduced from 200 nm to 146 nm after RIE. A thin copper film is then deposited onto the etched PSL template via direct current (DC) magnetron sputtering for a period of 132 sec. Topview and sideview SEM images of the copper nanocups are shown in Fig. 5.4 and its inset.

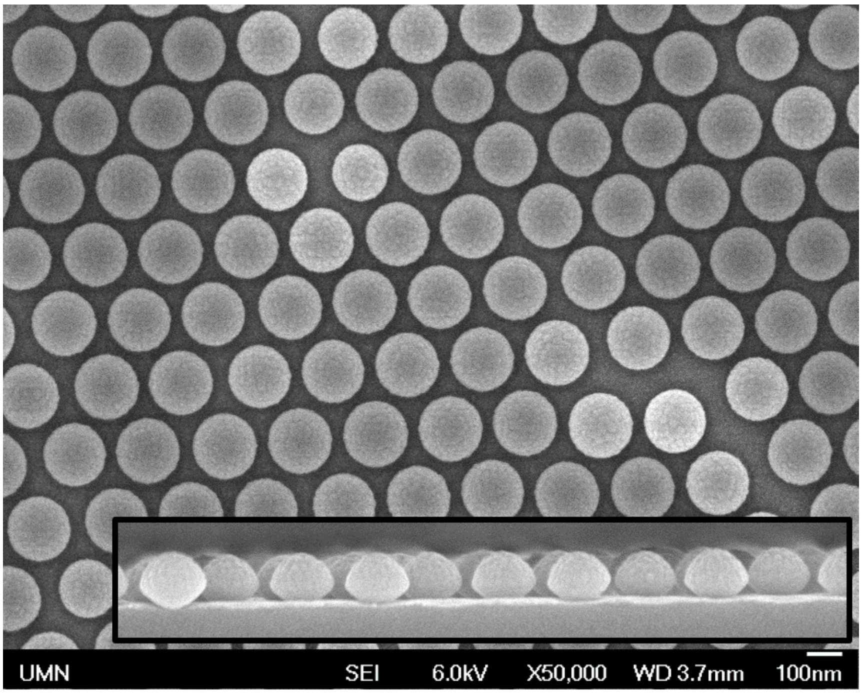

Figure 5.4: Topview and sideview (inset) SEM images of the copper nanocups deposited on 146 nm non-close-packed PSL template via DC magnetron sputtering for a period of 132 sec.

Fig. 5.5 shows the geometry model and extinction spectra of the copper nanocups dispersed in toluene and acetic acid. The background extinction below 600 nm is due to the interband transition of copper from the 3d band to the conduction band. Three plasmon resonance peaks can be observed around 600 nm, 740 nm and 1000 nm. We should note that all extinction spectra measured in this study are for dispersed nanocups along with dissolved polystyrene. Extinction contribution from polystyrene alone, at the same concentration as in the mixture of nanocups and dissolved polystyrene, is minor and flat around 0.025 across the entire extinction spectrum. Therefore, no purification procedures are carried out in this study to separate the nanocups from dissolved polystyrene. The calculated extinction spectra of the copper nanocups, dashed black curve in Fig. 5.5 (b), agree well with the measured spectra (solid black curve). To better understand the resonance behaviors of the plasmons in the copper nanocups near the extinction peaks, our collaborators calculated the field and charge distributions, shown in Fig. 5.6. The extinction maximum near $\lambda = 1000$ nm is caused by the strong dipole-like plasmonic resonance perpendicular to the symmetry axis of the copper nanocup. This plasmonic resonance occurs when the symmetry axis of the nanocup is perpendicular to the electric field. The extinction maximum near $\lambda = 720$ nm is contributed by dipole-like plasmonic resonances both along and perpendicular to the symmetry axis of the copper nanocup. The former resonance is excited when the symmetry axis is aligned with the electric field and perpendicular to the light wavevector while the latter is excited when the symmetry axis is perpendicular to both the electric field and wavevector. The extinction peak near $\lambda = 600$ nm is caused by complex multipolar plasmonic resonances. To excite these multipolar resonances, the symmetry axis of the nanocup should be perpendicular to the electric polarization, and be either parallel or perpendicular to the light wavevector.

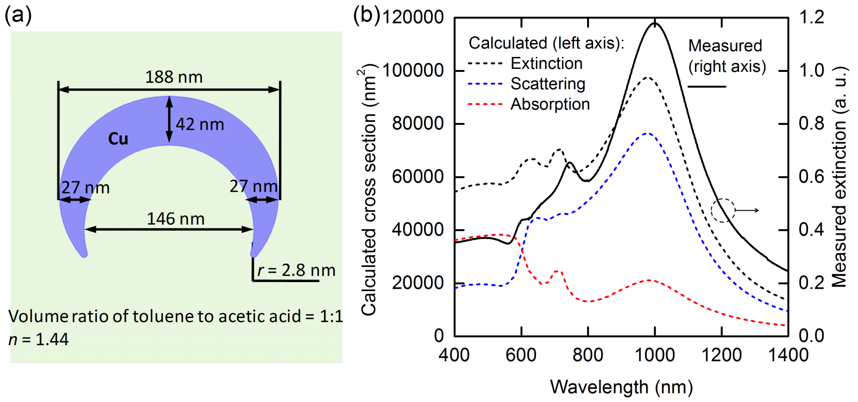

Figure 5.5: (a) Geometry model of the copper nanocups. (b) Measured extinction spectrum and calculated scattering, absorption and extinction cross sections of copper nanocups dispersed in a 1:1 mixture of toluene and acetic acid.

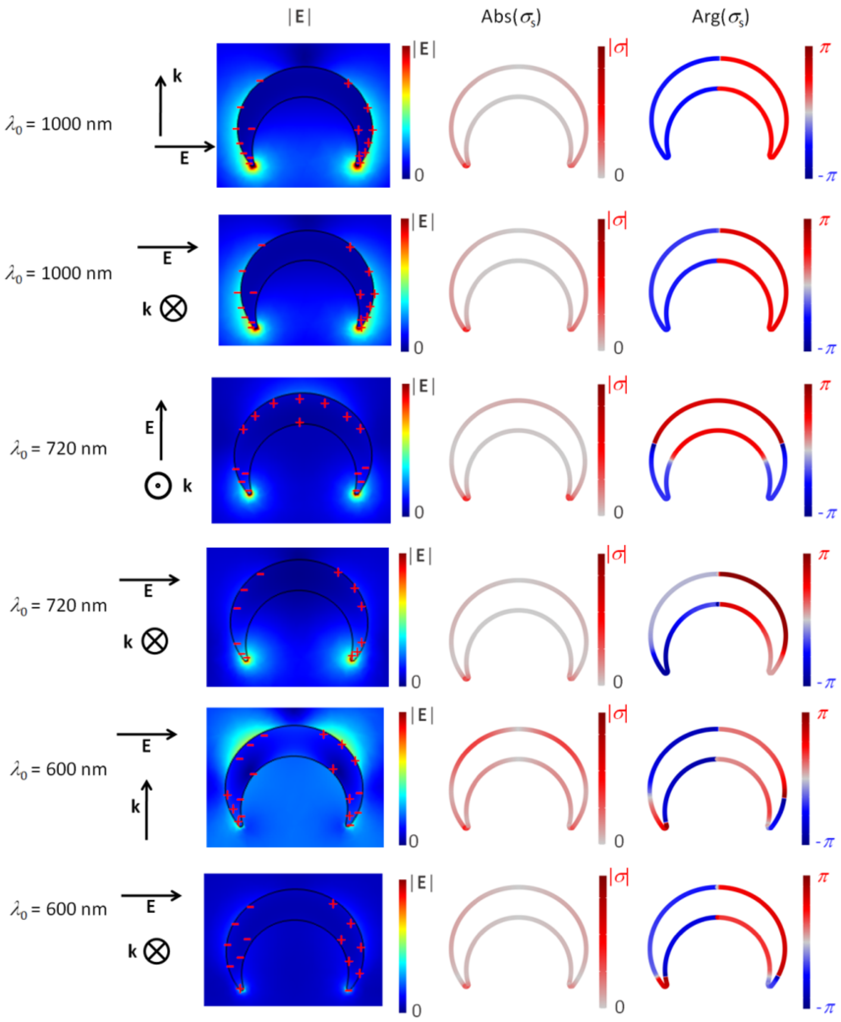

Figure 5.6: Field maps $|\mathbf{E}|$ and charge distributions $\sigma$ at the cross section of the copper nanocup near the extinction peaks.

### 5.2.2 Aluminum Nanocups

Similarly, aluminum nanocups are fabricated on the as-prepared PSL templates via radio frequency (RF) sputtering for 10 min. Topview and sideview SEM images of the aluminum nanocups are shown in Fig. 5.7 and its inset.

Fig. 5.9 (a) shows the geometry model of the aluminum nanocups. Fig. 5.9 (b) shows the extinction spectrum measured with the aluminum nanocups dispersed in toluene, and also the calculated extinction, scattering and absorption cross sections. Two plasmon resonance peaks around 580 nm and 990 nm can be observed. Again, the calculated extinction spectra agree well with the measured

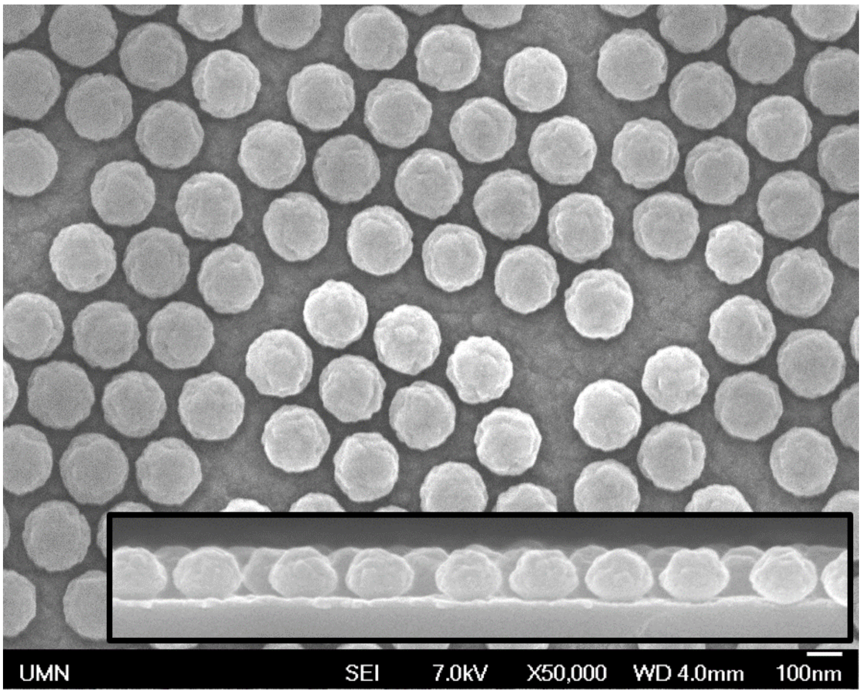

Figure 5.7: Topview and sideview (inset) SEM images of the aluminum nanocups deposited on 146 nm non-close-packed PSL template via RF magnetron sputtering for a period of 10 min.

one.

As demonstrated in the field and charge maps in Fig. 5.8, at the extinction maximum near 1000 nm, the plasmons oscillate in dipole-like behaviors. The strong dipole-like plasmons can be excited in the direction either perpendicular or parallel to the symmetric axis of the aluminum nanocup. For the first case, the symmetry axis needs to be perpendicular to the external electric field with an arbitrarily oriented wave wavevector. For the latter case, the symmetry axis should be aligned with the external electric field, and perpendicular to the light wavevector. The extinction maximum near 600 nm is mainly attributed to the horizontal dipole-like plasmonic resonance and also partly to the vertical dipole-like resonance and complex multipolar resonances. Near this wavelength, the strong horizontal dipole-like resonance is excited when the symmetry axis of aluminum nanocup is perpendicular to both the external electric field and the light wavevector. The complex multipolar resonance is excited when the symmetry axis of the nanocup is perpendicular to the electric field but parallel

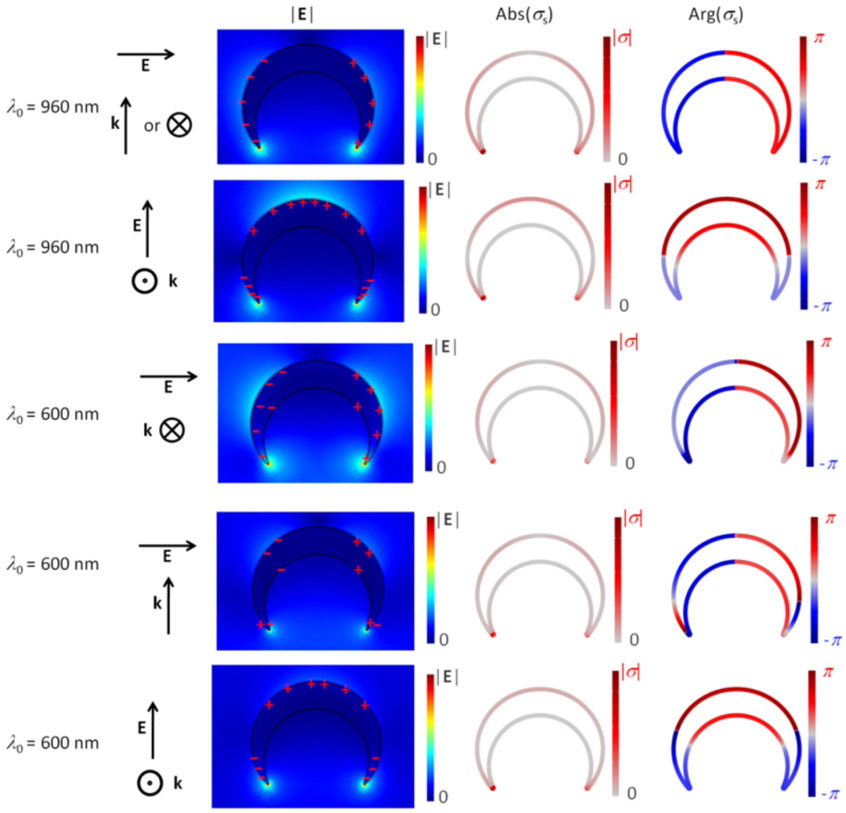

Figure 5.8: Field maps $|\mathbf{E}|$ and charge distributions $\sigma$ at the cross sections of the aluminum nanocups near the extinction peaks.

to the wavevector. The vertical dipole-like resonance is excited when the symmetry axis is parallel to the electric field and perpendicular to the wavevector.

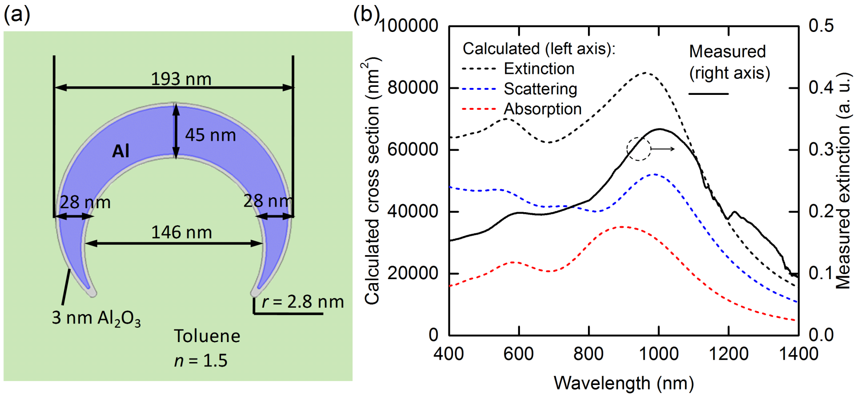

Figure 5.9: (a) Geometry model of the aluminum nanocups. (b) Measured extinction spectrum and calculated scattering, absorption and extinction cross sections of aluminum nanocups dispersed in toluene.

The good agreements between experimental and calculated extinction spectra found for both copper and aluminum nanocups validate the geometry model and suggest that the shapes of the nanocups are well-defined. Overall, the plasmon resonance peaks of the copper nanocups are much sharper and stronger than those of the aluminum nanocups. For this reason, the rest of the present study is focused on copper nanocups.

### 5.2.3 Tuning Plasmon Resonance of Copper Nanocups

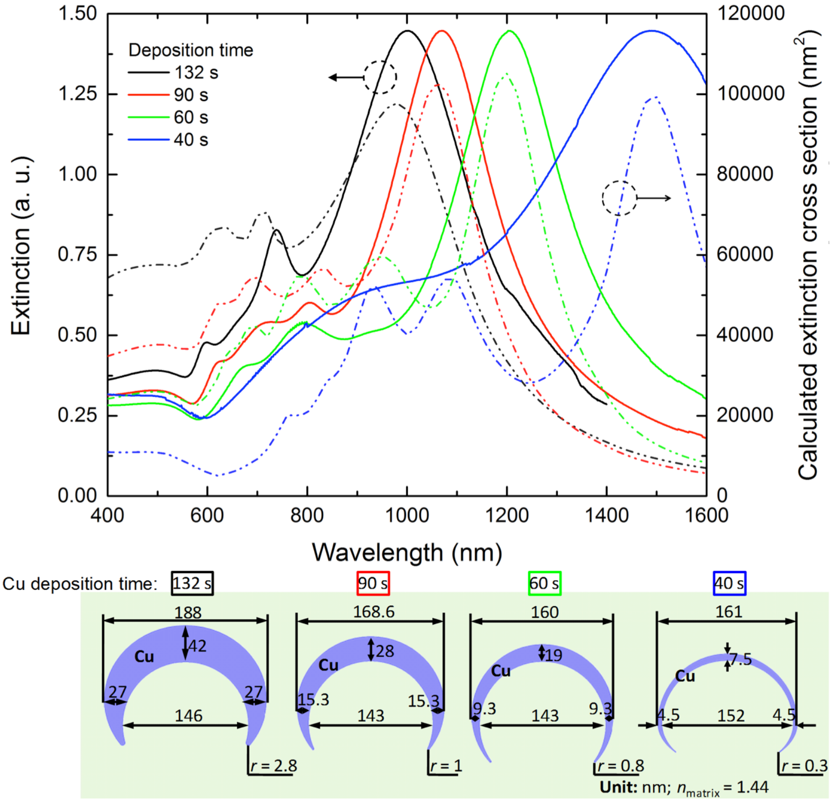

Figure 5.10: Measured extinction spectra (solid) and calculated extinction cross sections (dashed) for copper nanocups with different deposition times between 40 sec and 132 sec. The measured (solid) curves are scaled to the maximum of the solid red curve for easy comparison. Geometry models of the nanocups used in the simulation are shown at the bottom.

To tune the LSPR peaks of the copper nanocups, DC magnetron sputtering deposition time is varied between 40 sec to 132 sec, yielding copper nanocups of different shell thickness. Extinction spectra for copper nanocups with deposition times of 40 sec, 60 sec, 90 sec and 132 sec, respectively, were measured in a 1:1 mixture of toluene and acetic acid, shown as the solid curves in Fig. 5.10. All of the four measured (solid) curves are scaled to the maximum of the red curve (90 sec deposition time) for easy comparison.

Table 5.1: Geometry parameters for the simulation.

| Model # | Deposition time (s) | Main plasmon resonance wavelength (nm) | Cu thickness, top (nm)[a] | Cu thickness, side (nm) | Rounding radius at cup edge (nm) | Total diameter (nm)[b] | PSL template diameter (nm)[b] |
|---|---|---|---|---|---|---|---|
| 1 | 132 | 1000 | 42 | 27 | 2.8 | 188 | 146 |
| 2 | 90 | 1065 | 28 | 15.3 | 1 | 168.6 | 143 |
| 3 | 60 | 1200 | 19 | 9.3 | 0.8 | 160 | 143 |
| 4 | 40 | 1490 | 7.5 | 4.5 | 0.3 | 161 | 152 |

[a] Estimated from the deposition rate of copper from magnetron sputtering on a bare silicon wafer; [b] Estimated from topview and sideview SEM images.

Geometry parameters used in the simulation are summarized in Table 5.1. Top shell thickness of the nanocups is estimated from the deposition rate of copper on a bare silicon wafer while the PSL particle size and the side shell thickness of the nanocups are estimated from SEM images. We should note that the actual RIE is timed manually and therefore might deviate from the nominal 54 sec. As a result, the actual PSL particle size may fluctuate a little around the nominal value 146 nm (see the geometry model at the bottom of Fig. 5.10 and the last column in Table 5.1). Calculated extinction cross sections for each of the four nanocups are shown as the dashed curves in Fig. 5.10 in the same colors as the experimental spectra. Good agreements between experimental and calculated spectra were found, not only for the main plasmon resonance peaks between 1000 nm and 1500 nm, but also for the small features between 600 nm and 1000 nm. With decreasing deposition time and therefore decreasing shell thickness, the main plasmon resonance peak red-shifts from $\sim$1000 nm to 1500 nm. The red-shift of the main dipole-like plasmons is due to the increased impedance of the copper nanocups and the increased field confinement of the plasmons.

In addition to shell thickness, the LSPR peaks of the copper nanocups can also be tuned by varying the core PSL particle size. Copper nanocups are deposited on PSL templates of 3 different sizes, namely 127 nm, 214 nm and 237 nm, with 132 sec DC magnetron sputtering. Extinction spectra of the nanocups dispersed in a 1:1 mixture of toluene and acetic acid are shown in Fig. 5.11. The green curve (237 nm) and the red curve (214 nm) are scaled down to the black curve (127 nm) for easy comparison. With increasing core PSL particle size, the main plasmon resonance peak red-shifts from ∼ 900 nm to 1400 nm.

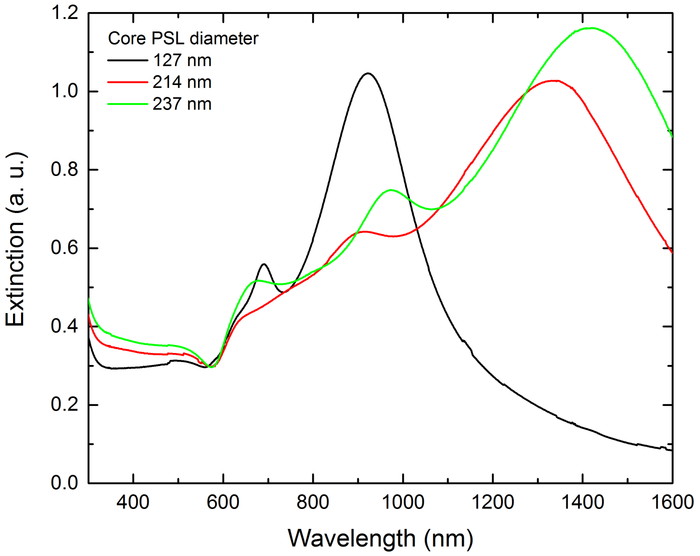

Figure 5.11: Measured extinction spectra for copper nanocups deposited on PSL templates of 3 different sizes, namely 127 nm, 214 nm and 237 nm. The copper deposition time is 132 sec in all three cases. Red and green curves are scaled down to the black curve for easy comparison.

### 5.2.4 Oxidation Study of Copper Nanocups

To study the oxidation and degradation of copper nanocups in air, extinction spectra are measured in toluene immediately, 3 days, 7 days and 13 days after fabrication, shown in Fig. 5.12. A new nanocup dispersion is prepared for every extinction spectrum measurement, using nanocups on an area of 3.7 cm by 3.7 cm. This helps to avoid multiple transfers of the nanocup dispersion between the measurement cuvette and the sonication vial that might be incomplete due to surface tension of the solvent. A new baseline from toluene is collected for each measurement to minimize the effects of cross-contamination from other materials stuck on the cuvette.

A minor red-shift and attenuation of the main LSPR peak at around 1200 nm is observed after 3 days. This allows plenty of time for the copper nanocups to be further processed in air for applications while their plasmonic properties remain almost the same. After 7 days, the red-shift and attenuation of the main LSPR peak becomes more noticeable. We note, however, the peak intensity of the main LSPR peak at around 1200 nm compared to the background extinction below 600 nm and above 1600 nm is still greater than $10^{1.25}$. After 13 days, the main LSPR peak remains roughly the same as that after 7 days although the small features between 600 nm and 1000 nm see a minor decrease in intensity. A possible explanation is that the multipolar components of the plasmon resonances between 600 nm and 1000 nm are sensitive to slight changes of shell thickness and rim sharpness due to oxidation.

It should be noted that, for some unknown mechanism, certain batches of copper nanocup samples tend to stick to the cuvette wall when measuring their extinction spectra about (or more than) 10 days after fabrication. When this happens, a nonuniform layer of transparent black film can be observed on the cuvette wall by naked eye, rendering the extinction measurements questionable. This suggests that the sticking behavior has something to do with oxidation but there must be some other factors too as the sticking behavior is not always observed. Nonetheless, the extinction spectra after 10 days for non-sticking samples (*i.e.* when no black films can be observed on the cuvette wall) are consistently similar to those after 7 days in terms of both LSPR peak positions and LSPR peak magnitudes, suggesting that oxidation has slowed down significantly after 7 days. It might be argued that the naked eye observation of no black film is not sufficient to claim a non-sticking sample, however the fact that the main LSPR peak position remains almost the same (for both sticking and non-sticking samples) between day 7 and day 13 still strongly indicates negligible oxidation during the period.

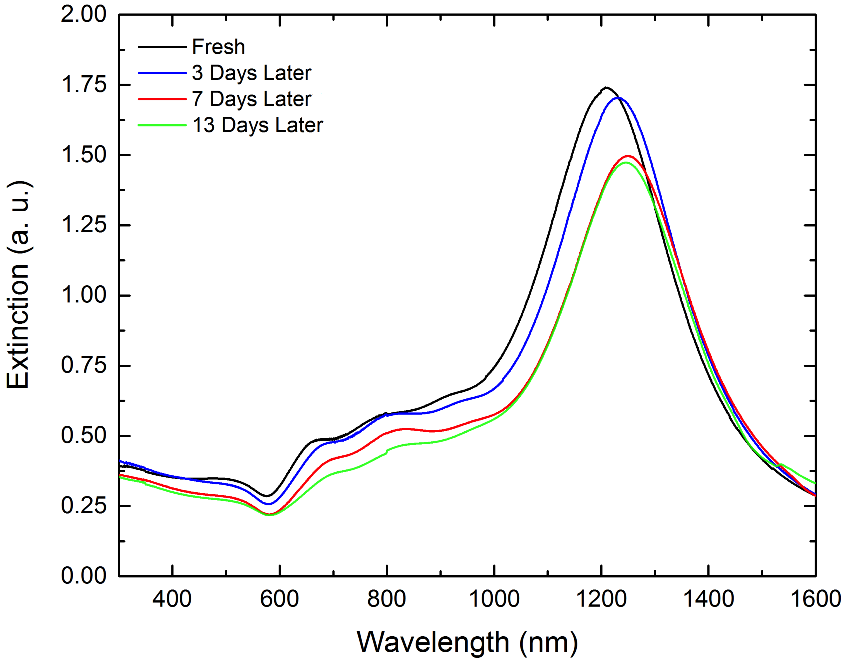

Figure 5.12: Extinction spectra of copper nanocups measured in toluene immediately, 3 days, 7 days and 13 days after fabrication.

### 5.2.5 Potential Application: an Alternative to Low Emissivity Window Coatings

Nanomaterials made of cheap plasmonic metals as studied here appear very interesting for optical applications such as meta-solutions and meta-films [129, 130]. A mixture of plasmonic nanocrystals of different sizes and shapes can be used to design interesting and potentially useful materials with tailored transmission spectra in the visible and IR spectral intervals. For example, meta-solutions and meta-films with a narrow transmission window placed in the IR spectral interval were designed using collections of plasmonic nanorods, nanocrosses and semiconductor quantum dots [129, 130]. We should note that, so far, mostly noble nanocrystals were considered for applications of this kind since mostly gold and silver nanocrystals exhibit narrow plasmon peaks. However, we show in this paper that copper and aluminum nanocrystals also show potential for applications of this sort. These nanomaterials show narrow and tunable plasmon resonances in wide spectral intervals and, importantly, are made of cheap metals. Furthermore, the template-assisted magnetron sputtering technique used in this study can be easily scaled up in industry and, therefore, the nanomaterials fabricated in this study can be potentially produced in large quantities.

Here we demonstrate one potential application for these copper nanocups: window coatings. Nowadays low emission windows are often an integral part of high performance commercial buildings. Multilayer structures comprised of metal, metal oxides and metal nitrides are deposited on window glasses via physical vapor deposition, e.g., magnetron sputtering. The number of layers in these multilayer coatings ranges from three to sometimes more than thirteen. Among those layers, one or more are often silver layers that help to reflect heat from the sun. Typical transmission spectra for low emission window coatings are shown in Fig. 5.13 (a) (redrawn from data in Ref. 181).

Based on numerical superposition of the measured extinction data, we found that transmission spectra somewhere in between those of moderate solar gain and low solar gain low emission coatings can be achieved with a mixture of copper nanocups at a low overall concentration. Specifically, a mixture of 90 sec, 60 sec and 40 sec copper nanocups with a ratio of 0.1:0.1:1.3 yields the theoretical transmission spectrum shown as the solid green curve in Fig. 5.13 (b). The numbers 0.1, 0.1 and 1.3 are relative concentrations of corresponding copper nanocups in reference to the amount used in the extinction spectra measurement shown in Fig. 5.10 (nanocups on an area of about 3.7 cm by 3.7 cm dispersed in about 3 mL). In other words, the measured extinction spectra for each copper nanocup component is taken from Fig. 5.10 and then multiplied by the numbers 0.1, 0.1 and 1.3 and converted to transmission. The overall transmission for the nanocup mixture is then obtained by multiplying the transmission for each nanocup component together. Alternatively, we can also calculate the transmission spectrum of the mixture using calculated cross sections, shown as the dashed blue curve in Fig. 5.13 (b). For this calculation the transmittance of the nanocup mixture is written as

$$T = \exp\left( - \sum \sigma_{ext,i}\, n_i\, L \right) \tag{5.1}$$

Here $\sigma_{ext,i}$ and $n_i$ are extinction cross section and the number density of the $i$th species respectively, and $L$ is the path length of the beam. For the nanocups with deposition time of 90 sec, 60 sec and 40 sec, the quantities $n_i L$ are estimated as $2.6 \times 10^8\,\mathrm{cm}^{-2}$, $2.6 \times 10^8\,\mathrm{cm}^{-2}$, and $3.4 \times 10^9\,\mathrm{cm}^{-2}$, respectively. As seen, the transmission spectrum calculated based on the cross sections has consistent spectral features with the one calculated based on measured extinction spectra. Transmittance of the copper nanocup mixture from 800 nm to 1600 nm lies between those of moderate solar gain and low solar gain low emission coatings while the transmittance below 700 nm lies slightly (15%) below those of low emission coatings. Therefore, the replacement of multilayer coatings containing silver layers with copper nanocups may significantly reduce costs without sacrificing high window performance.

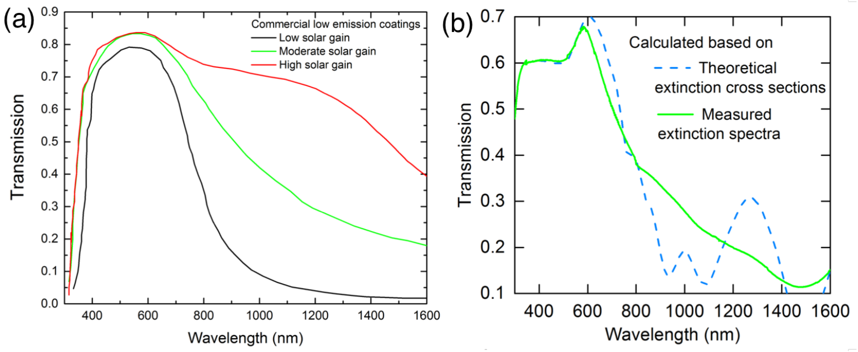

Figure 5.13: (a) Transmission spectra of commercial low emission coatings with low, moderate and high solar gain. Redrawn from data in Ref. 181. (b) Theoretical transmission spectra from a mixture of 90 sec, 60 sec, and 40 sec copper nanocups with a low overall concentration, calculated based on measured extinction spectra (solid green curve) and theoretical extinction cross sections (dashed blue curve) for each copper nanocup component.

## 5.3 Conclusion

In this chapter we experimentally and theoretically investigated the plasmonic properties of aluminum and copper nanocups, fabricated by magnetron sputtering on templated wafers. The choice of magnetron sputtering, rather than other PVD techniques, is based on the high film qualities commonly seen in sputtered thin films. The fabrication of nanocups is essentially the deposition of a thin metal film on a dielectric core.

We focused on the copper nanocups as they demonstrate much stronger and sharper plasmon resonance peaks compared to their aluminum counterparts. The nanocups are fabricated by magnetron sputtering of corresponding targets in an argon environment onto silicon wafers templated with non-close-packed PSL particles. The non-close-packed feature of the PSL particles guarantees that the nanocups subsequently fabricated on them are discrete and well-defined.

Extinction spectra of the nanocups are measured with the nanocups dispersed in toluene or a 1:1 mixture of toluene and acetic acid. For the aluminum nanocups, two plasmon resonance peaks around 580 nm and 990 nm are observed although both of them have relatively low peak intensities. For the copper nanocups, three or more plasmon resonance peaks are observed with the main plasmon resonance peak having a peak intensity more than 10 times stronger than the background extinction. Tunability of the main copper plasmon resonance peak from 900 nm to 1500 nm is achieved by varying shell thickness or core PSL particle size, extending the typical plasmon range of copper plasmonics. Good agreements between calculated and experimental extinction spectra are found in all cases. The nature of the plasmon resonance peaks is revealed from charge maps and electromagnetic field intensity maps calculated by our collaborators. Oxidation study is also carried out for the copper nanocups by measuring the extinction spectra in toluene immediately, 3 days, 7 days and 13 days after fabrication. The main plasmon resonance peak sees a minor red-shift and attenuation after 3 days and stabilizes after 13 days. A potential application for the copper nanocups is low emissivity window coatings. The replacement of commercial low emissivity window coatings containing one or multiple silver layers with copper nanocup mixtures may significantly reduce costs without sacrificing high performance.

# Chapter 6

# Fabrication of Anisotropic Plasmonic Nanostructures: Copper Nanorods

In this chapter we will focus on the fabrication and characterization of copper nanorods. Copper is chosen as the prototype material for this fabrication process as there are no stoichiometry issues and therefore emphasis can be placed on optimizing the fabrication method itself.

## 6.1 Experimental Setup

A schematic of the fabrication process is shown in Fig. 6.1, which is largely similar to that for the nanocups, except that the final deposition is done at a glancing angle, *i.e.* glancing angle deposition (GLAD).

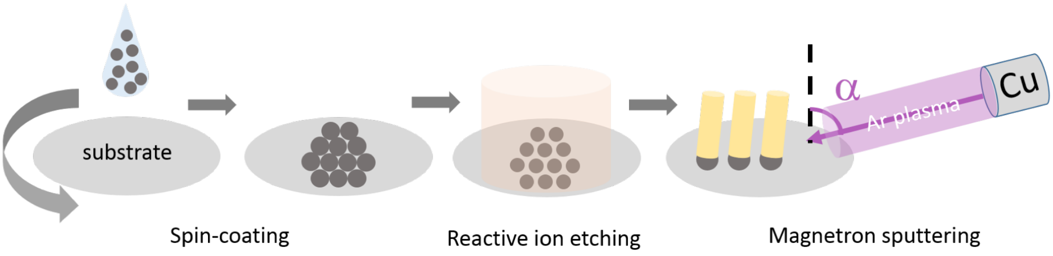

Figure 6.1: Schematic of the fabrication process for nanorods. The fabrication process is largely similar to that for the nanocups, except that the last deposition process is done at a glancing angle.

### 6.1.1 Glancing Angle Deposition

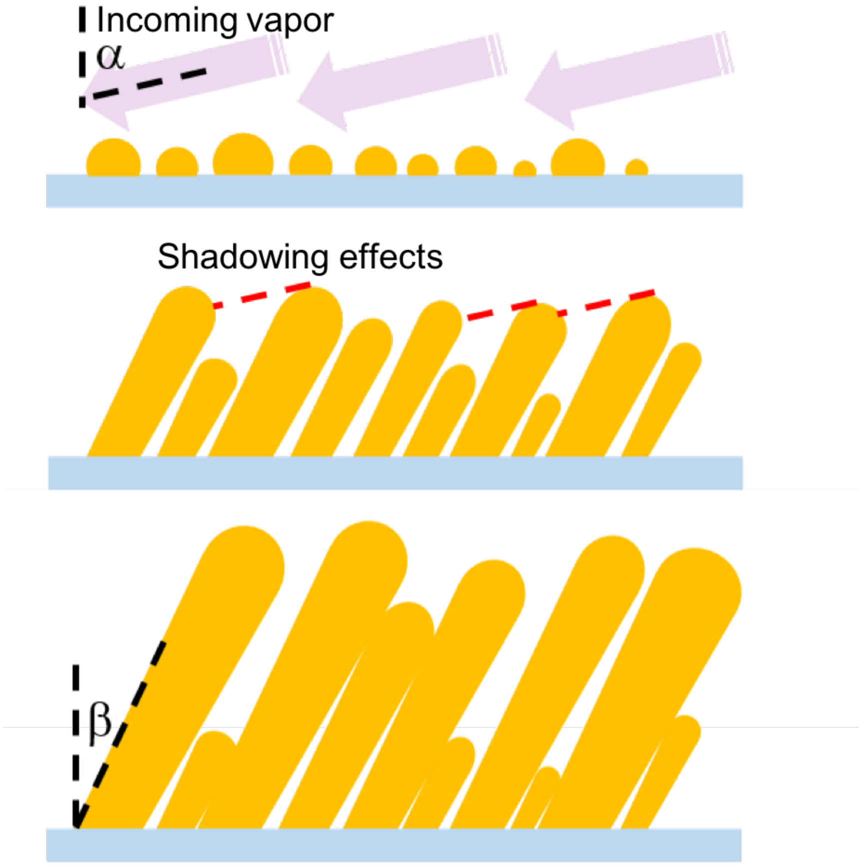

Figure 6.2: Schematic of the GLAD mechanism. After the initial nucleation process, the effect of ballistic shadowing, shown by dashed red lines, favors the growth of some nucleation sites while suppressing others, and eventually leads to the formation of nanorods. The growth angle $\beta$ is different from the incident vapor angle $\alpha$. Redrawn from Ref. 182

A schematic of the GLAD mechanism is shown in Fig. 6.2. As the name suggests, for GLAD the substrate is tilted such that the incident flux arrives at a very large angle, usually greater than 70°, with respect to the substrate normal. After the initial random nucleation process, the effect of ballistic shadowing favors the growth of some nucleation sites while suppressing others, and eventually leads to the formation of nanorods. We should note that, these columns grow at an angle $\beta$ different from the incident flux angle $\alpha$. In fact, the difference in $\alpha$ and $\beta$, or more specifically, $\beta$ being smaller than $\alpha$, ensures the effect of ballistic shadowing during the deposition process. A detailed description of this deposition method can be found in Ref. 182.

Some drawbacks of the traditional GLAD method are that, first of all, the initial nucleation process is entirely random and results in a large size distribution in the nanorods subsequently grown out of them, and secondly, adjacent nanorods suffer from interconnection problems. For plasmonic applications, however, size and shape uniformity are highly desired to in turn achieve sharp LSPR resonance peaks. As we will show in the following sections, templating the silicon wafers with colloidal templates, e.g. a regular array of PSL particles, is both necessary and effective for the fabrication of discrete nanorods.

Figs. 6.3 (a) and (b) show two typical sideview SEM images for GLAD with and without a PSL template. Although columnar structure can be observed in both films, the non-templated film clearly exhibits a large size distribution in the columnar grains while the templated film shows highly monodispersed nanorods. However, both films suffer from interconnection issues and cannot be separated into discrete grains/nanorods upon sonication and do not exhibit any obvious plasmonic properties in their extinction spectra.

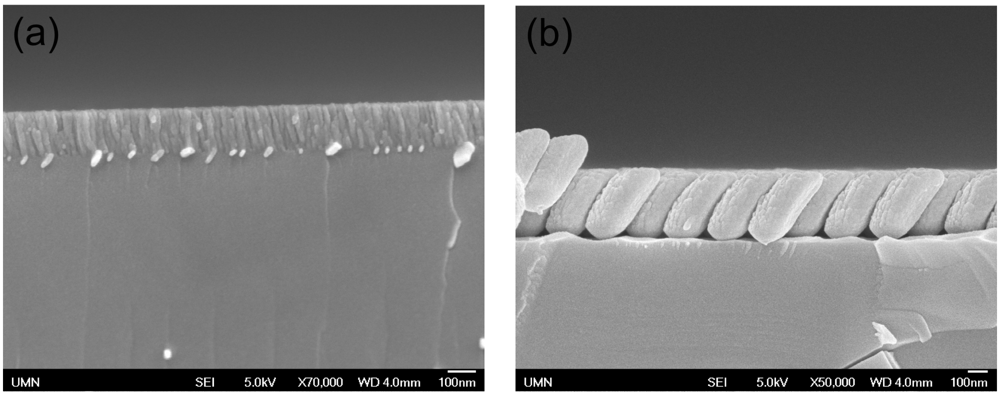

Figure 6.3: Typical sideview SEM images of copper nanorods (columns) grown using GLAD without (a) and with (b) PSL templates.

## 6.2 Results and Discussion

To avoid the nanorod interconnection problem we again resort to RIE of the PSL particles. Compared to the case of nanocup fabrication, controlling the RIE etching time requires extra care for the fabrication of nanorods: the inter-particle distance needs to be large enough such that the subsequently grown nanorods do not interconnect with their neighbors, but at the same time the inter-particle distance cannot be so large that the space between particles is able to receive a significant portion of incoming flux and unwanted extra structures grow, shown in Fig. 6.4. The extra structures are attached to the nanorods and cannot be detached through sonication.

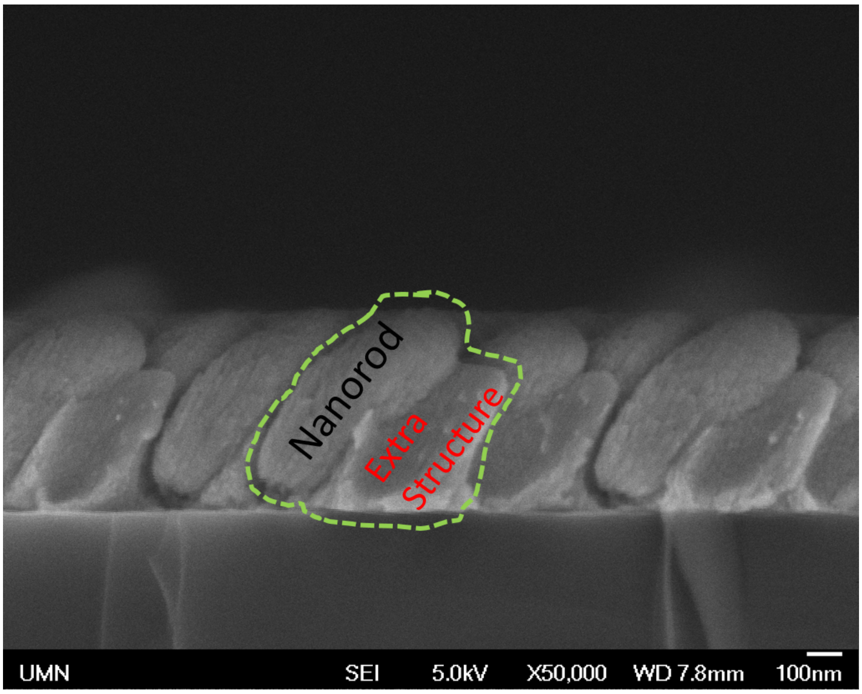

Figure 6.4: Sideview SEM image for copper nanorods grown on a template that has too much spacing. The extra structure is circled together with the nanorod. Sonication does not detach the extra structure from the nanorod.

With carefully optimized RIE time, discrete copper nanorods are successfully fabricated by GLAD. Figs. 6.5 show the topview and sideview SEM images of 5 min, 7 min and 13 min copper GLAD deposition on etched PSL templates. All these samples dispersed easily when sonicated in a 1:1 mixture of toluene and acetic acid. Toluene dissolves the PSL particles and therefore releases the copper nanorods into the solution for extinction spectra measurements while acetic acid removes the surface oxides. It should be noted that nanorod lengths in sideview SEM images should only be taken qualitatively due to the fact that the GLAD grown nanorods are tilted in the three-dimensional space while sideview SEM images are only two-dimensional projections.

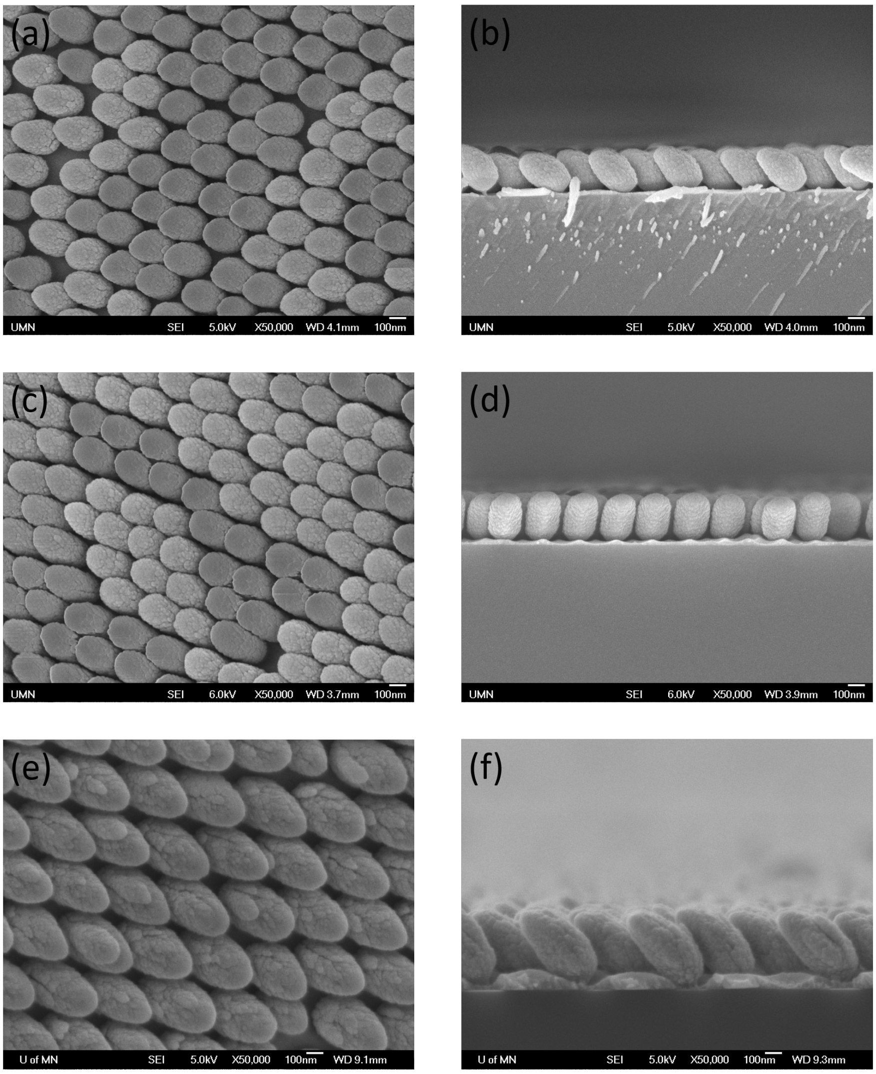

Figure 6.5: Topview and sideview SEM images of 5 min (a, b), 7 min (c, d) and 13 min (e, f) copper GLAD deposition on etched colloidal templates. It should be noted that nanorod lengths in sideview SEM images should only be used as qualitative indications for the actual nanorod lengths due to the fact that the nanorods are tilted in the three-dimensional space and the SEM images are only two-dimensional projections.

Fig. 6.6 shows the extinction spectra of these nanorods dispersed in the mixture of toluene and acetic acid. Two sets of LSPR peaks can be observed. The peaks near 650 nm are attributed to the transverse plasmon mode while the peaks at longer wavelengths are attributed to the longitudinal plasmon modes. The longitudinal LSPR peak red-shifts with increasing deposition time, in other words increasing nanorod length, as expected. The extinction shoulder below 600 nm is due to the interband transition between 3d band the conduction band of copper. Attempts were made for deposition times longer than 13 min, to separate the longitudinal and transverse LSPR more, but failed due to interconnection issues.

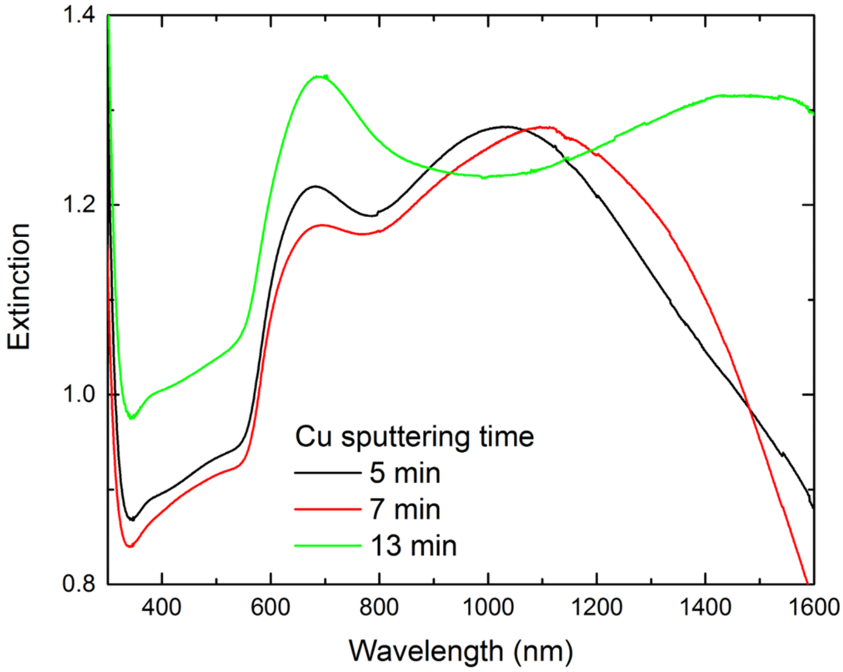

Figure 6.6: Extinction spectra of 5 min, 7 min and 13 min GLAD copper nanorods measured in a 1:1 mixture of toluene and acetic acid.

Oxidation behavior of the nanorods was studied by measuring the 13 min sample one day after fabrication in both toluene and mixture of toluene and acetic acid, shown in Fig. 6.7. Contrary to the case of copper nanocups, copper nanorods suffer from severe oxidation problems and their plasmonic properties degrade significantly after only one day of oxidation (black curve). Dispersing the nanorods in a mixture of toluene and acetic acid recovers the plasmonic properties, although a decrease in the longitudinal LSPR magnitude is observed (green curve). A possible explanation for the drastically different oxidation behavior is that whether the oxidation of copper is self-limiting or non-self-limiting depends directly on the strain conditions of the oxide shell [183]. Oxidation of the copper nanocups can be significantly more self-limiting due to the existence of large curvatures and sharp edges in the nanocup geometry.

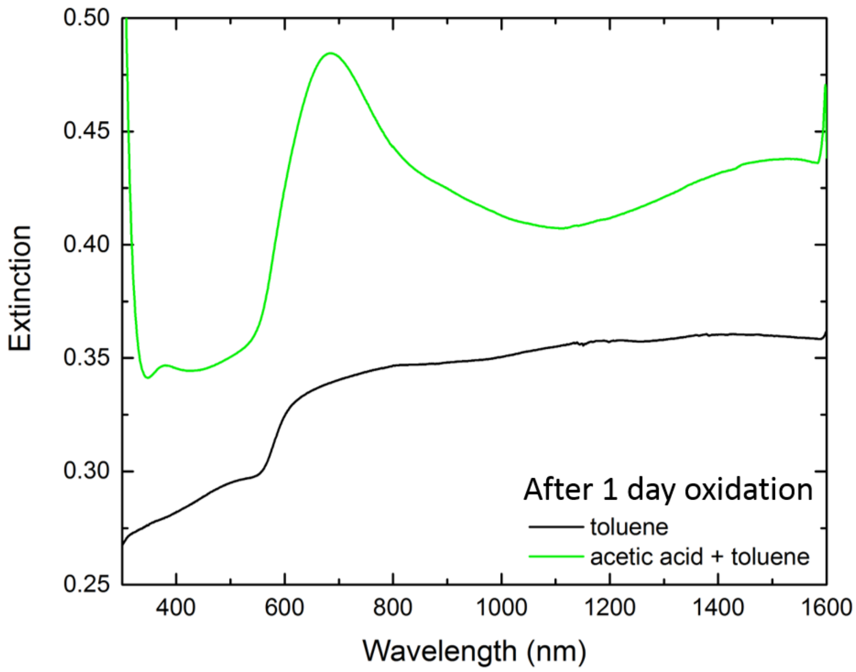

Figure 6.7: Extinction spectra of the 13 min copper nanorods measured in toluene and mixture of toluene and acetic acid, showing the significant impact of oxidation on these nanorods.

It should be noted that the NFC sputtering system used for the fabrication of copper nanorods (AJA1) is not designed for GLAD purposes. Therefore improvised substrate holders have to be used to implement the glancing angle. The absolute values of the glancing angle can only be assessed by the naked eye and some variations in the glancing angles inevitably exist for the samples above. Variations in the deposition angle in turn result in variations of the nanorod growing direction, shadowing effects and nanorod morphology. This is one of the two main reasons that prompted us to construct a custom-built angle sputtering system, described in detail in the appendix. The other reason is to implement heating for GLAD deposition.

## 6.3 Conclusion

In this chapter we described the fabrication method for copper nanorods, which is essentially the same as the fabrication method for nanocups, except that the deposition is done at a glancing angle. The copper nanorods exhibit two plasmon resonance peaks as expected, corresponding to electron oscillations in the transverse and longitudinal directions, respectively. Tunability of the longitudinal plasmon resonance peak is achieved by varying the magnetron sputtering deposition time. Compared with copper nanocups, copper nanorods suffer from much more severe oxidation problems and this may be attributed to the fact that copper oxidation becomes more self-limited when there is strain present in the oxide layer. Copper nanocups are likely to have more strain in the oxide layer due to the large curvatures and sharp tips in the nanocup geometry.

# Chapter 7

# Conclusion

In the first part of this dissertation thesis we focused on particle dynamics visualized by laser light scattering in a silane-containing dusty plasma. A better understanding of particle dynamics in dusty plasmas can be beneficial to both the intended synthesis of nanoparticles and the mitigation of nanoparticle contamination issues. Three distinct types of spatiotemporal behavior are observed for the dust particles, depending on the specific plasma power and pressure. The changing balance between the ion drag force and the electrostatic forces is hypothesized to be the dominant mechanism that determines particle dynamics in our case. The combination of laser light scattering and plasma emission proves to be an effective method for observing dust particles between tens of nanometers to a few hundreds of nanometers.

The second part of the dissertation thesis focused on the application of a magnetically enhanced glow discharge, namely magnetron sputtering, as a critical deposition technique for the fabrication of anisotropic plasmonic nanostructures. Upon light irradiation at the resonance frequency, plasmonic nanostructures can exhibit interesting near-field enhancement and far-field extinction, arising from the resonant oscillation of conduction electrons in the nanostructures. Specifically, we fabricated plasmonic nanocups and nanorods with alternative materials such as copper, aluminum and titanium nitride. The nanocups exhibit plasmon resonances in the near-infrared (especially sharp in the copper case), an important optical range for biological and window coating applications. The copper nanorods exhibit two plasmon resonances as expected, corresponding to electron oscillations in the transverse and longitudinal directions, respectively. Two sputtering systems at the University of Minnesota Nano Fabrication Center (NFC) are used in this thesis. Due to certain limitations of the NFC systems during preliminary attempts at titanium nitride fabrication, we also constructed a custom-built angle sputtering system with a tiltable heated stage, introduced in detail in the appendix.

# References

[1] MA Lieberman and AJ Lichtenberg. *Principles of plasma discharges and materials processing.* John Wiley & Sons, 2005.

[2] Y Qin, N Bilik, UR Kortshagen, and ES Aydil. Laser light scattering from silicon particles generated in an argon diluted silane plasma. *Journal of Physics D: Applied Physics*, 49(8):085203, 2016.

[3] PK Shukla and AA Mamun. *Introduction to Dusty Plasma Physics.* CRC Press, 2001.

[4] CK Goertz. Dusty plasmas in the solar system. *Reviews of Geophysics*, 27(2):271–292, 1989.

[5] VE Fortov and GE Morfill. *Complex and dusty plasmas: from laboratory to space.* CRC Press, 2009.

[6] L Mangolini, E Thimsen, and UR Kortshagen. High-yield plasma synthesis of luminescent silicon nanocrystals. *Nano Lett.*, 5(4):655–659, 2005.

[7] KK Ostrikov, U Cvelbar, and AB Murphy. Plasma nanoscience: setting directions, tackling grand challenges. *J. Phys. D: Appl. Phys.*, 44(17):174001, 2011.

[8] A Gupta, MT Swihart, and H Wiggers. Luminescent colloidal dispersion of silicon quantum dots from microwave plasma synthesis: exploring the photoluminescence behavior across the visible spectrum. *Adv. Funct. Mater.*, 19(5):696–703, 2009.

[9] UR Kortshagen. Nonthermal plasma synthesis of semiconductor nanocrystals. *J. Phys. D: Appl. Phys.*, 42(11):113001, 2009.

[10] KY Cheng, R Anthony, UR Kortshagen, and RJ Holmes. High-efficiency silicon nanocrystal light-emitting devices. *Nano Lett.*, 11(5):1952–1956, 2011.

[11] E Thimsen, M Johnson, X Zhang, AJ Wagner, KA Mkhoyan, UR Kortshagen, and ES Aydil. High electron mobility in thin films formed via supersonic impact deposition of nanocrystals synthesized in nonthermal plasmas. *Nat. Commun.*, 5:5822, 2014.

[12] M Mikikian and L Boufendi. Experimental investigations of void dynamics in a dusty discharge. *Phys. Plasmas*, 11(8):3733–3737, 2004.

[13] J Goree, GE Morfill, VN Tsytovich, and SV Vladimirov. Theory of dust voids in plasmas. *Phys. Rev. E*, 59(6):7055, 1999.

[14] H Thomas, GE Morfill, V Demmel, J Goree, B Feuerbacher, and D Möhlmann. Plasma crystal: Coulomb crystallization in a dusty plasma. *Physical Review Letters*, 73(5):652, 1994.

[15] Y Hayashi and K Tachibana. Observation of coulomb-crystal formation from carbon particles grown in a methane plasma. *Japanese journal of applied physics*, 33(6A):L804, 1994.

[16] H Tawidian, T Lecas, and M Mikikian. Zoom into dusty plasma instabilities. *IEEE Trans. Plasma Sci.*, 41(4):754–758, 2013.

[17] M Mikikian, L Couëdel, Y Tessier, and L Boufendi. Carousel instability in a capacitively coupled rf dusty plasma. *IEEE transactions on plasma science*, 39(11):2748–2749, 2011.

[18] R Hoogerbrugge and PG Kistemaker. Analytical expressions for the internal and kinetic energy distributions of sputtered clusters and molecules. *Nuclear Instruments and Methods in Physics Research Section B: Beam Interactions with Materials and Atoms*, 21(1-4):37–45, 1987.

[19] G Praburam and J Goree. Experimental observation of very low-frequency macroscopic modes in a dusty plasma. *Physics of Plasmas*, 3(4):1212–1219, 1996.

[20] T Fukuzawa, H Kawasaki, M Shiratani, and Y Watanabe. Study on growth processes of subnanometer particles in early phase of silane rf discharge. *Japanese journal of applied physics*, 33(7S):4212, 1994.

[21] H Kawasaki, H Ohkura, T Fukuzawa, M Shiratani, Y Watanabe, Y Yamamoto, S Suganuma, M Hori, and T Goto. Roles of sih3 and sih2 radicals in particle growth in rf silane plasmas. *Japanese journal of applied physics*, 36(7S):4985, 1997.

[22] Y Watanabe, M Shiratani, H Kawasaki, S Singh, T Fukuzawa, Y Ueda, and H Ohkura. Growth processes of particles in high frequency silane plasmas. *Journal of Vacuum Science & Technology A: Vacuum, Surfaces, and Films*, 14(2):540–545, 1996.

[23] Y Watanabe, M Shiratani, T Fukuzawa, H Kawasaki, Y Ueda, S Singh, and H Ohkura. Contribution of short lifetime radicals to the growth of particles in sih4 high frequency discharges and the effects of particles on deposited films. *Journal of Vacuum Science & Technology A: Vacuum, Surfaces, and Films*, 14(3):995–1001, 1996.

[24] L Boufendi and A Bouchoule. Particle nucleation and growth in a low-pressure argon-silane discharge. *Plasma Sources Sci. Technol.*, 3(3):262, 1994.

[25] C Hollenstein, JL Dorier, J Dutta, L Sansonnens, and AA Howling. Diagnostics of particle genesis and growth in rf silane plasmas by ion mass spectrometry and light scattering. *Plasma Sources Sci. Technol.*, 3(3):278, 1994.

[26] AA Howling, L Sansonnens, JL Dorier, and Ch Hollenstein. Time-resolved measurements of highly polymerized negative ions in radio frequency silane plasma deposition experiments. *J. Appl. Phys.*, 75(3):1340–1353, 1994.

[27] AA Howling, L Sansonnens, JL Dorier, and Ch Hollenstein. Negative hydrogenated silicon ion clusters as particle precursors in rf silane plasma deposition experiments. *J. Phys. D: Appl. Phys.*, 26(6):1003, 1993.

[28] AA Howling, JL Dorier, and Ch Hollenstein. Negative ion mass spectra and particulate formation in radio frequency silane plasma deposition experiments. *Appl. Phys. Lett.*, 62(12):1341–1343, 1993.

[29] A Bouchoule, A Plain, L Boufendi, JP Blondeau, and C Laure. Particle generation and behavior in a silane-argon low-pressure discharge under continuous or pulsed radio-frequency excitation. *J. Appl. Phys*, 70(4):1991–2000, 1991.

[30] AA Fridman, L Boufendi, T Hbid, BV Potapkin, and A Bouchoule. Dusty plasma formation: Physics and critical phenomena. theoretical approach. *J. Appl. Phys.*, 79(3):1303–1314, 1996.

[31] L Landau and E Teller. Zur theorie der schalldispersion. *Phys. Z. Sowjetunion*, 10(1):34, 1936.

[32] HA Bethe and E Teller. Aberdeen proving ground report x-117. *Google Scholar*.

[33] RN Schwartz, ZI Slawsky, and KF Herzfeld. Calculation of vibrational relaxation times in gases. *The Journal of Chemical Physics*, 20(10):1591–1599, 1952.

[34] U Bhandarkar, UR Kortshagen, and S Girshick. Numerical study of the effect of gas temperature on the time for onset of particle nucleation in argon–silane low-pressure plasmas. *Journal of Physics D: Applied Physics*, 36(12):1399, 2003.

[35] NJ Kramer, RJ Anthony, M Mamunuru, ES Aydil, and UR Kortshagen. Plasma-induced crystallization of silicon nanoparticles. *Journal of Physics D: Applied Physics*, 47(7):075202, 2014.

[36] M Mamunuru, R Le Picard, Y Sakiyama, and SL Girshick. The existence of non-negatively charged dust particles in nonthermal plasmas. *Plasma Chemistry and Plasma Processing*, 37(3):701–715, 2017.

[37] UR Kortshagen, UV Bhandarkar, MT Swihart, and SL Girshick. Generation and growth of nanoparticles in low-pressure plasmas. *Pure and applied chemistry*, 71(10):1871–1877, 1999.

[38] UV Bhandarkar, MT Swihart, SL Girshick, and UR Kortshagen. Modelling of silicon hydride clustering in a low-pressure silane plasma. *Journal of Physics D: Applied Physics*, 33(21):2731, 2000.

[39] K De Bleecker, A Bogaerts, R Gijbels, and W Goedheer. Numerical investigation of particle formation mechanisms in silane discharges. *Physical Review E*, 69(5):056409, 2004.

[40] Y Watanabe. Formation and behaviour of nano/micro-particles in low pressure plasmas. *Journal of Physics D: Applied Physics*, 39(19):R329, 2006.

[41] M Cavarroc, M Mikikian, Y Tessier, and L Boufendi. Instabilities during the growth of dust successive generations in silane-based plasmas. *Phys. Plasmas*, 15(10):103704, 2008.

[42] M Cavarroc, M Mikikian, Y Tessier, and L Boufendi. Successive generations of dust in complex plasmas: A cyclic phenomenon in the void region. *Phys. Rev. Lett.*, 100(4):045001, 2008.

[43] M Cavarroc, M Mikikian, G Perrier, and L Boufendi. Single-crystal silicon nanoparticles: An instability to check their synthesis. *Appl. Phys. Lett.*, 89(1):013107, 2006.

[44] M Cavarroc, MC Jouanny, K Radouane, M Mikikian, and L Boufendi. Self-excited instability occurring during the nanoparticle formation in an ar–sih4 low pressure radio frequency plasma. *J. Appl. Phys.*, 99(6):064301, 2006.

[45] M Mikikian, L Couëdel, M Cavarroc, Y Tessier, and L Boufendi. Self-excited void instability in dusty plasmas: plasma and dust cloud dynamics during the heartbeat instability. *New J. Phys.*, 9(8):268, 2007.

[46] J Goree. Ion trapping by a charged dust grain in a plasma. *Physical review letters*, 69(2):277, 1992.

[47] AV Zobnin, AP Nefedov, VA SinelâĂŹShchikov, and VE Fortov. On the charge of dust particles in a low-pressure gas discharge plasma. *Journal of Experimental and Theoretical Physics*, 91(3):483–487, 2000.

[48] M Lampe, V Gavrishchaka, G Ganguli, and G Joyce. Effect of trapped ions on shielding of a charged spherical object in a plasma. *Physical review letters*, 86(23):5278, 2001.

[49] S Ratynskaia, S Khrapak, A Zobnin, MH Thoma, M Kretschmer, A Usachev, V Yaroshenko, RA Quinn, GE Morfill, O Petrov, et al. Experimental determination of dust-particle charge in a discharge plasma at elevated pressures. *Physical review letters*, 93(8):085001, 2004.

[50] SA Khrapak, SV Ratynskaia, AV Zobnin, AD Usachev, VV Yaroshenko, MH Thoma, M Kretschmer, H Höfner, GE Morfill, and OF Petrov. Particle charge in the bulk of gas discharges. *Physical Review E*, 72(1):016406, 2005.

[51] M Gatti and UR Kortshagen. Analytical model of particle charging in plasmas over a wide range of collisionality. *Physical Review E*, 78(4):046402, 2008.

[52] U Kortshagen and U Bhandarkar. Modeling of particulate coagulation in low pressure plasmas. *Physical Review E*, 60(1):887, 1999.

[53] EC Whipple. Potentials of surfaces in space. *Reports on Progress in Physics*, 44(11):1197, 1981.

[54] P Debye and E Hückel. On the theory of electrolytes. i. freezing point depression and related phenomena. *The collected papers of Peter JW Debye*, pages 217–263, 1954.

[55] H Yukawa. On the interaction of elementary particles. i. *Proceedings of the Physico-Mathematical Society of Japan. 3rd Series*, 17:48–57, 1935.

[56] M Lampe. Limits of validity for orbital-motion-limited theory for a small floating collector. *Journal of plasma physics*, 65(3):171–180, 2001.

[57] H. M. Mott-Smith and I Langmuir. The theory of collectors in gaseous discharges. *Phys. Rev.*, 28:727–763, Oct 1926.

[58] IB Bernstein and IN Rabinowitz. Theory of electrostatic probes in a low-density plasma. *The Physics of Fluids*, 2(2):112–121, 1959.

[59] JG Laframboise and LW Parker. Probe design for orbit-limited current collection. *The Physics of Fluids*, 16(5):629–636, 1973.

[60] JE Daugherty, RK Porteous, MD Kilgore, and DB Graves. Sheath structure around particles in low-pressure discharges. *Journal of applied physics*, 72(9):3934–3942, 1992.

[61] RN Varney. Mean free paths, ion drift velocities, and the poisson distribution. *American Journal of Physics*, 39:534–538, 1971.

[62] S.H. Lam. Mae 558 plasmadynamics notes. *Princeton University Department of Mechanical and aerospace engineering*, 1997.

[63] D Bohm. The characteristics of electrical discharges in magnetic fields. *Qualitative Description of the Arc Plasma in a Magnetic Field*, 1949.

[64] JE Daugherty, RK Porteous, and DB Graves. Electrostatic forces on small particles in low-pressure discharges. *Journal of applied physics*, 73(4):1617–1620, 1993.

[65] S Hamaguchi and RT Farouki. Polarization force on a charged particulate in a nonuniform plasma. *Physical Review E*, 49(5):4430, 1994.

[66] TG Northrop and TJ Birmingham. Plasma drag on a dust grain due to coulomb collisions. *Planetary and space science*, 38(3):319–326, 1990.

[67] MS Barnes, JH Keller, JC Forster, JA OâĂŹNeill, and DK Coultas. Transport of dust particles in glow-discharge plasmas. *Phys. Rev. Lett.*, 68(3):313, 1992.

[68] DB Graves, JE Daugherty, MD Kilgore, and RK Porteous. Charging, transport and heating of particles in radiofrequency and electron cyclotron resonance plasmas. *Plasma Sources Science and Technology*, 3(3):433, 1994.

[69] L Talbot, RK Cheng, RW Schefer, and DR Willis. Thermophoresis of particles in a heated boundary layer. *Journal of fluid mechanics*, 101(4):737–758, 1980.

[70] N Bilik, R Anthony, BA Merritt, ES Aydil, and UR Kortshagen. Langmuir probe measurements of electron energy probability functions in dusty plasmas. *J. Phys. D: Appl. Phys.*, 48(10):105204, 2015.

[71] D Samsonov and J Goree. Instabilities in a dusty plasma with ion drag and ionization. *Phys. Rev. E*, 59(1):1047–1058, 1999.

[72] J Goree and D Samsonov. Instabilities driven by ion drag. In *AIP Conference Proceedings*, volume 446, pages 157–167. AIP, 1998.

[73] MR Akdim and WJ Goedheer. Modeling the effect of dust on the plasma parameters in a dusty argon discharge under microgravity. *Physical Review E*, 67(6):066407, 2003.

[74] BM Annaratone, SA Khrapak, P Bryant, GE Morfill, H Rothermel, HM Thomas, M Zuzic, VE Fortov, VI Molotkov, and AP Nefedov. Complex-plasma boundaries. *Physical Review E*, 66(5):056411, 2002.

[75] M Mikikian, L Boufendi, A Bouchoule, HM Thomas, GE Morfill, AP Nefedov, and VE Fortov. Formation and behaviour of dust particle clouds in a radio-frequency discharge: results in the laboratory and under microgravity conditions. *New J. Phys.*, 5(1):19, 2003.

[76] HT Do, G Thieme, M Frohlich, H Kersten, and R Hippler. Ion molecule and dust particle formation in ar/ch4, ar/c2h2 and ar/c3h6 radio-frequency plasmas. *Contributions to Plasma Physics*, 45(5-6):378–384, 2005.

[77] JL Dorier, Ch Hollenstein, and AA Howling. Spatiotemporal powder formation and trapping in radio frequency silane plasmas using two-dimensional polarization-sensitive laser scattering. *J. Vac. Sci. Technol. A*, 13(3):918–926, 1995.

[78] L Couëdel, M Mikikian, AA Samarian, and L Boufendi. Self-excited void instability during dust particle growth in a dusty plasma. *Phys. Plasmas*, 17(8):083705, 2010.

[79] P Agarwal and SL Girshick. Numerical modeling of an rf argon–silane plasma with dust particle nucleation and growth. *Plasma Chem. Plasma P.*, 34(3):489–503, 2014.

[80] CF Bohren and DR Huffman. *Absorption and Scattering of Light by Small Particles*. John Wiley & Sons, 2008.

[81] DP Lymberopoulos and DJ Economou. Fluid simulations of radio frequency glow discharges: Two-dimensional argon discharge including metastables. *Appl. Phys. Lett.*, 63(18):2478–2480, 1993.

[82] DP Lymberopoulos and DJ Economou. Modeling and simulation of glow discharge plasma reactors. *Journal of Vacuum Science & Technology A: Vacuum, Surfaces, and Films*, 12(4):1229–1236, 1994.

[83] DP Lymberopoulos and DJ Economou. Two-dimensional self-consistent radio frequency plasma simulations relevant to the gaseous electronics conference rf reference cell. *Journal of research of the National Institute of Standards and Technology*, 100(4):473, 1995.

[84] JP Boeuf and LC Pitchford. Two-dimensional model of a capacitively coupled rf discharge and comparisons with experiments in the gaseous electronics conference reference reactor. *Physical Review E*, 51(2):1376, 1995.

[85] JL Dorier, Ch Hollenstein, AA Howling, C Courteille, W Schwarzenbach, A Merad, and JP Boeuf. Global visualization of powder trapping in capacitive rf plasmas by two-dimensional laser scattering. *IEEE Trans. Plasma Sci.*, 24(1):101–102, 1996.

[86] LJ Overzet and MB Hopkins. Spatial variations in the charge density of argon discharges in the gaseous electronics conference reference reactor. *Applied physics letters*, 63(18):2484–2486, 1993.

[87] D Herrebout, A Bogaerts, M Yan, R Gijbels, W Goedheer, and A Vanhulsel. Modeling of a capacitively coupled radio-frequency methane plasma: Comparison between a one-dimensional and a two-dimensional fluid model. *Journal of applied physics*, 92(5):2290–2295, 2002.

[88] SJ Choi, P Ventzek, RJ Hoekstra, and MJ Kushner. Spatial distributions of dust particles in plasmas generated by capacitively coupled radiofrequency discharges. *Plasma Sources Science and Technology*, 3(3):418, 1994.

[89] Y Qin, X Kong, Z Wang, AO Govorov, and UR Kortshagen. Near-infrared plasmonic copper nanocups fabricated by template-assisted magnetron sputtering. *ACS Photonics*, 4(11):2881–2890, 2017.

[90] T Ryynanen, M Toivanen, S Narkilahti, and J Lekkala. Titanium nitride microelectrodes deposited by ion beam assisted e-beam evaporation.

[91] N Angert. Ion sources.

[92] H Hahn and RS Averback. The production of nanocrystalline powders by magnetron sputtering. *Journal of Applied Physics*, 67(2):1113–1115, 1990.

[93] H Haberland, M Karrais, M Mall, and Y Thurner. Thin films from energetic cluster impact: A feasibility study. *Journal of Vacuum Science & Technology A: Vacuum, Surfaces, and Films*, 10(5):3266–3271, 1992.

[94] D Depla and S Mahieu. *Springer Series in Materials Science: Reactive Sputter Deposition*. Springer, 2008.

[95] G Wehner. Influence of the angle of incidence on sputtering yields. *Journal of Applied Physics*, 30(11):1762–1765, 1959.

[96] G Dupp and A Scharmann. Die zerstäubung von kupfer durch edelgasionen im energiebereich von 100 kev bis 1 mev als funktion des einfallswinkels. *Zeitschrift für Physik*, 194(5):448–452, 1966.

[97] KB Cheney and ET Pitkin. Sputtering at acute incidence. *Journal of applied Physics*, 36(11):3542–3544, 1965.

[98] PK Rol, JM Fluit, and J Kistemaker. Sputtering of copper by bombardment with ions of 5–25 kev. *Physica*, 26(11):1000–1008, 1960.

[99] P Sigmund. Theory of sputtering. i. sputtering yield of amorphous and polycrystalline targets. *Physical review*, 184(2):383, 1969.

[100] W Grove. On the electro-chemical polarity of gases. In *Abstracts of the Papers Communicated to the Royal Society of London*, volume 6, pages 168–169. The Royal Society, 1854.

[101] PD Townsend, JC Kelly, and N Hartley. Ion implantation. *Sputtering and Their Applications (Academic, New York, 1976)*, pages 166–169, 1976.

[102] HH Andersen and HL Bay. Sputtering yield measurements. In *Sputtering by particle bombardment I*, pages 145–218. Springer, 1981.

[103] PS McLeod and LD Hartsough. High-rate sputtering of aluminum for metallization of integrated circuits. *Journal of Vacuum Science & Technology*, 14(1):263–265, 1977.

[104] RK Waits. Planar magnetron sputtering. *Journal of Vacuum Science & Technology*, 15(2):179–187, 1978.

[105] JA Thornton. Magnetron sputtering: basic physics and application to cylindrical magnetrons. *Journal of Vacuum Science and Technology*, 15(2):171–177, 1978.

[106] A Anders. Tutorial: Reactive high power impulse magnetron sputtering (r-hipims). *Journal of Applied Physics*, 121(17):171101, 2017.

[107] A Anders. Discharge physics of high power impulse magnetron sputtering. *Surface and Coatings Technology*, 205:S1–S9, 2011.

[108] G Betz and W Husinsky. Modelling of cluster emission from metal surfaces under ion impact. *Philosophical Transactions of the Royal Society of London A: Mathematical, Physical and Engineering Sciences*, 362(1814):177–194, 2004.

[109] GP Können, A Tip, and AE De Vries. On the energy distribution of sputtered dimers. *Radiation Effects*, 21(4):269–274, 1974.

[110] GP Können, J Grosser, A Haring, AE De Vries, and J Kistemaker. Hyperthermal beams sputtered from alkalihalide surfaces. *Radiation Effects*, 21(3):171–179, 1974.

[111] W Gerhard. A model calculation of the neutral molecule emission by sputtering processes. *Zeitschrift für Physik B Condensed Matter*, 22(1):31–39, 1975.

[112] RA Haring, HE Roosendaal, and PC Zalm. On the energy and angular distribution of sputtered polyatomic molecules. *Nuclear Instruments and Methods in Physics Research Section B: Beam Interactions with Materials and Atoms*, 28(2):205–213, 1987.

[113] PJ Kelly and RD Arnell. Magnetron sputtering: a review of recent developments and applications. *Vacuum*, 56(3):159–172, 2000.

[114] JA Thornton. Influence of apparatus geometry and deposition conditions on the structure and topography of thick sputtered coatings. *Journal of Vacuum Science and Technology*, 11(4):666–670, 1974.

[115] R Messier, AP Giri, and RA Roy. Revised structure zone model for thin film physical structure. *Journal of Vacuum Science & Technology A: Vacuum, Surfaces, and Films*, 2(2):500–503, 1984.

[116] J Musil, S Kadlec, V Valvoda, R Kužel, and R Černỳ. Ion-assisted sputtering of tin films. In *Metallurgical Coatings and Thin Films 1990*, pages 259–269. Elsevier, 1990.

[117] S Craig and GL Harding. Effects of argon pressure and substrate temperature on the structure and properties of sputtered copper films. *Journal of Vacuum Science and Technology*, 19(2):205–215, 1981.

[118] D Güttler, B Abendroth, R Grötzschel, W Möller, and D Depla. Mechanisms of target poisoning during magnetron sputtering as investigated by real-time in situ analysis and collisional computer simulation. *Applied physics letters*, 85(25):6134–6136, 2004.

[119] D Depla and R De Gryse. Target poisoning during reactive magnetron sputtering: Part i: the influence of ion implantation. *Surface and Coatings Technology*, 183(2-3):184–189, 2004.

[120] D Depla and R De Gryse. Target poisoning during reactive magnetron sputtering: Part ii: the influence of chemisorption and gettering. *Surface and Coatings Technology*, 183(2-3):190–195, 2004.

[121] D Depla and R De Gryse. Target poisoning during reactive magnetron sputtering: Part iii: the prediction of the critical reactive gas mole fraction. *Surface and Coatings Technology*, 183(2-3):196–203, 2004.

[122] D Depla, S Heirwegh, S Mahieu, and R De Gryse. Towards a more complete model for reactive magnetron sputtering. *Journal of Physics D: Applied Physics*, 40(7):1957, 2007.

[123] D Depla, S Mahieu, and R De Gryse. Depositing aluminium oxide: a case study of reactive magnetron sputtering. In *Reactive Sputter Deposition*, pages 153–197. Springer, 2008.

[124] I Safi. Recent aspects concerning dc reactive magnetron sputtering of thin films: a review. *Surface and Coatings Technology*, 127(2):203–218, 2000.

[125] M Fleischmann, PJ Hendra, and AJ McQuillan. Raman spectra of pyridine adsorbed at a silver electrode. *Chem. Phys. Lett.*, 26(2):163–166, 1974.

[126] X Huang, PK Jain, IH El-Sayed, and MA El-Sayed. Plasmonic photothermal therapy (pptt) using gold nanoparticles. *Laser. Med. Sci.*, 23(3):217, 2008.

[127] K Awazu, M Fujimaki, C Rockstuhl, JJ Tominaga, H Murakami, Y Ohki, N Yoshida, and T Watanabe. A plasmonic photocatalyst consisting of silver nanoparticles embedded in titanium dioxide. *Journal of the American Chemical Society*, 130(5):1676–1680, 2008.

[128] XM Zhang, YL Chen, RS Liu, and DP Tsai. Plasmonic photocatalysis. *Rep. Prog. Phys.*, 76(4):046401, 2013.

[129] H Zhang, HV Demir, and AO Govorov. Plasmonic metamaterials and nanocomposites with the narrow transparency window effect in broad extinction spectra. *ACS Photonics*, 1(9):822–832, 2014.

[130] LV Besteiro, K Gungor, HV Demir, and AO Govorov. Simple and complex metafluids and metastructures with sharp spectral features in a broad extinction spectrum: Particle–particle interactions and testing the limits of the beer–lambert law. *J. Phys. Chem. C*, 121(5):2987–2997, 2017.

[131] JW Strutt. Lviii. on the scattering of light by small particles. *The London, Edinburgh, and Dublin Philosophical Magazine and Journal of Science*, 41(275):447–454, 1871.

[132] JW Strutt. Xxxvi. on the light from the sky, its polarization and colour. *The London, Edinburgh, and Dublin Philosophical Magazine and Journal of Science*, 41(273):274–279, 1871.

[133] M Hu, JY Chen, ZY Li, L Au, GV Hartland, XD Li, M Marquez, and Y Xia. Gold nanostructures: engineering their plasmonic properties for biomedical applications. *Chemical Society Reviews*, 35(11):1084–1094, 2006.

[134] AP Liu, T Xu, QH Ren, M Yuan, WJ Dong, and WH Tang. Graphene modulated 2d assembly of plasmonic gold nanostructure on diamond-like carbon substrate for surface-enhanced raman scattering. *Electrochemistry Communications*, 25:74–78, 2012.

[135] EB Dickerson, EC Dreaden, XH Huang, IH El-Sayed, HH Chu, S Pushpanketh, JF McDonald, and MA El-Sayed. Gold nanorod assisted near-infrared plasmonic photothermal therapy (pptt) of squamous cell carcinoma in mice. *Cancer letters*, 269(1):57–66, 2008.

[136] H Zhang, YJ Li, IA Ivanov, YQ Qu, Y Huang, and XF Duan. Plasmonic modulation of the upconversion fluorescence in nayf4: Yb/tm hexaplate nanocrystals using gold nanoparticles or nanoshells. *Angewandte Chemie*, 122(16):2927–2930, 2010.

[137] HJ Chen, L Shao, Q Li, and J Wang. Gold nanorods and their plasmonic properties. *Chemical Society Reviews*, 42(7):2679–2724, 2013.

[138] J Becker, A Trügler, A Jakab, U Hohenester, and C Sönnichsen. The optimal aspect ratio of gold nanorods for plasmonic bio-sensing. *Plasmonics*, 5(2):161–167, 2010.

[139] JM McMahon, AI Henry, KL Wustholz, MJ Natan, RG Freeman, RP Van Duyne, and GC Schatz. Gold nanoparticle dimer plasmonics: finite element method calculations of the electromagnetic enhancement to surface-enhanced raman spectroscopy. *Analytical and bioanalytical chemistry*, 394(7):1819–1825, 2009.

[140] BD Busbee, SO Obare, and CJ Murphy. An improved synthesis of high-aspect-ratio gold nanorods. *Adv. Mater.*, 15(5):414–416, 2003.

[141] NR Jana, L Gearheart, and CJ Murphy. Wet chemical synthesis of high aspect ratio cylindrical gold nanorods. *J. Phys. Chem B*, 105(19):4065–4067, 2001.

[142] SD Perrault and WC Chan. Synthesis and surface modification of highly monodispersed, spherical gold nanoparticles of 50- 200 nm. *J. Am. Chem. Soc.*, 131(47):17042–17043, 2009.

[143] M Rycenga, CM Cobley, J Zeng, WY Li, CH Moran, Q Zhang, D Qin, and Y Xia. Controlling the synthesis and assembly of silver nanostructures for plasmonic applications. *Chemical reviews*, 111(6):3669–3712, 2011.

[144] AL Pyayt, B Wiley, YN Xia, AT Chen, and L Dalton. Integration of photonic and silver nanowire plasmonic waveguides. *Nature nanotechnology*, 3(11):660–665, 2008.

[145] YJ Lu, JS Kim, HY Chen, CH Wu, N Dabidian, CE Sanders, CY Wang, MY Lu, BH Li, and XG Qiu. Plasmonic nanolaser using epitaxially grown silver film. *science*, 337(6093):450–453, 2012.

[146] A Tao, P Sinsermsuksakul, and PD Yang. Tunable plasmonic lattices of silver nanocrystals. *Nature nanotechnology*, 2(7):435–440, 2007.

[147] B Pietrobon, M McEachran, and V Kitaev. Synthesis of size-controlled faceted pentagonal silver nanorods with tunable plasmonic properties and self-assembly of these nanorods. *ACS nano*, 3(1):21–26, 2008.

[148] Y Ekinci, HH Solak, and JF Löffler. Plasmon resonances of aluminum nanoparticles and nanorods. *J. Appl. Phys.*, 104(8):083107, 2008.

[149] M Knight, NS King, L Liu, HO Everitt, P Nordlander, and NJ Halas. Aluminum for Plasmonics. *ACS Nano*, 8(1):834–840, January 2014.

[150] GH Chan, J Zhao, EM Hicks, GC Schatz, and RP Van. Plasmonic Properties of Copper Nanoparticles Fabricated by Nanosphere Lithography. *Nano Lett.*, 7(7):1947–1952, 2007.

[151] R Zong, J Zhou, B Li, M Fu, S Shi, and L Li. Optical properties of transparent copper nanorod and nanowire arrays embedded in anodic alumina oxide. *J. Chem. Phys.*, 123(9):094710–6, 2005.

[152] H Chen, J Lee, Y Kim, D Shin, S Park, X Meng, and J Yoo. Metallic copper nanostructures synthesized by a facile hydrothermal method. *J. Nanosci. Nanotechnol.*, 10(1):629–636, 2010.

[153] H Wang, F Tam, NK Grady, and NJ Halas. Cu nanoshells: effects of interband transitions on the nanoparticle plasmon resonance. *J. Phys. Chem. B*, 109(39):18218–18222, 2005.

[154] MW Knight and NJ Halas. Nanoshells to nanoeggs to nanocups: optical properties of reduced symmetry core–shell nanoparticles beyond the quasistatic limit. *New J. Phys.*, 10(10):105006, 2008.

[155] NS King, Y Li, C Ayala-Orozco, T Brannan, P Nordlander, and NJ Halas. Angle-and spectral-dependent light scattering from plasmonic nanocups. *ACS Nano*, 5(9):7254–7262, 2011.

[156] NA Mirin and NJ Halas. Light-bending nanoparticles. *Nano Lett.*, 9(3):1255–1259, 2009.

[157] Y Lu, GL Liu, J Kim, YX Mejia, and LP Lee. Nanophotonic crescent moon structures with sharp edge for ultrasensitive biomolecular detection by local electromagnetic field enhancement effect. *Nano Lett.*, 5(1):119–124, 2005.

[158] J Liu, B Cankurtaran, G McCredie, MJ Ford, L Wieczorek, and MB Cortie. Investigation of the optical properties of hollow aluminium nano-caps. *Nanotechnol.*, 16(12):3023, 2005.

[159] J He, P Zhang, J Gong, and Z Nie. Facile synthesis of functional au nanopatches and nanocups. *Chem. Commun.*, 48(59):7344–7346, 2012.

[160] R Jiang, F Qin, Y Liu, X Ling, J Guo, M Tang, S Cheng, and J Wang. Colloidal gold nanocups with orientation-dependent plasmonic properties. *Adv. Mater.*, 28(30):6322–6331, 2016.

[161] D Rodríguez-Fernández, J Pérez-Juste, I Pastoriza-Santos, and LM Liz-Marzán. Colloidal synthesis of gold semishells. *ChemistryOpen*, 1(2):90–95, 2012.

[162] C Charnay, A Lee, S Man, CE Moran, C Radloff, R Bradley, and NJ Halas. Reduced symmetry metallodielectric nanoparticles: chemical synthesis and plasmonic properties. *J. Phys. Chem. B*, 107(30):7327–7333, 2003.

[163] P Van Dorpe and J Ye. Semishells: versatile plasmonic nanoparticles. *ACS Nano*, 5(9):6774–6778, 2011.

[164] P Pramod and KG Thomas. Plasmon coupling in dimers of au nanorods. *Adv. Mater.*, 20(22):4300–4305, 2008.

[165] I Romero, J Aizpurua, GW Bryant, and FJB De Abajo. Plasmons in nearly touching metallic nanoparticles: singular response in the limit of touching dimers. *Opt. Express*, 14(21):9988–9999, 2006.

[166] JH Yang, NJ Kramer, KS Schramke, LM Wheeler, LV Besteiro, CJ Hogan Jr, AO Govorov, and UR Kortshagen. Broadband absorbing exciton–plasmon metafluids with narrow transparency windows. *Nano Lett.*, 16(2):1472–1477, 2016.

[167] H Wu, J Henzie, W Lin, C Rhodes, Z Li, E Sartorel, J Thorner, P Yang, and JT Groves. Membrane-protein binding measured with solution-phase plasmonic nanocube sensors. *Nat. Methods*, 9(12):1189–1191, 2012.

[168] M Frederiksen, VE Bochenkov, MB Cortie, and DS Sutherland. Plasmon hybridization and field confinement in multilayer metal–dielectric nanocups. *J. Phys. Chem. C*, 117(30):15782–15789, 2013.

[169] G Xiao and S Man. Synthesis of bismuth nanocap arrays on quartz substrates and their surface plasmon resonance properties. *J. Phys. Chem. Solids*, 73(4):604–607, 2012.

[170] P Zhan, ZL Wang, H Dong, J Sun, J Wu, H Wang, SN Zhu, NB Ming, and J Zi. The anomalous infrared transmission of gold films on two-dimensional colloidal crystals. *Adv. Mater.*, 18(12):1612–1616, 2006.

[171] J Liu, AI Maaroof, L Wieczorek, and MB Cortie. Fabrication of hollow metal nanocaps and their red-shifted optical absorption spectra. *Adv. Mater.*, 17(10):1276–1281, 2005.

[172] K Sugawa, T Tamura, H Tahara, D Yamaguchi, T Akiyama, J Otsuki, Y Kusaka, N Fukuda, and H Ushijima. Metal-enhanced fluorescence platforms based on plasmonic ordered copper arrays: wavelength dependence of quenching and enhancement effects. *ACS Nano*, 7(11):9997–10010, 2013.

[173] L Wollet, B Frank, M Schäferling, M Mesch, S Hein, and H Giessen. Plasmon hybridization in stacked metallic nanocups. *Opt. Mater. Express*, 2(10):1384–1390, 2012.

[174] S Yang, M Lapsley, B Cao, C Zhao, Y Zhao, Q Hao, B Kiraly, J Scott, W Li, and L Wang. Large-scale fabrication of three-dimensional surface patterns using template-defined electrochemical deposition. *Adv. Funct. Mater.*, 23(6):720–730, 2013.

[175] X Zhu, S Xiao, L Shi, X Liu, J Zi, O Hansen, and NA Mortensen. A stretch-tunable plasmonic structure with a polarization-dependent response. *Opt. Express*, 20(5):5237–5242, 2012.

[176] Z Chen, P Zhan, W Dong, Y Li, C Tang, N Min, and Z Wang. Bottom-up fabrication approaches to novel plasmonic materials. *Chinese Sci. Bull.*, 55(24):2600–2607, 2010.

[177] J Ye, N Verellen, W Van Roy, L Lagae, G Maes, G Borghs, and P Van Dorpe. Plasmonic modes of metallic semishells in a polymer film. *ACS Nano*, 4(3):1457–1464, 2010.

[178] J Martin and J Plain. Fabrication of aluminium nanostructures for plasmonics. *J. Phys. D: Appl. Phys.*, 48(18):184002, 2014.

[179] PB Johnson and R Christy. Optical constants of the noble metals. *Phys. Rev. B*, 6(12):4370, 1972.

[180] AD Rakić. Algorithm for the determination of intrinsic optical constants of metal films: application to aluminum. *Appl. Opt.*, 34(22):4755–4767, 1995.

[181] J Carmody. *Residential windows: a guide to new technologies and energy performance*. WW Norton & Company, 2007.

[182] MT Taschuk, MM Hawkeye, and MJ Brett. Glancing angle deposition. *Handbook of Deposition Technologies for Films and Coatings*, pages 621–678, 2010.

[183] C Chen, T Yamaguchi, K Sugawara, and K Koga. Role of stress in the self-limiting oxidation of copper nanoparticles. *The Journal of Physical Chemistry B*, 109(44):20669–20672, 2005.

[184] C Ernsberger, J Nickerson, T Smith, AE Miller, and D Banks. Low temperature oxidation behavior of reactively sputtered tin by x-ray photoelectron spectroscopy and contact resistance measurements. *Journal of Vacuum Science & Technology A: Vacuum, Surfaces, and Films*, 4(6):2784–2788, 1986.

[185] HG Tompkins. Oxidation of titanium nitride in room air and in dry o2. *Journal of Applied Physics*, 70(7):3876–3880, 1991.

[186] HG Tompkins. The initial stages of the oxidation of titanium nitride. *Journal of Applied Physics*, 71(2):980–983, 1992.

[187] M Wittmer, J Noser, and H Melchior. Oxidation kinetics of tin thin films. *Journal of Applied Physics*, 52(11):6659–6664, 1981.

[188] P Hones, C Zakri, PE Schmid, F Lévy, and OR Shojaei. Oxidation resistance of protective coatings studied by spectroscopic ellipsometry. *Applied Physics Letters*, 76(22):3194–3196, 2000.

[189] G Samsonov. *The oxide handbook*. Springer Science & Business Media, 2013.

[190] YL Jeyachandran, SK Narayandass, D Mangalaraj, S Areva, and JA Mielczarski. Properties of titanium nitride films prepared by direct current magnetron sputtering. *Materials Science and Engineering: A*, 445:223–236, 2007.

[191] S Mahieu, P Ghekiere, G De Winter, S Heirwegh, D Depla, R De Gryse, OI Lebedev, and G Van Tendeloo. Mechanism of preferential orientation in sputter deposited titanium nitride and yttria-stabilized zirconia layers. *Journal of crystal growth*, 279(1-2):100–109, 2005.

[192] LJ Meng and MP Dos Santos. Characterization of titanium nitride films prepared by dc reactive magnetron sputtering at different nitrogen pressures. *Surface and Coatings Technology*, 90(1-2):64–70, 1997.

[193] L Combadiere and J Machet. Reactive magnetron sputtering deposition of tin films. i. influence of the substrate temperature on structure, composition and morphology of the films. *Surface and Coatings Technology*, 88(1-3):17–27, 1997.

[194] WD Sproul, PJ Rudnik, and ME Graham. The effect of n2 partial pressure, deposition rate and substrate bias potential on the hardness and texture of reactively sputtered tin coatings. *Surface and Coatings Technology*, 39:355–363, 1989.

[195] H Chen and F Lu. Oxidation behavior of titanium nitride films. *Journal of Vacuum Science & Technology A: Vacuum, Surfaces, and Films*, 23(4):1006–1009, 2005.

# Appendix A

# Fabrication of Anisotropic Plasmonic Nanostructures: Preliminary Results on TiN

Unlike the fabrication processes for copper and aluminum plasmonic nanostructures, TiN poses an extra challenge: stoichiometry.

Even though oxidation of stoichiometric TiN is favorable from the thermodynamic point of view ($\mathrm{TiN} + \mathrm{O_2} \longrightarrow \mathrm{TiO_2} + \frac{1}{2}\mathrm{N_2}$ , $\Delta G^o$=$-139$ kcal/mol), the specific oxidation kinetics are actually quite slow, especially at temperatures below 500 $^o$C. Ernsberger *et al.* [184] studied the oxidation behavior of TiN films at room temperature and proposed a logarithmic formula for the oxide thickness. Using their formula, TiN only develops an oxide layer of 1.6 nm over a period of 3 months. Tompkins *et al.* [185, 186] studied the oxidation behavior between 350 $^o$C and 450 $^o$C and observed a very slow initial oxidation stage followed by a regular oxidation stage, both of which can be described with a parabolic equation: $y^2 = kt$ where $y$ is the oxide thickness and $k$ is the oxidation rate constant with a form of $k = k_o \exp(-\frac{E}{RT})$ where $k_o$ is a constant, $E$ is the activation energy required for the oxygen diffusion process, $R$ is the gas constant and $T$ is the temperature. Wittmer *et al.* [187] studied the oxidation behavior between 500 $^o$C and 650 $^o$C and proposed a parabolic formula for the oxidation kinetics.

Sub-stoichiometric and over-stoichiometric TiN, however, more readily oxidizes upon exposure to air. Hones *et al.* [188] proposed that for nitrogen rich TiN films, the excess nitrogen atoms favor the formation of molecular nitrogen, the formation enthalpy of which essentially decreases the activation energy for TiN oxidation. On the other hand, for nitrogen deficient TiN films, the oxidation of Ti into $TiO_2$ offers a new pathway for oxidation with a lower activation energy [189].

Therefore, care should be taken to ensure a near-stoichiometric TiN film during magnetron sputtering. Extensive studies have been conducted to study the effects of discharge power, $N_2$ partial pressure, total gas pressure, substrate temperature and substrate bias on the microstructures and stoichiometry of the deposited TiN films. While in some studies stoichiometric TiN films were successfully synthesized without substrate bias or substrate heating [190], the base pressures of the sputtering reactors used in those studies are usually very low, on the order of $10^{-9}$ Torr. Most studies, on the other hand, stress the importance of substrate heating or bias on film stoichiometry. In fact, preliminary attempts were made to deposit TiN films without substrate heating or bias in the NFC sputtering system AJA1, which has a base pressure of high $10^{-7}$ Torr, but all of the films turned out to have high oxygen percentages even though some exhibit the typical golden color of stoichiometric TiN [191]. While stage heating is possible in the AJA1 system, it only works for regular depositions, *i.e.* non-glancing angle depositions (GLAD). For GLAD depositions in AJA1, an improvised substrate holder has to be used and the substrate will no longer be in direct contact with the heated stage. This is the primary reason that prompted us to construct our own sputtering system, that is, a sputtering system with a tiltable, heated stage.

Aside from substrate heating, it has been shown that higher $N_2$ partial pressures are also beneficial for TiN deposition. Meng *et al.* [192] observed increasing grain sizes with increasing $N_2$ partial pressures. Combadiere *et al.* [193] successfully synthesized stoichiometric TiN at high $N_2$ partial pressures and high substrate temperatures while over-stoichiometric TiN were synthesized at lower substrate temperatures. They attributed the difference in stoichiometry to desorption of $N_2$ at high substrate temperatures. This suggests that a combination of high substrate temperature and high $N_2$ flow rate might be ideal for TiN deposition.

Higher sputtering power has also been shown to improve TiN film quality [194]. This is because a higher ion flux gets to the substrate and effectively heats up the film during deposition, creating a denser film with larger grain sizes. Existence of large grain boundaries can provide an effective shortcut for the diffusion of oxygen and therefore oxidation of the TiN film [195]. However, care must be taken to increase $N_2$ partial pressures correspondingly as gas heating and rarefaction under high sputtering power can reduce the nitrogen density near the target significantly [194].

## A.1 Custom-built Angle Sputtering System

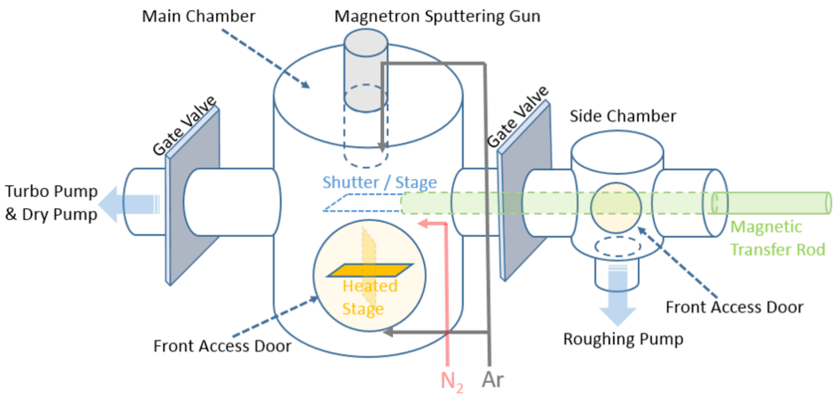

Figure A.1: Schematic of the custom-built angle sputtering system.

A schematic of the custom-built angle sputtering system is shown in Fig. A.1. On the top of the main chamber is the Torus sputtering gun purchased from Kurt J. Lesker. The sputtering gun uses a 2” diameter target. Two gate valves separate the main chamber from the turbo pump and the side chamber, respectively. When the gate valve on the side chamber side is opened, the main chamber can be pumped down by the roughing pump connected to the side chamber. Both the main chamber and the side chamber have a front access door, through which substrates can be manually loaded onto the heated stage in the main chamber or the secondary stage (also serves as shutter) in the side chamber. A magnetic transfer rod can move the shutter between the main chamber and the side chamber. The shutter can be used to block the sputtered atoms from the substrate. This is especially useful for oxidation-prone targets such as titanium. A pre-sputtering process can remove the thin oxide layer on the target, during which process a shutter should be used to block the fluxes from the substrate. The magnetic transfer rod and the shutter can be rotated so that both surfaces of the shutter can be exposed to the sputtering gun. While one side of the shutter can be used for the blocking purpose, the other side can be used as a secondary deposition stage if heating is not required. Substrates can be placed onto the shutter through the front access door on the side chamber. Argon gases can be introduced into the chamber at the bottom or through the gas distribution ring integrated in the sputtering gun. Nitrogen is introduced laterally into the chamber, close to the substrate and at a certain distance away from the sputtering gun, so that target poisoning can be controlled to some level.

A photo of the sputtering system is shown in Fig. A.2(a). A close-up look at the top part is shown in Fig. A.2(b). The sputtering gun has an 18” shaft that goes from the top of the reactor all the way to the main chamber. Sealing of the shaft against the chamber is done by an ultra-torr fitting so that the

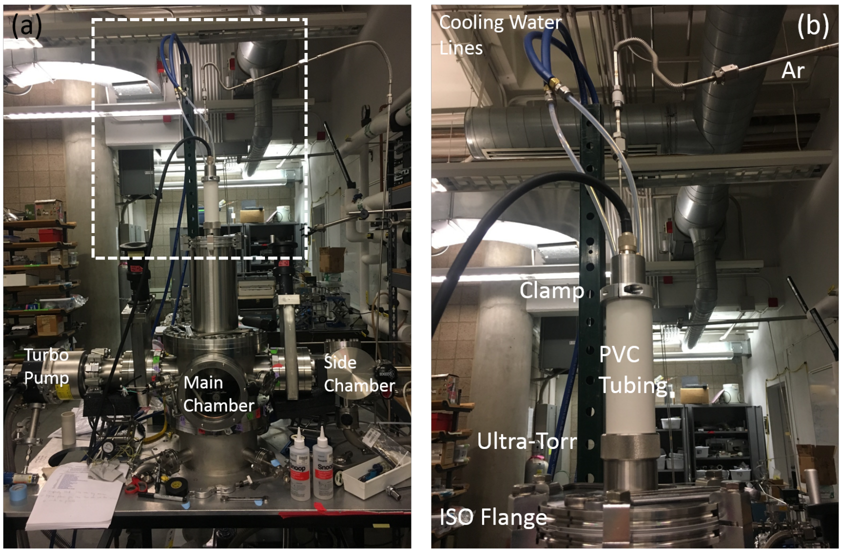

Figure A.2: (a) A photo of the custom-built angle sputtering system and (b) a close-up look at the top part.

vertical position of the sputtering gun can be adjusted if needed. To support the weight of the sputtering gun, a clamp is placed at the very end of the shaft. The PVC tubing is used to transfer the weight from the clamp to the upper surface of the ultra-torr and therefore to the chamber. The clamp is not placed right above the ultra-torr because scratches on the shaft in that region might affect the sealing performance of the ultra-torr. If the sputtering target needs to be changed, the whole sputtering gun can be removed from the chamber by undoing the ISO flange. An argon gas line can be seen at the very top and runs directly into the gas distribution ring of the sputtering gun. Cooling water lines are also installed to cool down the sputtering target during operation. With effective cooling the sputtering gun can be operated at higher powers without the target being melted.

A close-up top-down view of the tiltable stage is shown in Fig. A.3. Two substrate clamps and one substrate stopping pin help to keep the substrate in place, especially during GLAD. The tilting knob and the fixation knob can be turned through the front access door on the main chamber. A heater is flush with the stage surface and will be in direct contact with the substrate to be heated. Maximum temperature of the heater is 400 $^o$C. A thermocouple directly built into the heater measures the core temperature of the heater and provides the feedback signal for a customized temperature control box. A secondary thermocouple is bolted to the stage for easy measurement of the stage temperature and can serve as the backup thermocouple for the heater.

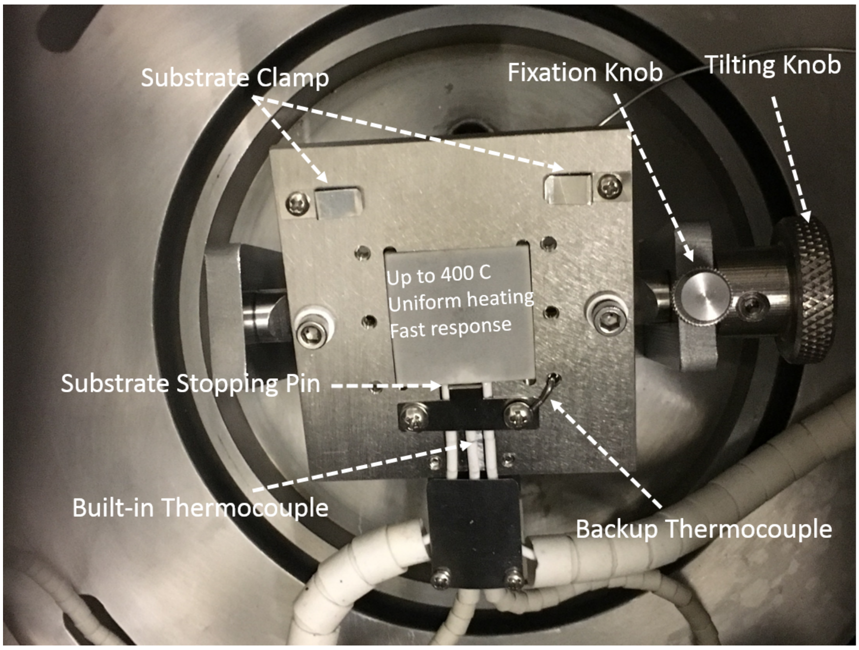

Figure A.3: A top-down view of the tiltable stage in the custom-built angle sputtering system.

## A.2 Silica Colloidal Template for Heated Deposition

The PSL templates used in the fabrication of copper and aluminum plasmonic nanostructures have a glass transition temperature of about 100 $^o$C and cannot be used for the heated deposition of TiN. Fortunately dispersions of silica particles are also commercially available and can be used to replace the PLS templates. With an appropriate combination of dispersion weight concentration (3.33 wt% in DI water), spinning speed (800 rpm) and spinning time (3 min), a hexagonally close-packed silica template can be obtained, shown in Fig. A.4.

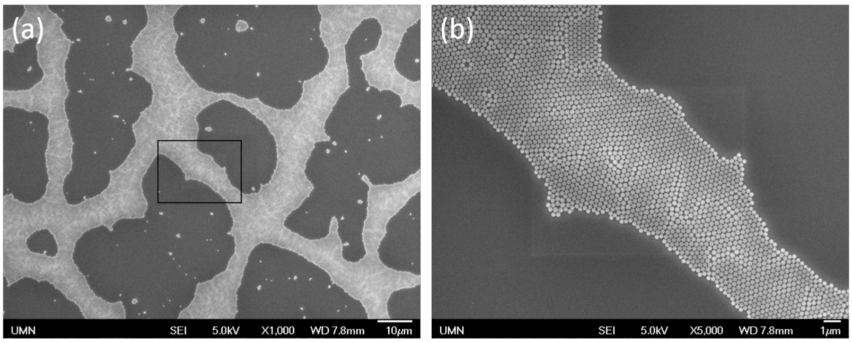

Figure A.4: (a) Topview SEM image of a hexagonally close-packed silica template and (b) a close-up look at the area in the black square.

RIE attempts of the close-packed silica templates were carried out in three different plasma etchers. Two were already mentioned above in previous sections for the etching of PSL particles, namely AV etcher and STS etcher. In these two etchers, using similar pressures and powers as those used for the etching of PSL particles, it turned out that these silica particles are much more resistant to plasma etching. For example, with 25 sccm $CF_4$, 50 sccm $CHF_3$ and 25 sccm Ar, the silica particles only shrink a little after 10 min of etching at 50 W and 125 mTorr, shown in Fig. A.5(a). The high $CHF_3$ to $CF_4$ ratio is to increase selectivity of $SiO_2$ etching over Si etching.

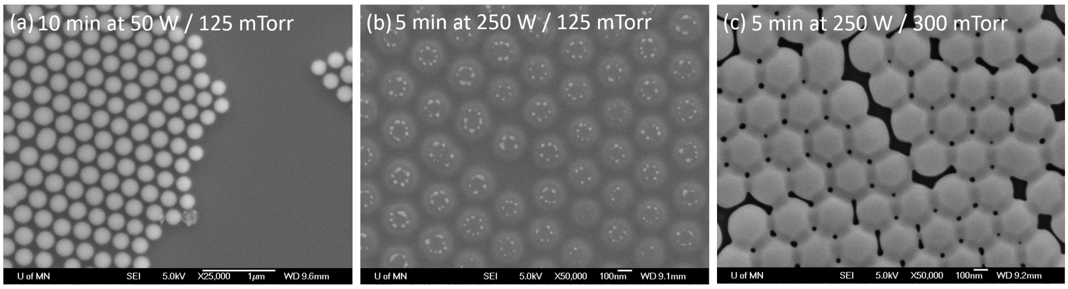

Figure A.5: Topview SEM images of the silica template after (a) 10 mins of etching at 50 W and 125 mTorr, (b) 5 mins of etching at 250 W and 125 mTorr and (c) 5 mins of etching at 250 W and 300 mTorr. Gas flow rates are 25 sccm $CF_4$, 50 sccm $CHF_3$ and 25 sccm Ar for all three recipes.

Due to the low etching rates, etching recipes with the same gas flow rates but with higher plasma powers and plasma pressures were tested. Fig. A.5(b) shows the topview SEM image of silica particles after 5 mins of etching in a plasma maintained at 250 W and 125 mTorr. It can be seen that the silica particles are completely shattered. Various powers between 150 W and 250 W were tested and all recipes ended up with shattered particles. This is due to the large dc bias developed at high plasma powers. Fig. A.5(c) shows the topview SEM image of silica particles after 5 mins of etching in a plasma maintained at 250 W and 300 mTorr. It can be seen that the particles are melted and form neckings in-between.

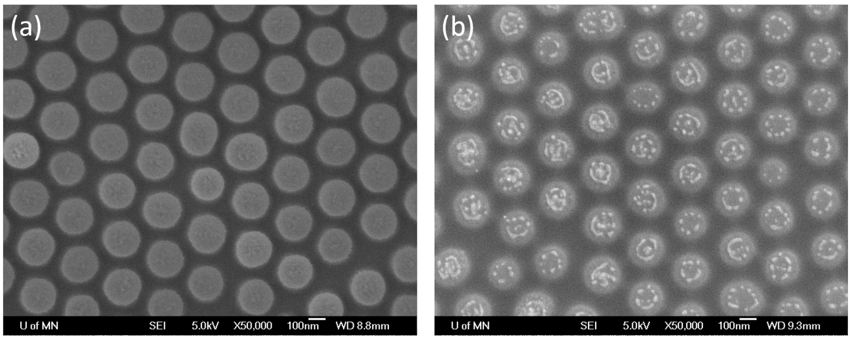

Figure A.6: Topview SEM images of the silica template after (a) 5 mins and (b) 7.5 mins of etching at 150 W and 125 mTorr. Gas flow rates are 25 sccm $CF_4$, 50 sccm $CHF_3$ and 25 sccm Ar.

Reducing the power to 150 W yields faster etching and still intact silica particles for the first 5 mins of etching, see Fig. A.6(a), and then the particles reach a critical diameter and get shattered, see Fig. A.6(b). Further optimization on the etching plasma power might be required to create silica templates of yet smaller particles than the ones shown in Fig. A.6(a).

In a set of parallel experiments, to solve the low etching rate issue, a remote inductively coupled plasma (ICP) etcher is tested as well (Plasmalab System 100 ICP 180). In this etcher the reactive species are generated in the ICP chamber and then get transfered to the main etching chamber in which a CCP plasma is generated. In other words, the density of the reactive species and the dc bias on the wafer can be separately controlled. Ideally the reactive species density should be high enough to speed up etching while the dc bias should be limited to a relatively low value to prevent the particles from being shattered. It turned out, however, that the initially spherical silica particles are turned into hemispheres after being etched in this reactor, even at the lowest ICP power available (500 W) for only 3 or 4 mins, shown in Fig. A.7(a). At higher ICP powers (700 W) the silica particles are turned into domes, shown in Fig. A.7(b). Note that this minimum power on the ICP remote power, 500 W, is still much higher than the powers used on the other two etchers. It is reasonable to assume that this irregular hemisphere or dome shape is at least partially caused by the high ICP power as no domes or hemispheres were ever observed in samples etched from the other two etchers (shown in Fig. A.7(c)) at similar gas flow rates and pressures. For this reason, future RIE experiments of the silica templates should be conducted in the other two etchers, namely STS etcher and AV etcher.

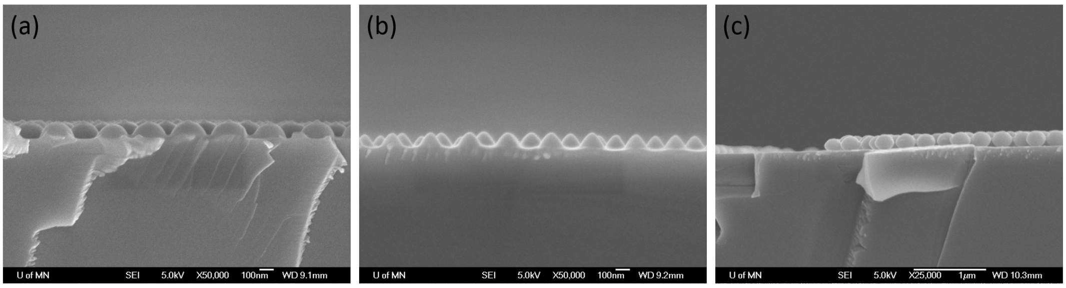

Figure A.7: Sideview SEM images for (a) 500 W on remote ICP etcher (b) 700 W on remote ICP etcher (c) 150 on STS etcher. All recipes use similar gas flow rates and pressures.